Two-Phase Immersion Cooling for Power Dense Printed Circuit Board Converters

Aleksandar Ristic-Smith

Mansfield College

University of Oxford

A thesis submitted for the degree of

Doctor of Philosophy

Hillary 2024

Acknowledgements

My DPhil studies were funded by the Engineering and Physical Sciences Research Council UK under a CASE award (EP/R513295/1) and supported by industrial partner YASA Ltd to whom I am very grateful for their support.

First and foremost, I would extend thanks to my supervisor Prof. Dan Rogers for his exceptional guidance at every step of the way. By working with Dan, I have learnt many invaluable lessons both relating to the technical aspects of power electronics and to navigating the struggles of academic life.

Special thanks to Simon Hart, Dan Rendell, Paul Spendley and Rajesh Kudikala who were associated with YASA Ltd during my DPhil and provided excellent technical advice and suggestions, particularly related to electric vehicle motor drives. As part of the CASE studentship, I spent six weeks working with the team at Evolito Ltd, whose insight provided me with valuable perspective on future trends and challenges in the field of electrified transport.

During my time as a DPhil student, I had the privilege of participating in fruitful collaborations with my good friends and colleagues in the Power Electronics group, Kawsar Ali and Jack Bruford. Furthermore, I greatly enjoyed the company of Gwilym Jones, Ngoni Mugwisi, Derek Neil, Pengling Li, Matthew Cooke and Thomas Bryden, always looking forward to our next weekly group meeting.

Last but not least, I am thankful to my mother Jasmina, my brother Marko and to Isidora for their unwavering support and helpful advice throughout the DPhil process.

Abstract

This thesis presents research into two-phase immersion cooling with Novec 7000 dielectric fluid in sealed enclosures for power electronic converters on printed circuit board substrates. Pool boiling heat transfer is experimentally characterised at elevated saturation temperature and pressure on a flat planar surface representative of a semiconductor switch. Critical heat flux of $43\,\mathrm{W/cm^2}$ is observed and the maximum heat transfer coefficient is $1.5\,\mathrm{W/(cm^2\,K)}$. A theoretical model and numerical solution method for boiling on pin fins is developed and used to design heat spreaders to increase the power dissipation per unit semiconductor area with minimal penalty on the converter volume. A maximum switch level heat transfer coefficient of $2.5\,\mathrm{W/(cm^2\,K)}$ is demonstrated experimentally. By grit-blasting the heat spreader surface, the switch level heat transfer coefficient increases to $3.4\,\mathrm{W/(cm^2\,K)}$.

A sealed two-phase immersion cooling system design is proposed for an electric vehicle motor drive. The system could theoretically sustain power dissipation of $30\,\mathrm{W/(L\,K)}$, which is competitive with the best performing systems in previous literature. The design facilitates integration of semiconductor switches, decoupling capacitors and gate drivers in close proximity on a single printed circuit board. This is an important step towards achieving power-dense PCB converters with low parasitic inductance electrical layouts.

Experiments with copper wires immersed in Novec 7000 indicate the maximum current-carrying capacity is up to eight times greater than for forced air cooling. Furthermore, it is shown that immersion of magnetic cores enables operation at high flux density and frequency. The volumetric power loss in a ferrite core is characterised at frequencies up to 1.6 MHz and flux densities up to saturation, a substantially wider operating range than is typically provided in material data-sheets. These results indicate it is possible to construct inductors and transformers with up to eight times smaller volume than those cooled by forced air. This is particularly important for applications like on-board chargers in electric vehicles, where compact magnetic components can lead to substantial reduction in volume for transformer isolated DC-DC converters.

Contents

List of Figures **xi**

List of Tables **xv**

List of Abbreviations **xvii**

Nomenclature **xix**

1 Introduction **1**

1.1 Motivation 1

1.1.1 Semiconductor Switches 1

1.1.2 Magnetic Components 4

1.1.3 Two-phase Immersion Cooling 5

1.2 Contribution 6

2 Literature Review **9**

2.1 Boiling Heat Transfer Background 9

2.1.1 Boiling Concepts 9

2.1.2 Fluid Selection 12

2.2 Boiling Heat Transfer for Semiconductor Switches 16

2.2.1 Switch Surface Micro-Enhancement 16

2.2.2 Switch Heat Spreaders 20

2.2.3 Comparison with High Heat Flux Liquid Cooling 23

2.3 Two-phase Immersion Cooling Systems 25

2.3.1 Heat Exchanger Performance 27

2.3.2 Overall System Performance 28

2.4 Two-phase Immersion Cooling for Magnetic Components 29

3 Boiling Heat Transfer for Planar Semiconductor Switches **31**

3.1 Fluid Thermophysical Properties 32

3.1.1 Surface Tension 32

3.1.2 Vapour Density 33

3.1.3 Latent Heat 34

3.2 Pool Boiling Models 35
3.2.1 Nucleate Boiling 35
3.2.2 Critical Heat Flux 37
3.3 Experimental Verification 38
3.3.1 Test Apparatus 39
3.3.2 Data Collection 41
3.3.3 Experimental Results 43
3.4 Conclusions 47

4 Boiling Heat Transfer for Finned Heat Spreaders 49
4.1 Boiling Fin Model 50
4.1.1 Numerical Solution Procedure 51
4.1.2 Comparison with Analytical Solutions 52
4.2 Heat Spreader Design 53
4.2.1 Modelling Finned Heat Spreaders 56
4.3 Experimental Verification 58
4.4 Conclusions 62

5 Power Density of Two-Phase Immersion Cooled Converters 63
5.1 Condensation on Finned Surfaces 64
5.1.1 Numerical Solution Procedure 65
5.1.2 Heat Exchanger Design 68
5.2 Experimental Results 68
5.3 Motor Drive Inverter 71
5.3.1 Two-Phase Immersion Cooling Performance 71
5.3.2 Leak Testing 73
5.4 Conclusions 76

6 Power Density of Two-Phase Immersion Cooled Magnetic Components 79
6.1 Coil Current Limits 81
6.1.1 Bare Copper Windings 82
6.1.2 Litz Wire Windings 86
6.2 Magnetic Cores 89
6.2.1 Curie Temperature Thermal Model 90
6.2.2 Magnetic Core Experiments 91
6.3 Transformer Power Density 94
6.3.1 Core Sizing 95
6.4 Conclusions 96

7 Discussion and Future Work **99**
7.1 Conclusions 99
7.2 Future Work 102

Appendices

A Uncertainty Evaluation **109**

B Analytical Solutions of the One-Dimensional Heat Equation **111**
B.1 Pin Fin with Uniform Surface Heat Flux 111
B.2 Cylindrical Magnetic Core with Uniform Power Dissipation 112

C Transformer Core Sizing **115**

References **117**

List of Figures

1.1 Diagram of a conventional power module. 2
1.2 Diagram of a possible PCB substrate converter. 4
1.3 Diagram of proposed two-phase immersion cooling for PCB substrate converters. 6

2.1 Boiling curve and corresponding heat transfer coefficients for water on platinum wire. Reproduced from data published in [12]. 9
2.2 Diagram of an immersed semiconductor switch. 16
2.3 Scanning electron microscope images of surfaces treated with emery paper and vapour blasting. Reproduced from [24] and [26] respectively. 17
2.4 Scanning electron microscopy images of 50 µm fins with heights 60 µm, 200 µm and 270 µm respectively. Reproduced from [34]. 18
2.5 Scanning electron microscope images of sintered and electroplated microporous copper coatings. Reproduced from [35] ©2022 IEEE. . 18
2.6 Diagrams showing two different breathing modes for lotus copper on grooved surfaces. Reproduced from [38]. 19
2.7 Diagram of an immersed semiconductor switch with heat spreader attached. 20
2.8 Finned heat spreader with microporous coating used to investigate the effect of lateral heat spreading, reproduced from [40] ©2006 IEEE. 21
2.9 Diagram showing assembly with bare die semiconductor switches and heat spreaders to facilitate double-sided cooling. Reproduced from [42] ©2010 IEEE. 22
2.10 Diagram of additively manufactured folded aluminium microchannel heat sink with impinging jet flow. Reproduced from [46] ©2021 IEEE. 24
2.11 Silicon microchannel heat sink coupled to a semiconductor switch by thermal interface material. Reproduced from [47] ©2020 IEEE. . . . 25
2.12 Diagram of air cooled fin and tube heat exchanger for two-phase immersion systems. Reproduced from [50] ©2007 IEEE. 27
2.13 Diagram of an immersion cooled traction inverter using gate turn on (GTO) thyristor switches. Reproduced from [42] ©2010 IEEE. . . . 28

2.14 Renders of two-phase immersion cooled system with liquid-cooled heat exchanger integrated into the chamber. Reproduced from [57] ©2015 IEEE. 30

3.1 Ratio of vapour densities calculated by ideal gas equation and Redlich-Kwong equation. 34
3.2 Heat transfer coefficient as a function of fluid saturation temperature. 37
3.3 Critical heat flux as a function of fluid saturation temperature. . . . 38
3.4 Diagram showing correspondence between a planar semiconductor switch and its facsimile. 39
3.5 Section views of experimental apparatus. All dimensions are in millimetres. 40
3.6 Heat loss to ambient air through heater block insulation as a function of the facsimile temperature increase above ambient. 42
3.7 (a) Measured temperatures T_{c}, T_{s} and T_{b} and (b) saturation pressure P_{s} at different power dissipations. 43
3.8 Heat flux dependence on difference between average facsimile temperature T_{c} and fluid saturation temperature T_{s}. 44
3.9 Experimental and theoretical critical heat fluxes at different fluid saturation temperature. 45
3.10 Experimental and theoretical heat transfer coefficients. 46

4.1 Diagrams depicting model of an immersed fin and discretisation into segments for numerical solving. 50
4.2 Percentage error for fin heat and mean percentage error for fin temperature with varying error tolerance ϵ and number of segments N. 52
4.3 (a) Mean ratio of numerically computed fin temperature to analytical solution and (b) Ratio of numerically computed fin heat to analytical solution for 1000 different fins. 54
4.4 Bubble departure diameter for Novec 7000 as a function of saturation temperature. 55
4.5 Area enhancement for heat spreaders with varying fin width. 56
4.6 Switch-level heat transfer coefficients for three candidate heat spreader arrangements with fins of varying length. 57
4.7 Switch-level critical heat fluxes for three candidate heat spreader arrangements with fins of varying length. 58
4.8 Diagram showing correspondence between a semiconductor switch with heat spreader and its facsimile. 58
4.9 Experimental and theoretical switch-level heat transfer coefficients for the smooth heat spreader facsimile. 60

4.10 Experimental switch-level heat transfer coefficients for the smooth and grit blasted heat spreader facsimiles as well as the planar facsimile from Chapter 3. 61
4.11 Measured switch-level heat fluxes for a single smooth heat spreader facsimile compared with theoretical prediction. 61

5.1 Diagrams depicting model of gravity-driven condensation on a fin and discretisation into segments for numerical solving. 64
5.2 Lengths of fin corresponding to different Bond numbers for varying fluid saturation temperature. 66
5.3 Mean percentage error in film thickness for different numbers of segments. 67
5.4 Total heat transfer across heat exchanger for a flat surface and enhanced with fins of varying length. 69
5.5 Fin base temperature and fluid saturation temperature for experiments conducted with three different switch facsimile types. 69
5.6 Temperature difference between fluid and fin base as a function of temperature. Experimental results and model predictions are shown for comparison. 70
5.7 Temperatures measured at the fin base, the fluid and the switch facsimile for flat and grit-blasted fin facsimiles. 71
5.8 Diagram of the proposed motor drive inverter on PCB substrate enclosed in a two-phase immersion cooling chamber. 72
5.9 Photographs of printed circuit board and full test apparatus used to investigate leakage of non-condensible gases. 74
5.10 Pressure measurements taken over a period of two weeks with four thermal cycles applied. 76

6.1 Maximum frequency for copper wire coils of varying diameter based on skin effect. 81
6.2 Per length values of power loss and surface heat transfer as a function of wire temperature at different currents. 83
6.3 Critical heat flux for a small horizontal wire as a function of its diameter according to the Zuber model of Equation 6.5. 84
6.4 Current limits based on thermal runaway and critical heat flux as a function of wire diameter. 85
6.5 Experimental apparatus used for testing of magnetic components. . . 86
6.6 Pictures showing different degrees of strand fusing for 300/46 Litz wire tested at three different current values. 88

6.7 (a) Power dissipation limits imposed on the chosen magnetic core by Curie temperature and critical heat flux. (b)Temperature difference from fluid to core surface and from core surface to centre at the Curie temperature limit. 91
6.8 Measured volumetric power dissipations for different flux densities and excitation frequencies (shown as dots). Steinmetz equation fits are also shown as straight lines. 93
6.9 Predicted peak flux density as a function of frequency for different heat transfer coefficients at the core surface. Experimentally measured values for the core immersed in Novec 7000 are also displayed. 94
6.10 Plots showing dimensions of transformers cooled in air, oil and Novec 7000. 96

7.1 Diagram showing section view of alternative heat exchanger structure which minimises separation between dielectric fluid and water-glycol coolant. 104

C.1 $\phi(d_{\mathrm{cr}})$ plotted as a function of core diameter. Also shown is the right hand side of Equation C.2) for various values of Curie temperature. 116

List of Tables

2.1 Candidate working fluids and their physical properties. All are specified at 25 °C except for boiling point and latent heat which are at atmospheric pressure. 13
2.2 Thermal performance and system properties of single and two phase cooling techniques. 26

3.1 Thermophysical properties for candidate dielectric fluids. Liquid properties are at 25 °C while phase change properties are at atmospheric pressure. 33
3.2 Comparison of data-sheet values for latent heat at atmospheric pressure boiling point with calculations via Equation. 3.3. 34
3.3 Summary of sources of experimental uncertainty. 43
3.4 Parameters used to evaluate the Rohsenow correlation for different portions of the pool boiling curve. 47

4.1 Experimental uncertainties on calculated quantities for smooth and grit blasted heat spreader facsimiles. 59

6.1 Heat transfer coefficients for different magnetic component cooling techniques. These are selected based on values proposed in the respective reference. 80
6.2 Calculated and experimentally determined values of critical heat flux and failure current for different wire diameters. 87
6.3 Failure currents for 300/46 Litz wire cooled by air, oil and Novec 7000. 89
6.4 Material properties and dimensions of the Fair-rite 5977001401 magnetic core. 90
6.5 Design parameters and calculated volume for transformers cooled in air, oil and boiling Novec 7000. 96

List of Abbreviations

CHF . . . . . . Critical Heat Flux.

CSPI . . . . . . Cooling System Performance Index.

DBC . . . . . . Direct Bonded Copper, referring to power module substrate.

DC-DC . . . . Direct current to direct current, referring to power conversion.

ENIG . . . . . Electroless Nickel Immersion Gold.

GTO . . . . . . Gate Turn On, referring to thyristor switches.

HEPI . . . . . Heat Exchanger Performance Index.

PCB . . . . . . Printed Circuit Board.

PEEK . . . . . Polyetheretherketone.

PTFE . . . . . Polytetrafluoroethylene.

NCG . . . . . . Non-Condensible Gas.

TIM . . . . . . Thermal Interface Material.

Nomenclature

. . . .

Symbols

A Area [m^2]

a Steinmetz equation frequency exponent

α Temperature coefficient [1/K]

b Steinmetz equation flux density exponent

ΔB Peak flux density [T]

Bi Biot number

Bo Bond number

$C_{\mathbf{sf}}$ Rohsenow correlation surface-fluid fitting coefficient

c Steinmetz equation coefficient

$c_{\mathbf{p}}$ Specific heat capacity [J/(kg K)]

d Diameter [m]

d_0 Bubble diameter [m]

δ Condensate film thickness [m]

$\delta_{\mathbf{e}}$ Skin depth [m]

f Frequency [Hz]

g Acceleration due to gravity [m/s^2]

h Heat transfer coefficient [W/(cm^2 K)]

k Thermal conductivity [W/(m K)]

$k_{\mathbf{E}}$ Eötvös constant [J/K/mol$^{\frac{2}{3}}$]

L Fin length [m]

$l_{\mathbf{lv}}$ Latent heat [J/kg]

μ Dynamic viscosity [Pa s]

$\mu_{\mathbf{m}}$ Magnetic permeability [H/m]

M Molar mass [kg/mol]

m Rohsenow correlation Prandtl number exponent

N Number of segments, fins, wires, strands

n Rohsenow correlation exponent

ρ Density [kg/m^3]

$\rho_{\mathbf{e}}$ Electrical resistivity [Ω m]

P Pressure [Pa]

Pr Prandtl number

Q Heat [W]

q Heat flux [W/cm^2]

$q_{\mathbf{chf}}$ Critical heat flux [W/cm^2]

$q_{\mathbf{zub}}$ Zuber estimate of critical heat flux [W/cm^2]

Q''' Volumetric power dissipation [W/cm^3]

R Universal gas constant [J/(K mol)]

r Radial distance [m]

$r_{\mathbf{p}}$ surface roughness [µm]

T Temperature [°C]

$t_{\mathbf{f}}$ Fin width [m]

$t_{\mathbf{sp}}$ Heat spreader baseplate thickness [m]

V Voltage [V]

ν Volume [m^3]

x Distance along fin length [m]

Δx Fin segment length [m]

Subscripts

atm At atmospheric pressure

b Condenser fin base

c Component surface

conv Converter

cr Magnetic core, Curie temperature

crit Critical point

f Fin

fl Flow side inlet

hex Heat exchanger

i Index

j Semiconductor junction

l Liquid property

r Reduced (pressure or temperature)

s Saturation

st Strand, referring to Litz wire

sw Switch, switch-level

v Vapour property

w Wire

1 Introduction

1.1 Motivation

Power converters interface electrical power sources to loads in a range of applications spanning grids, electric vehicles and consumer electronics. In general they consist of semiconductor switches, magnetic components (like transformers and inductors), capacitors and support systems (including gate drivers, power supplies and microcontrollers). These components lose power in the form of heat during operation. An important challenge relates to packaging the power converter so that heat can be extracted to ambient air or a liquid coolant without the temperature exceeding the rating of any electronic component.

1.1.1 Semiconductor Switches

In many power converter topologies, semiconductor switches produce the majority of heat losses [1]. Power modules have emerged as the industry standard for power semiconductor packaging. The structure of a conventional module is depicted in Fig. 1.1.

Within the module, bare die switches are attached to a Direct Bonded Copper (DBC) substrate via a soldering or sintering process. The substrate comprises a ceramic, which electrically isolates switches from the heat sink, sandwiched between two copper layers. Electrical connections are made amongst switches via aluminium

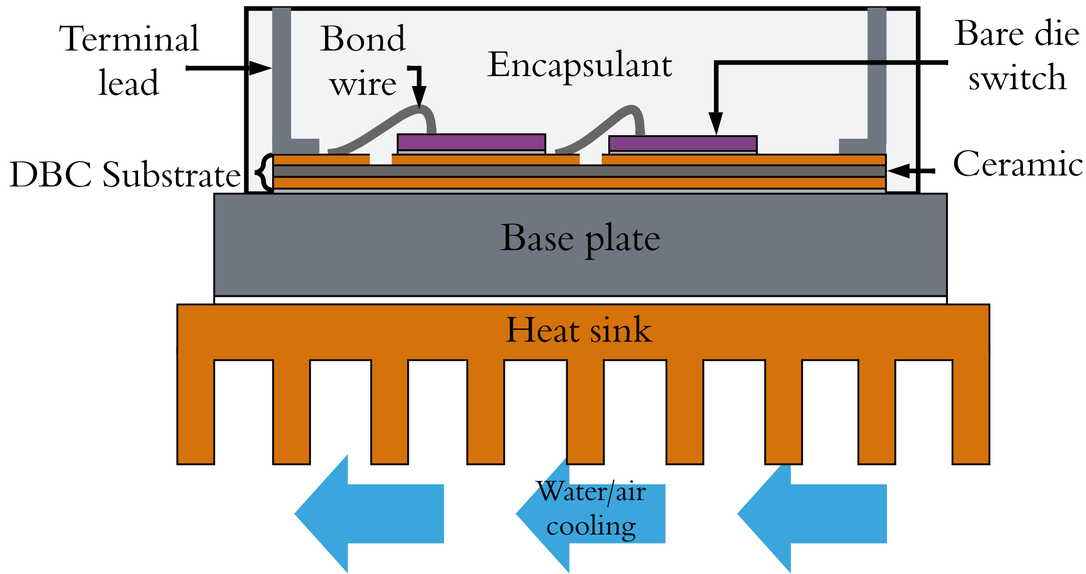

Figure 1.1: Diagram of a conventional power module.

wires which are ultrasonically bonded to metallised pads on top of the switch. Switches and substrate are encapsulated in an epoxy resin or silicon gel, which provides chemical and mechanical protection along with electrical isolation to the package [2]. Gate drivers and ancillary components are usually mounted on printed circuit boards external to the module and connected to it via terminal leads.

In a power module, heat is removed from the die by thermal conduction through the substrate and baseplate to an air-cooled heat sink or liquid cold plate. The baseplate is usually integral to the module structure and serves to spread heat laterally and provide mechanical support. The ceramics used are highly thermally conductive and electrically isolating, which limits the range of materials. For example, aluminium nitride has thermal conductivity of 170 W/(m K) [3], which is comparable with some grades of aluminium alloy. Power modules are therefore the technology of choice for converters which impose high power dissipations on the semiconductor switches.

For applications like electric vehicle motor drive inverters where space is constrained by the battery pack and motor, it is desirable to maximise the power density. This is a measure of converter power normalised by its volume, usually expressed in kW/L. A review of commercial, power module inverters up to 2016

demonstrates maximal power density of 22.6 kW/L [1]. By employing emerging wide band-gap semiconductors and innovative liquid cooling solutions, inverters like the Danfoss DCM1000X exhibit power density of 80 kW/L [4]. This is significantly higher than the Automotive Centre UK Technology Roadmap 2030 target of 35 kW/L [5].

However, a major disadvantage of power module packaging relates to the use of internal wire bonds and terminal leads for electrical connection. These introduce parasitic inductance into the power and gate loops of a circuit. During switching transitions this can cause a switch voltage to overshoot its eventual steady state value by an amount proportional to the parasitic inductance [6], potentially causing failure of the switch.

To address this issue, an alternative approach is to mount semiconductor switches on a printed circuit board (PCB) substrate, as shown in Fig. 1.2. PCB substrates offer several favourable attributes which facilitate minimisation of the parasitic inductance. Firstly, electrical connections are made via conductive traces and plated through holes in the board, which can minimise the conductor loop area compared with a wire bond and terminal lead approach [7]. Furthermore, decoupling capacitors and gate drivers can be integrated on the board in close proximity to the switches, respectively reducing the parasitic power and gate loop inductance [8]. This is not feasible with power modules, where capacitors and gate drivers are mounted on circuit boards external to the module package. A 650 V, 30 A half bridge converter on PCB substrate developed in [7] demonstrates power loop inductance of 1.03 nH and gate loop inductance of 0.34 nH. These are respectively 4 and 30 times lower than the best comparable wire-bonded power module solution in literature.

A possible cooling approach for a PCB-based converter is also shown in Fig. 1.2. The semiconductor switches are thermally coupled to a heat sink via a thermal interface material (TIM). This layer must be sufficiently soft to conform with microscopic surface defects and should also provide electrical isolation. This significantly limits the choice of material; most commercial solutions consist of

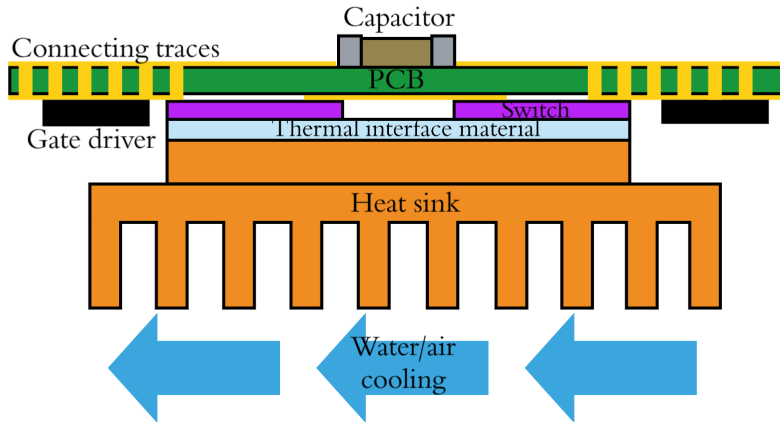

Figure 1.2: Diagram of a possible PCB substrate converter.

a silicone matrix enhanced with thermally conductive fillers like boron nitride [9]. To the author's knowledge, the best commercially available material exhibits thermal conductivity of 17.8 W/(m K) [10], ten times lower than aluminium nitride ceramics used in module substrates. This material usually accounts for a significant portion of the switch temperature increase above ambient and limits the achievable power density of PCB-based converters.

1.1.2 Magnetic Components

Another class of power electronic component which can dissipate significant heat is magnetics. These consist of one or more current carrying coils wound on a core which contains the magnetic field. An important application is the transformer in many DC-DC converter topologies, which provides voltage gain while maintaining galvanic isolation between the power source and load. In low voltage converters, the transformer is usually cooled by natural air convection or airflows driven by a fan. Due to poor heat transfer associated with air convection, the transformer typically contributes a significant portion of the overall converter volume, limiting the achievable power density. The Automotive Centre UK 2030 target for DC-DC converters is only 3 kW/L [5], almost 12 times lower than for inverters which typically do not have magnetic components in the main power path.

High-voltage transformers used in power transmission are often immersed in

tanks of mineral oil. This ensures electrical isolation between the transformer and its enclosure while cooling it more effectively via liquid convection. However, due to concerns surrounding flammability of oils, it is beneficial to develop novel cooling techniques which rely on non-flammable dielectric fluids [11].

1.1.3 Two-phase Immersion Cooling

Conventional cooling for power converters on PCB substrates are limited by poor thermal conductivity of interface materials or low heat transfer rates associated with air convection. Alternative concepts have been proposed in literature which attempt to cool components more effectively by bringing them into close contact with dielectric fluids. One approach is two-phase immersion cooling where components are submerged in a closed pool and heat is transferred from the surface of electronic components by boiling of local liquid. The vapour rises and condenses in contact with an air or water cooled heat exchanger which is positioned so condensate can return to the pool under gravity.

A possible implementation of two-phase immersion cooling for power electronics components on PCB substrates is shown in Fig. 1.3. The dielectric liquid is enclosed by two chambers which seal respectively to the top and bottom sides of the PCB. This accommodates cut-outs or plated holes in the circuit board and ensures equalisation of pressure on both sides to reduce mechanical stress. A portion of the PCB extends beyond the chamber walls to make connections with external power sources and circuitry. The heat exchanger is integrated into the top side chamber. The condenser side of the heat exchanger features downward facing fins to increase surface area and promote gravity-driven return of condensate. The flow side features channels for pumped liquid coolant. This approach offers several attractive features:

- The dielectric fluid provides electrical isolation between electronic components and the heat exchanger with no requirement for thermal interface materials which tend to have low thermal conductivity.

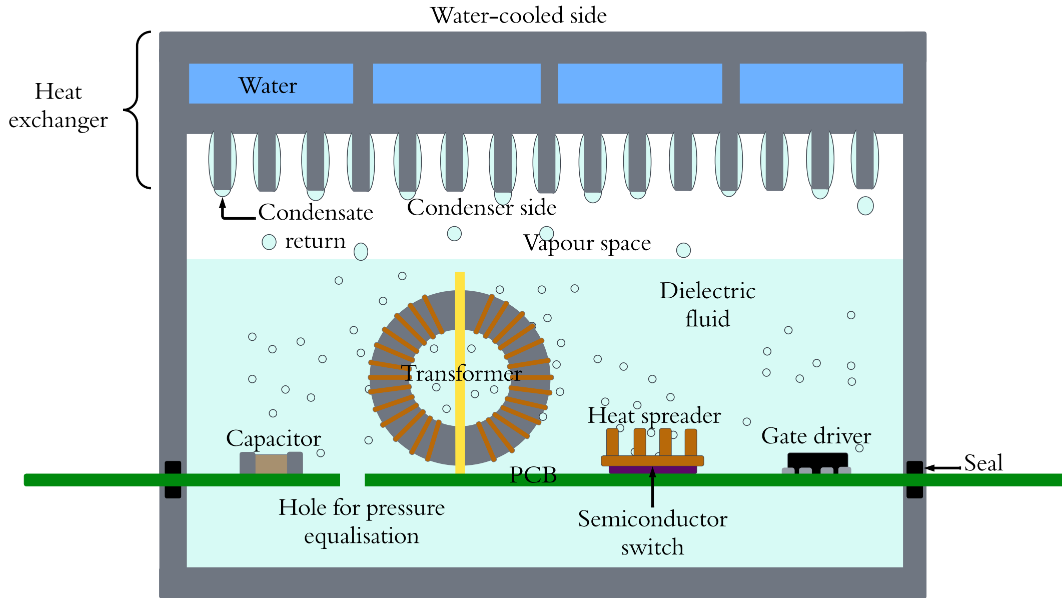

Figure 1.3: Diagram of proposed two-phase immersion cooling for PCB substrate converters.

- Fluid is passively circulated by cyclical boiling, condensation and gravity-driven return of condensate. This reduces system complexity by eliminating the need for additional pumps and piping beyond what is already available in conventional converter cooling systems.
- It may be possible to improve system-level power density by immersing the entire converter rather than just the semiconductor switches. More effective cooling compared with air convection could enable operation of magnetic components at more extreme conditions and facilitates reduction in their size.

1.2 Contribution

This thesis explores the potential for two-phase immersion cooling to facilitate high power density converters on PCB substrates. The target application is an electric vehicle motor drive in which heat is rejected to a water-glycol liquid cooling loop at 65 °C, as specified by the Automotive Centre UK [5]. Several pertinent research questions have been identified based on gaps in the existing literature.

1. **Identifying the limits of boiling heat transfer performance for planar horizontal switches in closed systems**. Much prior research has focused on characterising heat transfer rates for dielectric fluids boiling on planar horizontal surfaces representative of semiconductor switches. However, these experiments are typically conducted at the fluid atmospheric pressure boiling point in open pools. This work targets sealed systems evacuated of air, which operate under pressure corresponding to the fluid's saturation temperature. An important area of research therefore relates to theoretical and experimental characterisation of boiling heat transfer metrics for dielectric fluids at elevated saturation temperatures and pressures.

2. **Exploring improvements in boiling heat transfer for semiconductor switches with finned heat spreaders**. Previous studies have reported significant improvements in boiling heat transfer from semiconductor switches by attaching finned heat spreaders to increase the surface area. However, they did not examine systematic design of the heat spreader geometry for switches in PCB converters. Modelling of heat transfer from fins is complicated by the non-linear nature of boiling phenomena. A second avenue of investigation therefore relates to development of simple yet accurate models which can instruct design of heat spreaders subject to space constraints imposed by the PCB substrate.

3. **Design and evaluation of a complete sealed two-phase immersion cooling system targeting high thermal power density**. There are few studies in literature which consider the performance of two-phase immersion cooling systems including the heat exchanger. In order to achieve high thermal power density, it is necessary to develop high performance, compact heat exchangers. Furthermore, mechanisms for sealing the dielectric fluid pool between the chamber and PCB substrate are required which minimise the impact of non-condensible gases leaking into the system.

4. **Characterisation of the reduction in size of two-phase immersion cooled power magnetic components**. Boiling heat transfer is orders of magnitude more effective than air convection. It may therefore be possible to operate two-phase immersion cooled inductors and transformers with higher current density in the coils and magnetic flux density in the core. This can facilitate reduction in their size and may contribute substantially to the development of high power density DC-DC converters for electric vehicles.

The thesis is structured as follows. Chapter 2 presents a review of existing literature on two-phase immersion cooling for electronics applications and introduces the heat transfer coefficient and critical heat flux as performance metrics. Chapter 3 details theoretical models of boiling and a test apparatus/procedure used to characterise boiling heat transfer from various power electronic components. Novec 7000 from 3M is selected as the most promising candidate dielectric fluid. Chapter 4 describes a theoretical model and numerical solution procedure used to evaluate boiling heat transfer on finned heat spreaders. Chapter 5 presents a practical two-phase immersion cooling system design for a motor drive inverter in order to evaluate electrical and thermal power densities. Experiments are presented demonstrating reliability of the PCB substrate sealing approach. In Chapter 6, experiments are conducted with immersed copper wire coils and ferrite cores, demonstrating their operation at high current and magnetic flux densities. These results are used to evaluate potential reductions in size for a two-phase immersion cooled transformer compared with air or oil.

2

Literature Review

2.1 Boiling Heat Transfer Background

2.1.1 Boiling Concepts

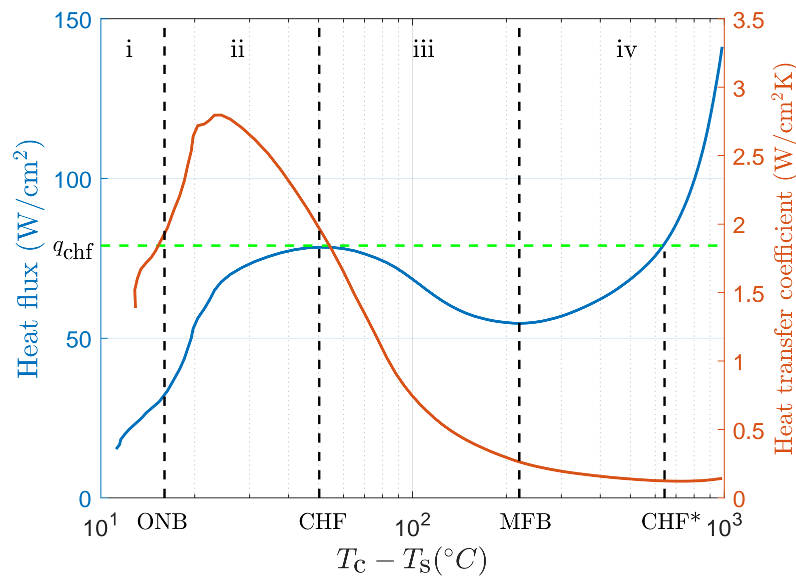

Figure 2.1: Boiling curve and corresponding heat transfer coefficients for water on platinum wire. Reproduced from data published in [12].

Prior research on two-phase immersion cooling has focused on characterising boiling heat transfer on surfaces representative of electronic components immersed in pools of dielectric fluid. The pool is maintained at a constant saturation temperature

T_s. T_c represents the component's temperature at the surface which is exposed to the liquid. It varies in response to the component power dissipation Q_c. The boiling heat transfer coefficient defined in Equation 2.1 provides a performance metric normalised to the heat transfer area A_c.

$$h = \frac{Q_c}{A_\mathrm{c}(T_c - T_\mathrm{s})} \tag{2.1}$$

Another important property unique to two-phase systems is the critical heat flux (CHF) defined by Equation 2.2. It represents the maximum power dissipation per unit area and arises due to instabilities in the boiling process which cause the component surface to become crowded with vapour.

$$q_\mathrm{chf} = \frac{\max\left(Q_\mathrm{c}\right)}{A_\mathrm{c}} \tag{2.2}$$

These quantities can be interpreted as features on the pool boiling curve. It provides a graphical relationship between heat flux through the component surface and its temperature rise above the surrounding fluid. Fig. 2.1 displays one such curve for water boiling on platinum wire at atmospheric pressure. Several distinct regimes of behaviour were identified in [12] and are detailed below. Corresponding heat transfer coefficients are also plotted to show relative magnitudes of heat transfer in the different regimes.

- Section (i) exhibits natural convection behaviour. The component's surface temperature is insufficient to generate vapour bubbles; instead, heat is transferred via buoyancy driven convection currents. In this region, the heat transfer coefficient is much lower than in the nucleate boiling regime.

- Point ONB represents the onset of nucleate boiling. This is the lowest temperature sufficient to sustain stable vapour bubbles in microscopic surface cavities. Once a bubble nucleates, it is theorized the bubble's growth spreads to neighbouring cavities, initiating boiling across the entire surface [13].

- Section (ii) is the nucleate boiling regime. Heat transfer is driven by periodic formation, growth and departure of bubbles. The heat transfer coefficient increases substantially with increasing surface temperature and the highest absolute value is observed in this portion of the curve.

- Point CHF is the critical heat flux. Hydrodynamic instabilities cause vapour transport mechanisms to break down and portions of the surface become crowded with vapour.

- Section (iii), known as transition boiling, is only observable experimentally when the surface temperature is controlled rather than the heat flux. In this regime, an increasing portion of the heater surface is blanketed by vapour leading to reduction in heat transfer coefficient with surface temperature.

- Point MFB, the minimum film boiling point, is the smallest heat flux with sufficient generation of vapour to maintain a stable film across the entire surface

- Section (iv) is the film boiling regime where a stable vapour layer covers the entire surface. Heat transfer occurs by thermal conduction through the vapour and at very high surface temperatures, thermal radiation.

In electronics applications, the heat flux is set by the power dissipation of a given component. When the critical heat flux is just exceeded, the surface temperature will rapidly increase through the transition and film boiling regimes until a steady state is reached at point CHF*, which is observed at 640 °C in Fig. 2.1. It is vital to ensure this does not occur to prevent thermal failure of the component. Consequently, only the nucleate boiling regime is important and critical heat flux represents a practical limit on the amount of heat that can be extracted per unit area.

2.1.2 Fluid Selection

While heat transfer during nucleate boiling is not fully understood, there are several proposed mechanisms which provide insight into key fluid properties. Cyclic growth and departure of bubbles in surface cavities induces circulation of the surrounding liquid. This is conceptually similar to forced convection [14] and favours use of low viscosity fluids. Another proposed mechanism is conduction through a thermal boundary layer adjacent to the surface which is periodically stripped away in the wake of departing bubbles. High thermal conductivity fluids are therefore required. The latent heat is another crucial parameter which should be maximised, impacting the rate of vaporisation during the growth of bubbles.

For power electronics applications, several electrical parameters of fluids need to be considered. The breakdown electric field should be high enough so that target voltage can be met without requiring large spacing between conductors which compromises electrical design. The dielectric constant should also be minimised. Fluids with high dielectric constants have highly polar molecules and effectively dissolve ions which can form electrically conductive paths between components and their enclosure [15]. Table 2.1 summarises the properties of several candidate fluids for two-phase immersion cooling of power electronics. Included in this selection are a Fluroinert (FC72) and a Novec fluid from 3M. These are engineered to provide high breakdown strength, low dielectric constant and widespread chemical compatibility. Deionized water has significantly improved thermal conductivity and latent heat but is a highly effective solvent for ionic compounds as indicated by its high dielectric constant. Organic solvents like methanol exhibit lower dielectric constant than water but are rarely used due to concerns surrounding chemical compatibility or flammability [15].

Table 2.1 also shows the atmospheric pressure boiling point T_{atm} for each fluid. This determines the temperature at which an open pool at atmospheric pressure P_{atm} will boil. In practical two-phase immersion cooling systems, the fluid is enclosed in a sealed chamber which has been evacuated of air prior to filling. The fluid is therefore in a saturation state and boils at a temperature and dependent

Table 2.1: Candidate working fluids and their physical properties. All are specified at 25 °C except for boiling point and latent heat which are at atmospheric pressure.

	FC72 [16]	**Novec 7000** [17]	**Methanol** [18] [19]	**Water** [20] [19]
Liquid thermal conductivity (W/(m K))	0.057	0.075	0.200	0.598
Liquid dynamic viscosity (mPa s)	0.640	0.450	0.544	0.890
Latent heat (kJ/kg)	88	142	1099	2256
Boiling point(°C)	56	34	65	100
Critical temperature(°C)	176	165	239	374
Liquid dielectric constant	1.75	7.40	32.70	80.10
Liquid dielectric strength (kV/mm)	>15	>10	N/A	N/A

pressure determined by heat flows through the system. In general, there exists a logarithmic relationship between saturation pressure P_s and temperature T_s which can be modelled to a first approximation by the Clausius-Clapeyron equation [14].

$$\ln\left(\frac{P_\mathrm{s}}{P_\mathrm{atm}}\right) = -\frac{l_\mathrm{lv}}{R}\left(\frac{1}{T_\mathrm{s}} - \frac{1}{T_\mathrm{atm}}\right) \tag{2.3}$$

In [21], it is observed for methanol, pentane and water that both heat transfer coefficient and critical heat flux increase with saturation pressure and temperature due to changes in physical properties. Fluids with low atmospheric pressure boiling points may therefore exhibit substantial improvements in performance at the elevated temperatures observed in power electronic systems. This comes at the expense of higher system pressure via Equation 2.3 and thus greater mechanical stress on the fluid chamber. Most prior work uses Fluorinert or Novec fluids with boiling points between 30 °C and 60 °C.

A final consideration is the critical temperature, beyond which no liquid phase

exists and the fluid behaves as a gas. Critical temperatures for FC72 and Novec 7000 exceed junction temperature ratings for most power semiconductor switches (150 °C) though they may be unsuitable for use with silicon carbide devices, some of which are rated up to 200 °C.

Several studies have characterised the boiling behaviour of candidate fluids under saturation conditions. The fluid is either open to atmospheric pressure or enclosed in a chamber with the saturation temperature and pressure set by a controllable heat exchanger. In rare cases, boiling is characterised in a sub-cooled mode when the surface is sufficiently hot to nucleate bubbles though the bulk liquid has not yet reached its saturation temperature at system pressure. Several works have reported improvements in heat transfer coefficient and critical heat flux when the liquid is sub-cooled [22] [23]. Unless stated otherwise, results from studies reviewed in this thesis are under saturated rather than sub-cooled conditions.

Experiments with Fluorinert and Novec fluids boiling at atmospheric pressure on smooth, planar surfaces indicate they exhibit effective heat transfer coefficients below 1 W/(cm K) and critical heat fluxes below 30 W/cm^2 [24] [25] [26]. It is anticipated that demanding power electronics applications will impose heat flux requirements in excess of 300 W/cm^2 [27]. Consequently, a considerable quantity of research has focused on identifying candidate fluids with better thermophysical properties. One approach is to design new specialist fluids which are chemically inert and electrically isolating. Computer aided molecular design was employed to identify 35 fluids with improved thermal performance based on metrics defined in terms of the latent heat, thermal conductivity and liquid viscosity [28] . $C_6H_{11}F_3$ was selected as the best performing fluid for which a synthesis procedure has been detailed in literature. Since only a small quantity of the compound could be synthesized, a mixture of 7 % by weight $C_6H_{11}F_3$with Novec 7200 was tested, yielding an improvement in CHF by 6.9 % compared with pure Novec 7200. In another work, commercially available molecule $C_4H_{11}F_6$was identified via computer aided design and tested as part of a 10 % by weight mixture with Novec 7200, increasing critical heat flux by 8.4 % [29]. While several promising candidates have been identified, only minor improvements

in boiling heat transfer have been demonstrated thus far and their use is limited by commercial unavailability and lack of knowledge about synthesis procedures.

Another approach is to develop engineering solutions which facilitate use of deionized water or organic solvents. Water is an attractive candidate due to its exceptional thermal properties; critical heat flux at atmospheric pressure on a smooth surface was reported as 140 W/cm^2 [21]. To overcome electrical conduction issues, it is proposed to coat circuit boards and electronic components with micrometer thick layers of electrically insulating Parylene-C [30]. Coating thicknesses ranging from 1 µm to 25 µm were achieved using a chemical vapour deposition process. Coated semiconductor switches were immersed in a pool of water open to atmosphere and maintained at room temperature, such that boiling occurs in the sub-cooled mode. For the 1 µm coating, a switch level critical heat flux of 342 W/cm^2 was reported with maximal heat transfer coefficient of 1.8 $W/(cm^2\,K)$. However, the dielectric strength of the coating is only 78 V/µm. For applications like electric vehicles, 400 V DC links are the norm and 800 V links are increasingly common, so coating thicknesses in excess of 10 µm are required. Calculations indicate that coatings thicker than 10 µm yield lower heat transfer coefficients in water than for uncoated surfaces in Novec 7300. This is due to the thermal resistance associated with conduction through Parylene-C, which has a low thermal conductivity of 0.1 W/(m K). It is clear the technology in its current form is only suitable for low voltage applications where very thin coatings can be tolerated.

Alcohols have also shown potential for two-phase immersion cooling. Methanol boiling at atmospheric pressure on a smooth surface exhibits critical heat flux of 70 W/cm^2 [21]. Ethanol has slightly worse thermal properties with critical heat flux of 49 W/cm^2 [31] though is more chemically benign. A practical two-phase immersion cooling concept with ethanol was presented in [32]. Bare die semiconductor switches are packaged in a sealed, evacuated heat pipe made from copper and cold rolled steel filled with ethanol. This work lends support to the notion that electrical conduction and chemical compatibility issues for organic solvents can be addressed. Nevertheless, only dielectric fluids will be considered in the remainder of this thesis.

2.2 Boiling Heat Transfer for Semiconductor Switches

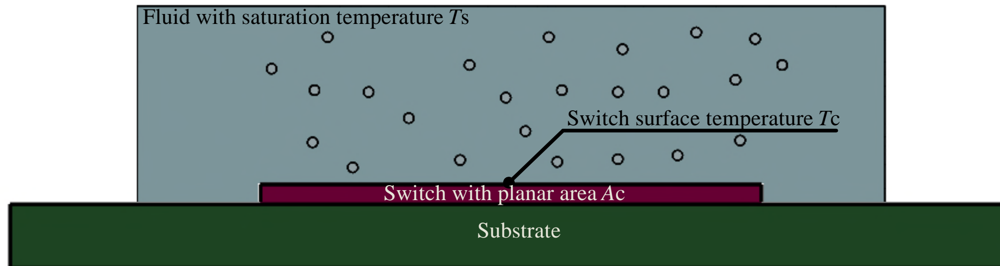

Figure 2.2: Diagram of an immersed semiconductor switch.

For the immersed semiconductor switch shown in Fig. 2.2, boiling can be characterised directly via the heat transfer coefficient and critical heat flux of Equations 2.1 and 2.2 calculated relative to the planar switch area. Given the performance limits of dielectric fluids established in the previous section, a significant portion of existing literature has focused on enhancing boiling heat transfer by altering the switch surface geometry. Micro-scale features are employed to favourably influence bubble behaviour, increasing the heat transfer coefficient and critical heat flux. On the other hand, millimetre scale features are used to increase the heat transfer area in contact with liquid for the same semiconductor footprint.

2.2.1 Switch Surface Micro-Enhancement

The primary function of switch surface micro-geometry modification is to create more cavities for bubble nucleation. This can be achieved using relatively simple methods like applying abrasive media to the surface. In [24] emery paper with different grit counts was used to prepare copper surfaces with average roughness varying from 0.039 µm to 0.58 µm. This produces a structure of parallel grooves as shown in Fig. 2.3a for the roughest surface. Critical heat flux for Novec 7000 at atmospheric pressure increased from 21.6 $\mathrm{W/cm^2}$ to 30 $\mathrm{W/cm^2}$ with increasing surface roughness. The heat transfer coefficient increased from 0.8 $\mathrm{W/(cm^2\,K)}$ to 1.9 $\mathrm{W/(cm^2\,K)}$.

Vapour blasting using a water based slurry with grit silica particles was applied

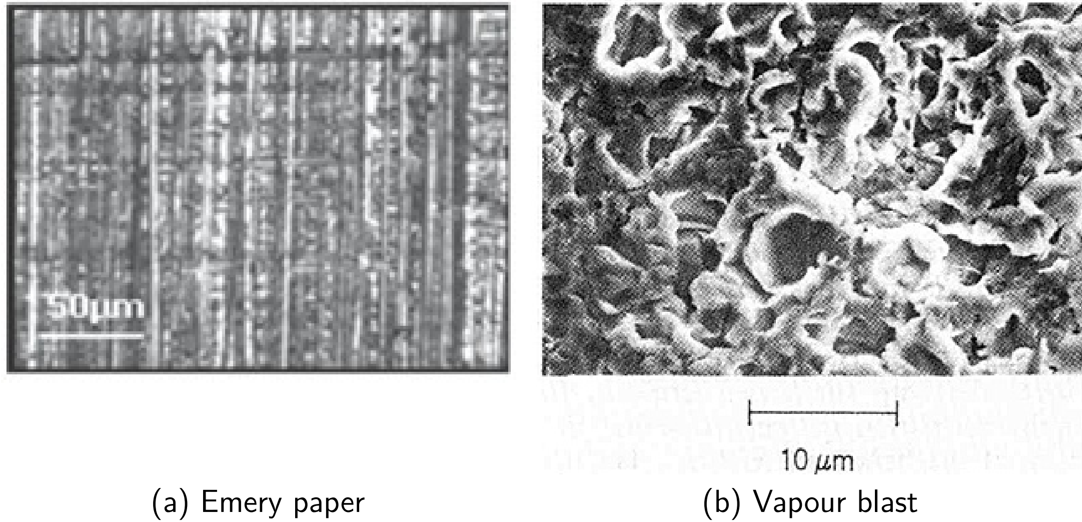

(a) Emery paper (b) Vapour blast

Figure 2.3: Scanning electron microscope images of surfaces treated with emery paper and vapour blasting. Reproduced from [24] and [26] respectively.

to a copper surface in [26]. As shown in Fig. 2.3b, this process removes features left by machining or polishing steps and produces a random structure of cavities. Only a minor increase of critical heat flux from 19.8 W/cm^2 to 20.5 W/cm^2 was reported for FC72. However, more significant improvements have been observed by sand blasting, which uses more abrasive dry media. In [33] surfaces with average roughness up to 9 μm were prepared in this way. The roughest surface yielded improvements in critical heat flux by factor of 1.5 and heat transfer coefficient by 3 compared with the smoothest when tested with Novec 649.

Complex surface enhancement methods produce regular patterns of micro-scale features to increase the number of potential nucleation sites and also expand the heat transfer area. For example, square studs of width 0.305 mm and depth 0.508 mm were cut into a copper surface, achieving critical heat flux of 51 W/cm^2 in FC72 at atmospheric pressure [26]. Micro-machining techniques have been employed to achieve smaller feature sizes by etching directly into silicon substrates. Square pin fins of thickness 50 μm with heights ranging from 60 μm to 270 μm (shown in Fig. 2.4) were tested in FC72 [34]. The maximum CHF reported was 33 W/cm^2 with heat transfer coefficient exceeding 2 W/(cm^2 K).

Much like machined micro features, microporous surface coatings can provide

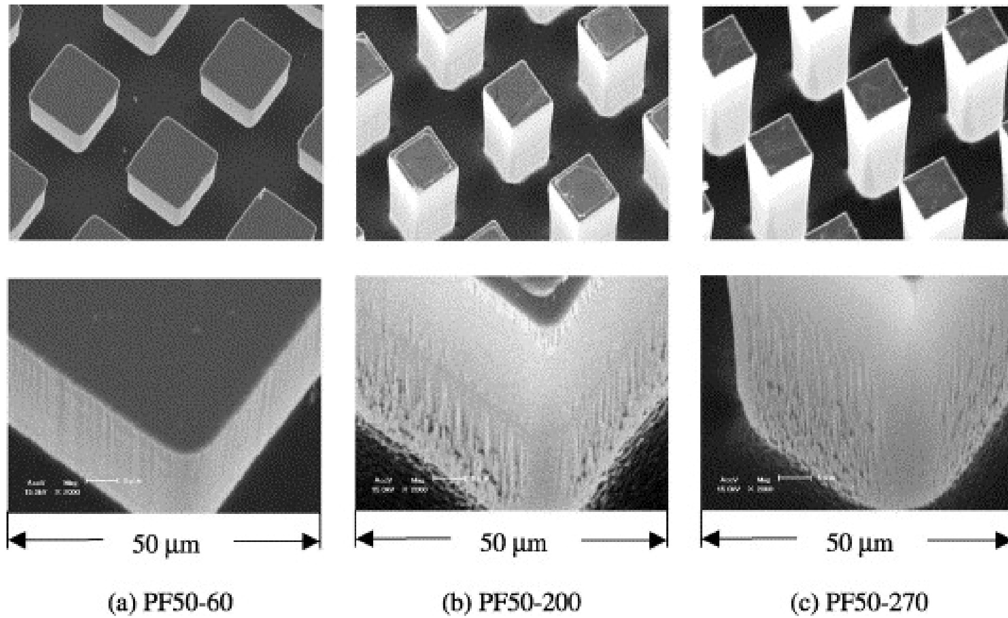

Figure 2.4: Scanning electron microscopy images of 50 µm fins with heights 60 µm, 200 µm and 270 µm respectively. Reproduced from [34].

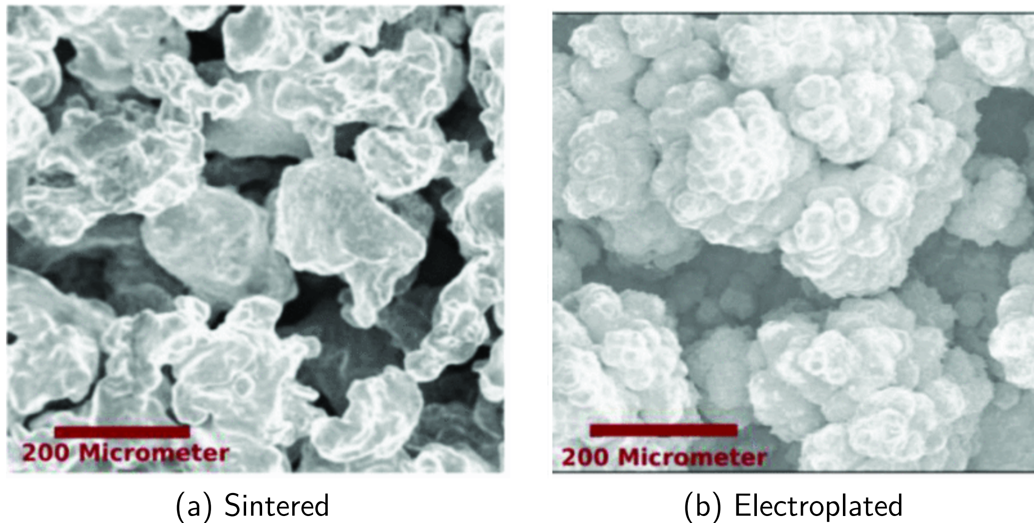

Figure 2.5: Scanning electron microscope images of sintered and electroplated microporous copper coatings. Reproduced from [35] ©2022 IEEE.

higher density of nucleation sites and greater heat transfer area. A unique advantage is the improvement of liquid circulation close to the surface due to capillary action through the pores [36]. Commercial microporous coating processes involve sintering copper particles which requires high pressure and temperature. An example is shown in Fig. 2.5a. Such a coating demonstrates heat transfer coefficient $1.15\,\mathrm{W/(cm^2\,K)}$

in saturated Novec 649 compared with $1.01\,\mathrm{W/(cm^2\,K)}$ for copper micro-fins [37]. Electro-plating was explored as an alternative coating method which can be conducted at room temperature and atmospheric pressure, reducing mechanical stress on the semiconductor switch [35]. The porous structure, shown in Fig. 2.5b exhibits greater diversity of pore sizes than the sintered coating, with larger pores nearer the top assisting in circulation of liquid. An improvement in heat transfer coefficient over the sintered coating by factor of 1.5 was reported when tested in Novec 649 [35]. Boiling of FC72 on a porous graphite foam was characterised in [23], with maximal heat transfer coefficient of $3.3\,\mathrm{W/(cm^2\,K)}$ though only a moderate critical heat flux of $28\,\mathrm{W/(cm^2\,K)}$ was reported.

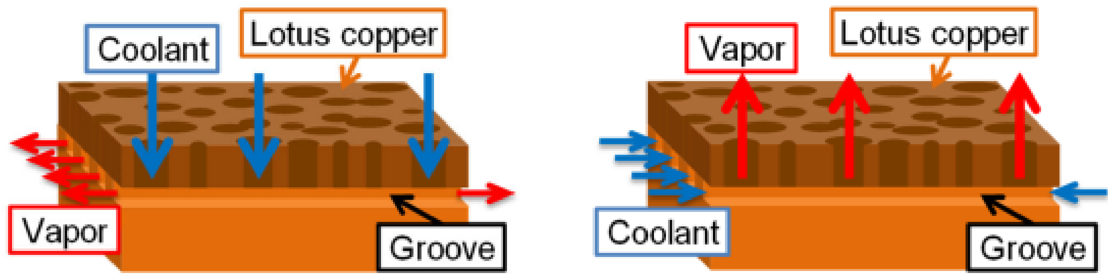

Figure 2.6: Diagrams showing two different breathing modes for lotus copper on grooved surfaces. Reproduced from [38].

Copper structures with pores aligned in one direction are termed lotus copper. They offer higher thermal conductivity in the through-pore direction compared with other porous media [27]. Furthermore, when bonded to grooved surfaces, lotus copper creates a separation between vapour discharge and liquid replenishment routes to the surface; this is known as the breathing effect [38]. Vapour is discharged through grooves or pores depending on the fluid properties and liquid drawn in via the other path as shown in Fig. 2.6. Exceptional critical heat fluxes exceeding $80\,\mathrm{W/cm^2}$ were reported for FC72 boiling on a surface with 1 mm wide grooves and lotus copper with heat transfer coefficients exceeding $3\,\mathrm{W/(cm^2\,K)}$ [39]. To the author's knowledge, this is the best reported performance for dielectric fluid boiling on a surface with only micro-scale enhancement.

2.2.2 Switch Heat Spreaders

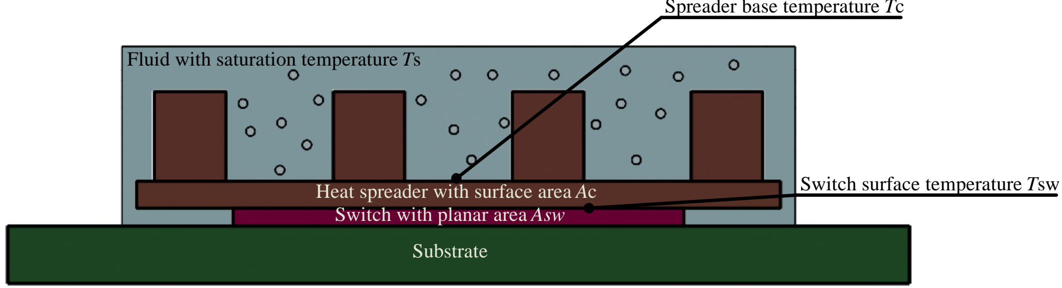

Figure 2.7: Diagram of an immersed semiconductor switch with heat spreader attached.

For very demanding power electronics applications, a heat spreader may be attached to the switch as shown in Fig. 2.7. Through lateral heat spreading and features like fins, the spreader surface area A_c is several times larger than the planar switch area A_sw. The switch-level heat transfer coefficient h_sw can be defined by Equation 2.4.

$$h_\mathrm{sw} = \frac{Q_\mathrm{c}}{A_\mathrm{sw}(T_\mathrm{sw} - T_\mathrm{s})} \tag{2.4}$$

A switch-level critical heat flux q_sw can also be defined. Both of these metrics are normalised to the switch area rather than the spreader area.

$$q_\mathrm{sw} = \frac{\max(Q_\mathrm{c})}{A_\mathrm{sw}} \tag{2.5}$$

Since the surface area in contact with the dielectric fluid is increased by the heat spreader, the switch power dissipation Q_c can be greater for the same switch area. The switch-level heat transfer coefficient and critical heat flux are therefore respectively higher than for a planar surface with no heat spreader. The end result in practical applications is an increase in converter power density for the same semiconductor area.

Arguably the simplest possible heat spreader has planar area equal to that of the switch, with protruding fins utilised to increase the heat transfer area. Different arrangements of cylindrical pin fins machined onto a square copper surface were characterised with saturated FC72 boiling at atmospheric pressure [22]. The highest

switch-level critical heat flux was 105 W/cm^2 for a single fin enhanced with micro-studs along the perimeter. A corresponding switch-level heat transfer coefficient of 5 W/(cm^2 K) was reported. The effect of lateral heat spreading, achieved by designing the heat spreader base to overhang the switch, was investigated in [40]. A 40 mm square copper heat spreader was prepared with an array of 1 mm wide and 4 mm long pin fins enhanced by microporous surface coating. It is shown in Fig. 2.8. The spreader was attached to a number of square copper heaters with lengths varying from 37 mm down to 7.5 mm. The switch-level heat transfer coefficient with Novec 7000 at atmospheric pressure increases from 7 W/(cm^2 K) to 15 W/(cm^2 K) as the switch length decreases due to the contribution of lateral heat spreading.

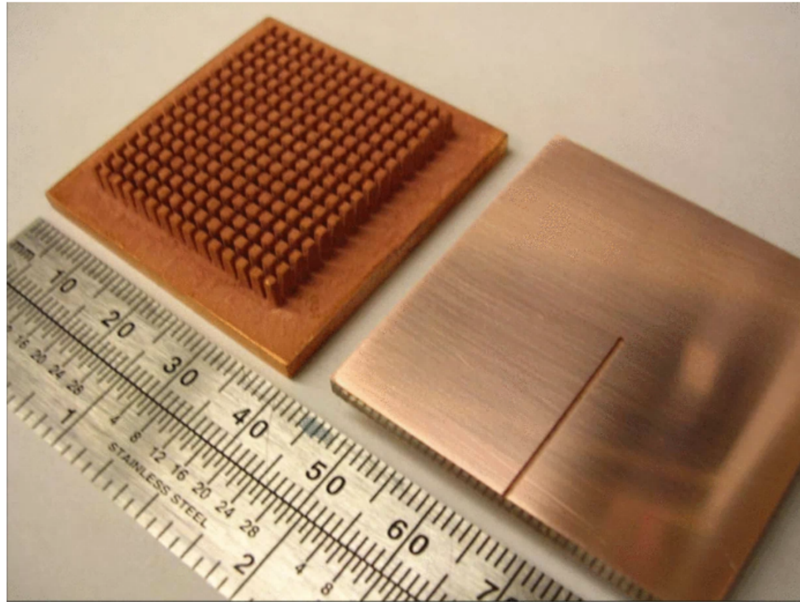

Figure 2.8: Finned heat spreader with microporous coating used to investigate the effect of lateral heat spreading, reproduced from [40] ©2006 IEEE.

Several practical implementations have been explored which address the challenge of attaching heat spreaders to switches. In [41], it is proposed to etch heat spreader structures in silicon, either directly into the switch material or as a separate structure. In the latter case, the heat spreader exhibits minimal mismatch in thermal expansion coefficient with the switch, allowing for a more reliable bond than a metal. Finite element simulations of optimised silicon heat spreaders immersed in FC72 at atmospheric pressure indicate an achievable switch-level critical heat flux

of 51 W/cm^2 [41].

Another approach is to press a heat spreader onto the switch by applying mechanical force. This is a non-permanent attachment which minimises the risk of failure compared with solder bonds, which are susceptible to fatigue under repeated thermal cycles. In [13], a single cylindrical copper fin is pressed onto a representative heater with varying contact pressure. Experiments with FC72 demonstrate a switch-level critical heat flux of 85 W/cm^2. However, comparison with a soldered fin indicates the contact resistance associated with the pressed fin accounts for approximately half of the total thermal resistance.

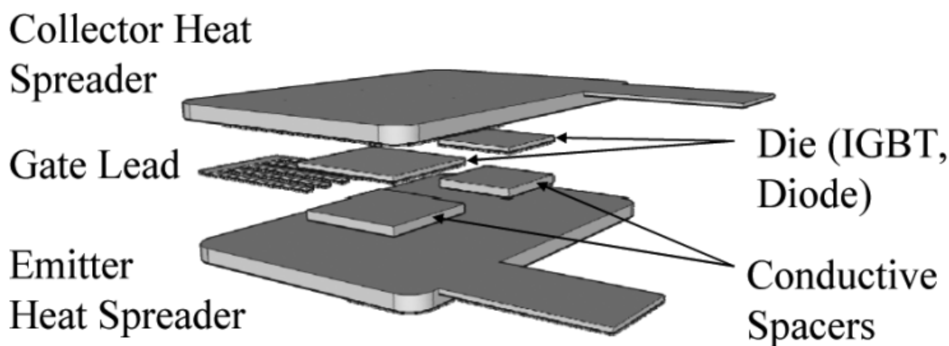

Figure 2.9: Diagram showing assembly with bare die semiconductor switches and heat spreaders to facilitate double-sided cooling. Reproduced from [42] ©2010 IEEE.

In [43], a silicon insulated gate bipolar transistor (IGBT) switch is soldered to a flat heat spreader with twelve times larger planar area, enhanced with a microporous coating. The highest switch-level heat transfer coefficient reported with Novec 7000 is 14 W/(cm^2 K) and the heat flux reaches 400 W/cm^2. In a further work, a 0.144 cm^2 bare die IGBT switch is soldered to two 1.69 cm^2 flat heat spreaders as shown in Fig. 2.9 such that both sides of the switch are cooled. To the author's knowledge this work produced the highest reported boiling heat transfer coefficient of 25 W/(cm^2 K) and critical heat flux of 1180 W/cm^2 at the switch level using Novec 7000 at atmospheric pressure.

2.2.3 Comparison with High Heat Flux Liquid Cooling

It is useful to compare the performance of boiling heat transfer with alternative high heat flux cooling techniques. In general, these are based on forced flow of liquid which does not undergo phase change. It is observed that for very narrow liquid channels, the flow is laminar and heat transfer coefficient increases with decreasing channel width [44]. It is therefore proposed to incorporate micro-scale channels in close proximity to the switch, often by etching into the semiconductor material itself. A water cooled silicon heat sink with 57 µm wide and 300 µm deep channels demonstrates switch-level heat transfer coefficient 11 W/(cm^2 K). The maximum heat flux was 790 W/cm^2, limited only by the switch temperature rise above the water inlet [44]. Micro-channel heat sinks have been combined with arrays of jets impinging on the channel surfaces, making use of high local heat transfer rates around the impingement zones. This was implemented in [45] by bonding separate micro-channel and jet array layers etched in silicon to the switch. Channels of width 150 µm yielded switch-level heat transfer coefficient with water of 11 W/(cm^2 K) [45] at the switch level. Better performance is expected with smaller channels though these were not considered due to fabrication limitations on the jet array.

Recent advances in additive manufacturing techniques facilitate formation of intricate micro-channel structures in metal without significant deterioration of the physical properties. For example, additive manufactured aluminium demonstrates thermal conductivity of 173 W K/m which is comparable to some grades of aluminium alloy [46]. It was used to create a folded heat sink with 250 µm channels and an integrated manifold structure to promote impinging flow. The heat sink, shown in Fig. 2.10, cools two semiconductor switches and has a small lateral footprint; it extends normally outwards from the switch to increase the heat transfer area. Computational fluid dynamics simulations predict a switch level heat transfer coefficient of 6.9 W/(cm^2 K) with water cooling [46].

If water is used as the coolant, an electrically isolating thermal interface material layer is required between the switch as shown in Fig. 2.11. The switch-level heat transfer coefficient for a silicon micro-channel heat sink with 100 µm channels was

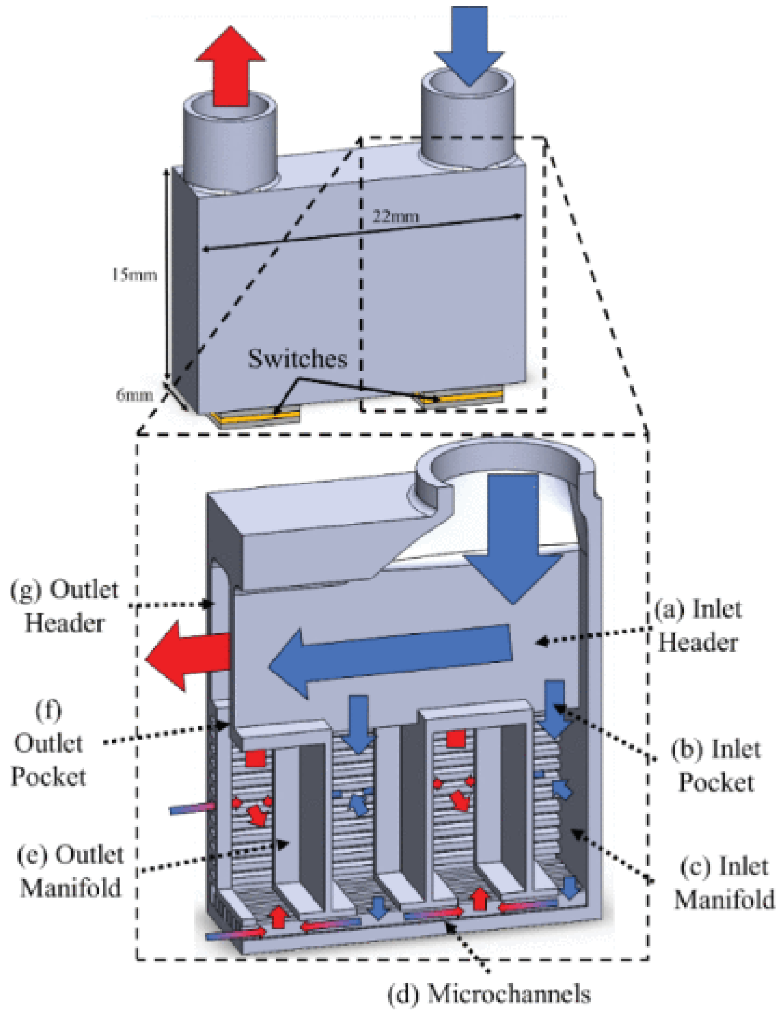

Figure 2.10: Diagram of additively manufactured folded aluminium microchannel heat sink with impinging jet flow. Reproduced from [46] ©2021 IEEE.

measured as 9.1 W/(cm^2 K). This decreased drastically to 0.83 W/(cm^2 K) when mounted on a switch due to conduction through the thermal interface material [47]. Single phase flow with dielectric fluids removes the need for thermal interface materials. Alpha-6 fluid from DSI Ventures was characterised impinging on a finned copper heat spreader. The chosen inter-fin spacing was 250 µm and fin height 4 mm; the switch-level heat transfer coefficient was 5.3 W/(cm^2 K) [48].

Table. 2.2 summarises heat transfer performance of single-phase liquid cooling techniques compared with pool boiling using dielectric liquids. Since the latter utilises passive fluid circulation, no pumping or plumbing components are required beyond a standard electric vehicle water glycol loop save for a heat exchanger to

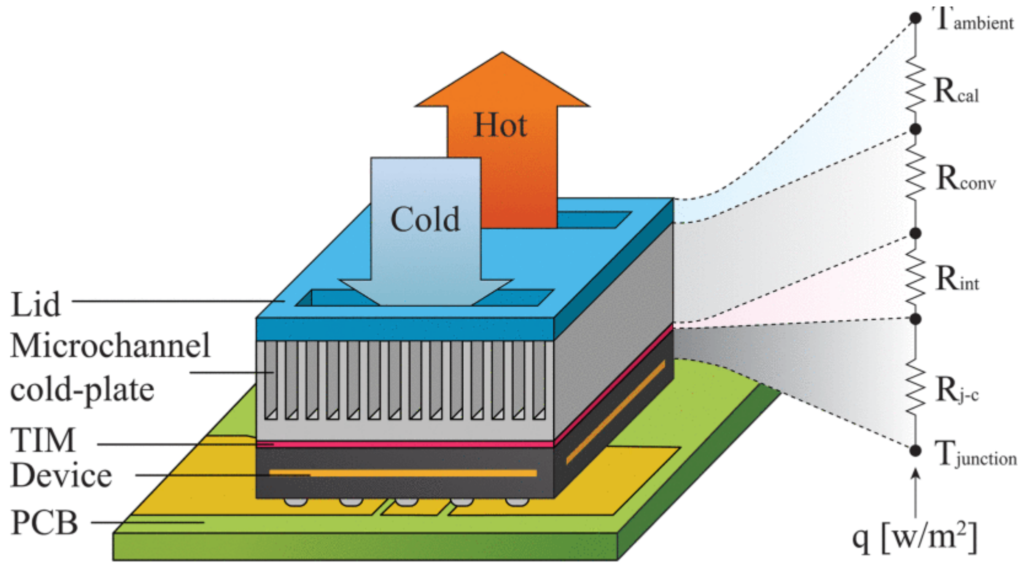

Figure 2.11: Silicon microchannel heat sink coupled to a semiconductor switch by thermal interface material. Reproduced from [47] ©2020 IEEE.

condense the vapour. Single-phase techniques require a pump to circulate fluid and a heat exchanger to reject heat to the water glycol loop. Furthermore, when impinging jets are employed, a manifold structure is required to direct fluid through the jet array. System requirements for each cooling approach are summarised in the final column of Table 2.2. Boiling of dielectric fluids with heat spreaders yields higher heat transfer coefficients than all single phase techniques while integrating electrical isolation and reducing system complexity.

2.3 Two-phase Immersion Cooling Systems

In a practical two-phase immersion cooling system, the dielectric fluid saturation temperature T_s is not constant. It varies in response to the total heat load and depends on performance of the heat exchanger, which condenses the fluid and facilitates return of condensate. While many different types of heat exchanger exist, they share some common features. The condenser side comprises a large surface area exposed to the saturated fluid's vapour. The flow side consists of channels/ducts which direct forced flows of liquid or air. The inlet temperature at

Table 2.2: Thermal performance and system properties of single and two phase cooling techniques.

Cooling method	**Switch-level heat transfer coefficient,** $\mathrm{W/(cm^2\,K)}$	**Switch-level Critical heat flux,** $\mathrm{W/cm^2}$	**Electrical isolation?**	**Additional system components**
Dielectric fluid boiling on smooth surface [24]	1.9	21	Yes	Heat exchanger
Dielectric fluid boiling on porous surface [39]	3.0	80	Yes	Heat exchanger
Dielectric fluid boiling with heat spreader [42]	25.0	1180	Yes	Heat exchanger
Silicon micro-channels with water [44]	11.0	N/A	No	Heat exchanger, pump
Aluminium micro-channel with water jets [44]	6.9	N/A	No	Heat exchanger, pump, manifold
Finned copper heat spreader with dielectric fluid jets	5.3	N/A	Yes	Heat exchanger, pump, manifold

the flow side is represented by T_{fl}. The heat exchanger is an important consideration as it contributes significantly to both the temperature of immersed electronic components and overall system volume.

For power dense converter applications, it is useful to consider thermal performance normalised to the converter volume. A useful metric is the cooling system performance index (CSPI) defined in Equation 2.6 [49]. It is expressed in terms of the total converter power dissipation Q_{conv} and its volume ν_{conv}. T_{j} is a measure of the average temperature internal to immersed components, for example at the

semiconductor junction of a switch.

$$\text{CSPI} = \frac{Q_{\text{conv}}}{\nu_{\text{conv}}(T_{\text{j}} - T_{\text{fl}})} \tag{2.6}$$

This metric is complicated by difficulty in defining the converter volume ν_{conv} and the temperature T_{j}. A related quantity, the heat exchanger performance index (HEPI) is defined by Equation. 2.7 in terms of the heat exchanger volume ν_{hex} and the fluid saturation temperature T_s. This metric depends purely on properties of the heat exchanger and provides an upper limit on the achievable value of CSPI.

$$\text{HEPI} = \frac{Q_{\text{conv}}}{\nu_{\text{hex}}(T_{\text{s}} - T_{\text{fl}})} \tag{2.7}$$

2.3.1 Heat Exchanger Performance

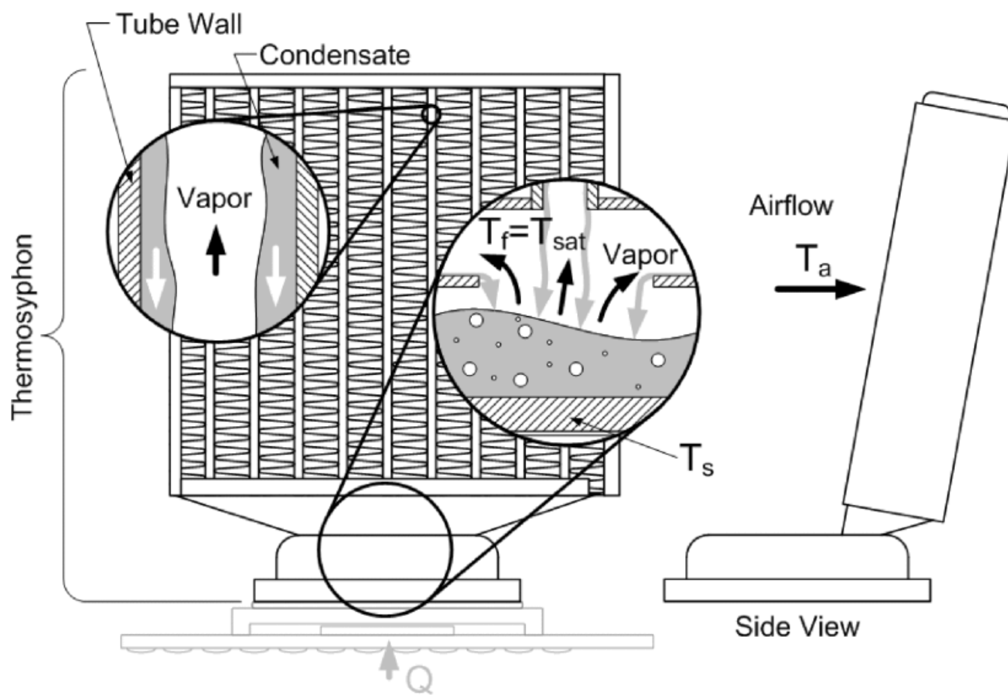

Figure 2.12: Diagram of air cooled fin and tube heat exchanger for two-phase immersion systems. Reproduced from [50] ©2007 IEEE.

Fin and tube heat exchangers, an example of which is depicted in Fig. 2.12, are frequently employed in two-phase immersion cooling systems. The vapour condenses along inner surfaces of the tubes while air is blown through the fins. Several studies have characterised thermal resistance for heat exchangers with varying fin/tube

arrangements [50] [51] [52]. The best performing heat exchanger exhibits thermal resistance of 0.042 °C/W using Novec 7000 fluid with an airflow of 2.2 m^3/min [52]. The heat exchanger volume is 0.6 L yielding HEPI of 40 W/(L K).

Heat exchangers with liquid on the flow side demonstrate substantial improvement over those cooled by air. Parallel plate heat exchangers comprise arrays of metal plates which separate the two-phase working fluid from the flow side liquid. A commercial stainless steel parallel plate heat exchanger with water on the flow side and refrigerant R245fa on the condenser side demonstrates HEPI of 300 W/(L K) [53]. In [54], it is proposed to use refrigerant R134a as both the two-phase working fluid and the flow side medium. The refrigerant boils in contact with the flow side surface and undergoes a pumped refrigeration cycle, rejecting heat to ambient air. The custom condensation-to-boiling heat exchanger exhibits HEPI of 260 W/(L K).

2.3.2 Overall System Performance

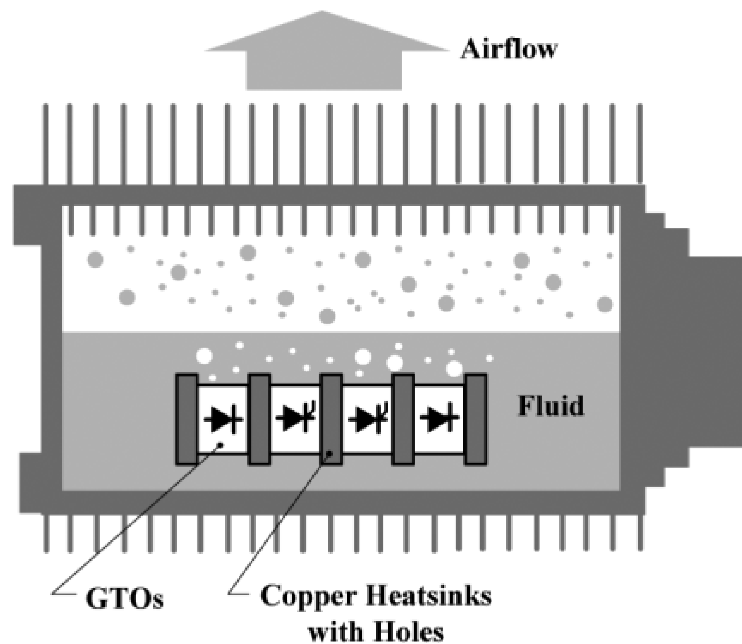

Figure 2.13: Diagram of an immersion cooled traction inverter using gate turn on (GTO) thyristor switches. Reproduced from [42] ©2010 IEEE.

Several practical two-phase immersion cooling systems have been proposed in literature, for which CSPI values can be estimated. Early implementations were

developed to cool semiconductor switches for traction inverters in trains [55] and haulage trucks [56]. The switches are pressed together with heat spreaders attached on both sides and submerged in a tank of dielectric fluid as shown in Fig. 2.13. The vapour condenses in contact with the internal tank walls while the external surface is cooled by air. The stated converter electrical power density of 1 kW/L and efficiency of 96 % [56] can be used to estimate power dissipation of 40 W/L. Assuming a moderate temperature rise from flow side to switch of 10 °C, it is clear these systems fail to achieve CSPI above 5 W/(L K).

Another two-phase immersion cooling approach proposed in literature immerses semiconductor switches, possibly with heat spreaders attached, in a sealed enclosure coupled to a separate commercial air-cooled heat exchanger. To the author's knowledge, the best performing system exhibits CSPI of 17 W/(L K). This was achieved by utilising highly effective double-sided cooling [42] in Novec 7000 dielectric fluid and the best performing heat exchanger from [52]. In [53], a two-phase system using refrigerant R245a and a water cooled parallel plate heat exchanger was proposed to cool four Infineon Econopack+ power modules. Taking into account volume of the heat exchanger and power modules, the CSPI value achieved is 45 W/(L K)

A novel approach detailed in [57] integrates the heat exchanger into the fluid chamber as illustrated by Fig. 2.14. It is conceptually similar to the system proposed in Fig.1.3. The condenser side comprises downward facing pin fins along which condensate forms before dripping back into the fluid pool. The flow side features parallel channels through which a water-glycol coolant is passed. Despite the use of liquid cooling on the flow side, the proposed system achieves a CSPI of only 5 W K/L with Novec 649 dielectric fluid.

2.4 Two-phase Immersion Cooling for Magnetic Components

There are comparatively few works in prior literature applying two-phase immersion cooling for power inductors and transformers. Experiments have been conducted

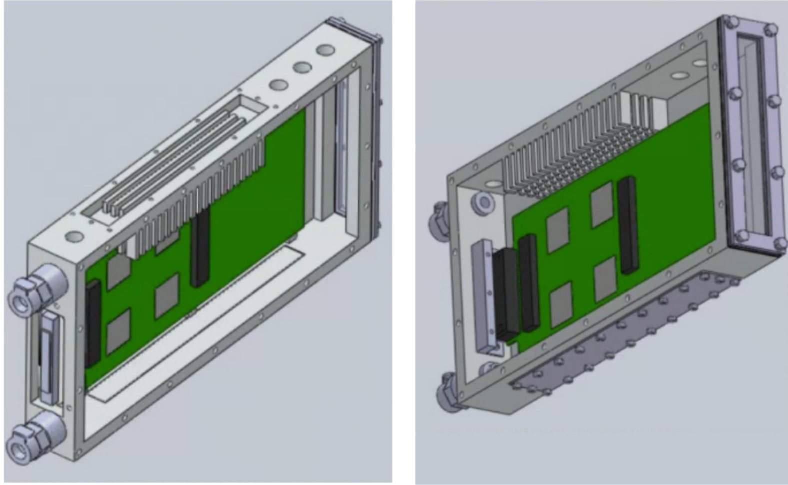

Figure 2.14: Renders of two-phase immersion cooled system with liquid-cooled heat exchanger integrated into the chamber. Reproduced from [57] ©2015 IEEE.

with magnetic components configured as filter inductors and DC-DC converter transformers immersed in dielectric fluid for thousands of hours [58]. No noticeable difference in appearance or mass was reported, indicating chemical compatibility of the fluid with common materials used in magnetic components such as enamelled copper wires and ferrite cores.

In high voltage power transmission transformers, two-phase immersion cooling with dielectric fluids has been explored as a non-flammable alternative to mineral oil [59]. In certain applications like mine tunnels, air-cooled transformers are typically used as the mineral oil flammability risk cannot be tolerated. By using fluorocarbon fluid instead, corrugated fins used to increase heat transfer to ambient air can be removed, decreasing the transformer tank volume by 50 % [60].

3

Boiling Heat Transfer for Planar Semiconductor Switches

Studies presented in the literature with dielectric fluids boiling on smooth, flat surfaces at atmospheric pressure demonstrate heat transfer coefficients up to $1\,\mathrm{W/(cm^2\,K)}$ and critical heat fluxes up to $30\,\mathrm{W/cm^2}$. Table 3.1 summarises physical properties for several fluorocarbon and Novec dielectric fluids. All exhibit atmospheric pressure boiling points between 30 °C and 56 °C. In electric vehicle power electronics, the lowest system temperature is determined by the water glycol coolant loop to which the converter rejects heat. The Advanced Propulsion Centre UK roadmap specifies a minimum coolant loop temperature of 65 °C [5]. Consequently, when applying two-phase immersion cooling, the dielectric fluid boils at a saturation pressure higher than atmosphere.

Experiments with water and organic solvents boiling at elevated pressures demonstrate improvements in both heat transfer coefficient and critical heat flux with increasing pressure [21]. This effect is explained by the reduction in liquid surface tension and increase in vapour density with saturation pressure and temperature. It is experimentally observed this leads to smaller bubble diameters in deionized water [61], which favourably influences boiling heat transfer. Furthermore, higher densities of active nucleation sites are observed in water at higher pressures [62]

which accounts for a proportional increase in the boiling heat transfer coefficient.

The purpose of this chapter is to characterise the boiling heat transfer coefficient and critical heat flux at elevated saturation pressures and temperatures for flat, planar surfaces representative of semiconductor switches. A temperature range of 65 °C to 100 °C was selected, representing the condition in an electric vehicle motor drive. Existing nucleate boiling and critical heat flux models with temperature dependent physical properties are employed to predict performance of each candidate fluid. An experimental apparatus is detailed which incorporates a realistic heat exchanger design and a water cooling loop at 65 °C. It is used to validate theoretical predictions for Novec 7000 dielectric fluid. The experimental results provide practical limits for flat semiconductor switches in a two-phase immersion cooled converter.

3.1 Fluid Thermophysical Properties

For the dielectric fluids in Table 3.1, liquid thermal conductivity, specific heat capacity, dynamic viscosity, liquid density and saturation pressure can be evaluated at different temperatures using expressions provided by the manufacturer. Additional models for the temperature dependence of liquid surface tension, vapour density and latent heat are required in order to predict the boiling heat transfer coefficient and critical heat flux.

3.1.1 Surface Tension

Liquid surface tension can be modelled using the Eötvös rule in Equation. 3.1 [66]. It predicts a linear decrease of surface tension with temperature until zero at the critical point. The Eötvös constant k_E is evaluated from the surface tension at 25 °C provided in the data sheet.

$$\sigma_\mathrm{l} = k_\mathrm{E}(T_\mathrm{crit} - T_\mathrm{s})\frac{M}{\rho_\mathrm{l}}^{-\frac{2}{3}} \tag{3.1}$$

Table 3.1: Thermophysical properties for candidate dielectric fluids. Liquid properties are at 25 °C while phase change properties are at atmospheric pressure.

	FC72 [16]	**FC87** [63]	**FC3284** [64]	**Novec 649** [65]	**Novec 7000** [17]
Molar mass M (kg/mol)	0.338	0.288	0.299	0.316	0.200
Liquid thermal conductivity k_l (W/(m K))	0.057	0.056	0.062	0.059	0.075
Specific heat c_p (kJ/(kg K))	1.1	1.1	1.1	1.1	1.3
Liquid density ρ_l (kg/m^3)	1680	1650	1710	1600	1400
Liquid dynamic viscosity μ_l (mPa s)	0.64	0.45	0.71	0.64	0.45
Liquid surface tension σ_l (mN/m)	10.0	9.0	13.0	10.8	12.4
Latent heat at 1 atm l_lv (kJ/kg)	88	103	105	88	142
Boiling point at 1 atm (°C)	56	30	50	49	34
Saturation pressure P_s (kPa)	30.9	81.1	35.7	40.0	65.0
Critical pressure P_crit (kPa)	1830	2130	1940	1880	2480
Critical temperature T_crit (°C)	176	150	161	169	165

3.1.2 Vapour Density

For saturation pressures significantly lower than the critical pressure, the vapour phase can be modelled as an ideal gas with density predicted by Equation 3.2.

$$\rho_\mathrm{v} = \frac{MP_\mathrm{s}}{RT_\mathrm{s}} \tag{3.2}$$

To validate this assumption, vapour densities are also calculated numerically using the cubic Redlich-Kwong equation. Fig. 3.1 compares the values predicted by the ideal gas model with the Redlich-Kwong equation for all fluids across the temperature range of interest. The largest deviation between the two models is

Table 3.2: Comparison of data-sheet values for latent heat at atmospheric pressure boiling point with calculations via Equation. 3.3.

	FC72	**FC87**	**FC3284**	**Novec 649**	**Novec 7000**
Latent heat l_{lv} (kJ/kg)	88	103	105	88	142
Estimated latent heat (kJ/kg)	87.8	102.2	104.5	92.6	146.8
Percentage error (%)	0.23	0.78	0.48	4.84	3.38

25 % for FC87 at 100 °C. The remaining fluids deviate by between 12 % and 18 % at 100 °C. The ideal gas model is deemed sufficiently accurate to provide estimates of boiling heat transfer performance.

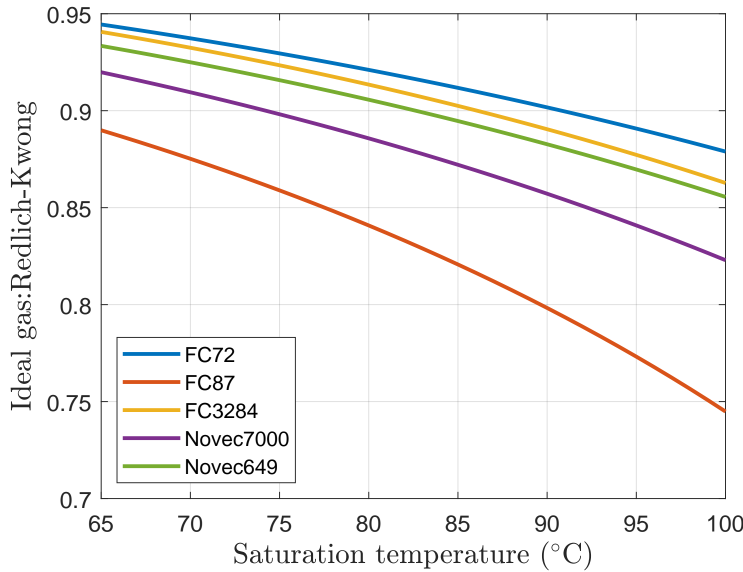

Figure 3.1: Ratio of vapour densities calculated by ideal gas equation and Redlich-Kwong equation.

3.1.3 Latent Heat

The Clapeyron equation below provides an expression for the gradient of saturation pressure with respect to temperature [14]. Since the relationship between saturation pressure and temperature is provided for all fluids, $\frac{dP_{\mathrm{s}}}{dT_{\mathrm{s}}}$ is known and Equation 3.3

can be rearranged to calculate latent heat.

$$\frac{\mathrm{d}P_\mathrm{s}}{\mathrm{d}T_\mathrm{s}} = \frac{l_\mathrm{lv}}{T_\mathrm{s}\left(\frac{1}{\rho_\mathrm{v}} - \frac{1}{\rho_\mathrm{l}}\right)} \tag{3.3}$$

Table. 3.2 compares calculated latent heats with data-sheet values at 25 °C for all fluids. The percentage difference is less than 5 % in each case.

3.2 Pool Boiling Models

3.2.1 Nucleate Boiling

Due to the complexity of underlying physical phenomena, nucleate boiling is usually modelled by empirical relationships derived from experimental data. In general, the boiling heat transfer coefficient of Equation 2.1 is expressed as a non-linear function of the difference between the surface temperature T_c and the fluid saturation temperature T_s

The Rohsenow correlation postulates heat transfer occurs predominantly from surface to liquid, which is agitated in the wake of departing bubbles [67]. A forced convection formulation is proposed which yields Equation 3.4 for the heat transfer coefficient. The Prandtl number exponent m is 1.7 and parameter C_sf is fit to experimental data to account for the specific combination of fluid and surface. Exponent n is 0.33 so the model predicts an approximately square dependence of the boiling heat transfer on the surface temperature rise.

$$h = \mu_\mathrm{l} l_\mathrm{lv} \frac{(T_\mathrm{c} - T_\mathrm{s})^{\frac{1-n}{n}}}{\left(\frac{C_\mathrm{sf} l_\mathrm{lv}}{c_\mathrm{p}} \mathrm{Pr}^m\right)^{\frac{1}{n}}} \left(\frac{\sigma_\mathrm{l}}{g(\rho_\mathrm{l} - \rho_v)}\right)^{-\frac{1}{2}} \tag{3.4}$$

The Stephen-Abdelsalam model was derived as a relationship between dimensionless groups by fitting to a large dataset. Different correlations are proposed for each of four general classes of fluids. The correlation for hydrocarbons is expressed in Equation 3.5 [68].

$$h = \left(0.0546 \frac{k_\mathrm{l}}{d_0} \left(\left(\frac{\rho_\mathrm{v}}{\rho_\mathrm{l}}\right)^{0.5} \frac{d_0}{k_\mathrm{l} T_\mathrm{s}}\right)^{0.67} \left(\frac{\rho_\mathrm{l} c_\mathrm{p} l_\mathrm{lv} d_0^2}{k_\mathrm{l}}\right)^{0.248} \left(\frac{\rho_\mathrm{l} - \rho_\mathrm{v}}{\rho_\mathrm{l}}\right)^{-0.433}\right)^3 (T_\mathrm{c} - T_\mathrm{s})^2 \tag{3.5}$$

The Stephen-Abdelsalam incorporates a direct dependence of heat transfer coefficient on the bubble departure diameter d_0, defined by Equation 3.6. As the saturation pressure increases, Equation 3.5 predicts an increase in heat transfer coefficient due to the corresponding decrease in bubble diameter.

$$d_0 = 0.723\left(\frac{\sigma_{\mathrm{l}}}{g(\rho_{\mathrm{l}} - \rho_{\mathrm{v}})}\right)^{0.5} \tag{3.6}$$

Reduced pressure models are based on the observation that all substances exhibit similar behaviour when normalised to the critical point properties. Nucleate pool boiling correlations can be expressed only in terms of the reduced pressure P_{r}, which is normalised to the critical pressure. One example is Mostinski's correlation in Equation 3.7 [69]. The reduced pressure formulation directly predicts an increase in heat transfer coefficient with saturation pressure.

$$h = (0.00417P_{\mathrm{crit}}^{0.69}(1.8P_{\mathrm{r}}^{0.17} + 4P_{\mathrm{r}}^{1.2} + 10P_{r}^{10}))^{3.3}(T_{\mathrm{c}} - T_{\mathrm{s}})^{2.3} \tag{3.7}$$

The Cooper correlation is another reduced pressure model which a accounts for surface properties via the roughness r_{p} [14].

$$h = (55P_{\mathrm{r}}^{0.12-0.4343\ln r_{\mathrm{p}}}(-\log_{10} P_{\mathrm{r}})^{-0.55}M^{-0.5})^{3}(T_{\mathrm{c}} - T_{\mathrm{s}})^{2} \tag{3.8}$$

A study across several different fluids and surfaces [70] compares the accuracy of Rohsenow's correlation with fitted parameters and several generalised correlations depending only on physical properties. Rohsenow's correlation was found to agree with experiments to within 40 % while the other models deviated by up to 300 %. In the absence of experimental data, the Stephen-Abdelsalam correlation is used to predict the boiling heat transfer coefficient, shown in Fig. 3.2. The surface temperature is set 25 °C higher than the saturation temperature. There is a significant increase in heat transfer coefficient with saturation temperature for all fluids across the entire range considered; this is attributed to the increase in vapour density and decrease in the bubble departure diameter. FC87 was identified as the best performing fluid across the entire temperature range. This is explained by its high vapour pressure which yields highest vapour densities.

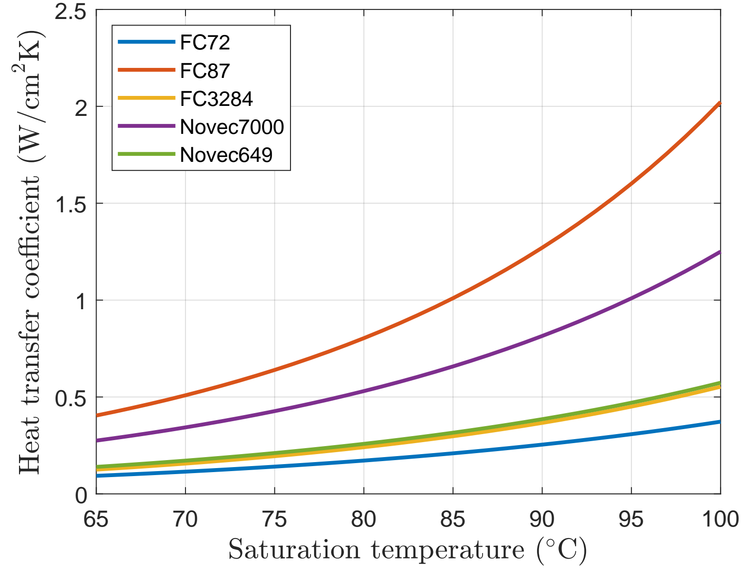

Figure 3.2: Heat transfer coefficient as a function of fluid saturation temperature.

3.2.2 Critical Heat Flux

The most widely accepted explanation of critical heat flux is the incipience of hydrodynamic instability in close proximity to the switch surface. Once this occurs, mechanisms which transport vapour away from the surface become insufficient to contend with the rate of vapour generation rate and bubbles start to crowd the surface. An analytical model for this phenomenon was proposed by Zuber [71], yielding an estimate of critical heat flux on infinite flat surfaces denoted by q_{zub}.

$$q_{\mathrm{zub}} = \frac{\pi}{24}\rho_{\mathrm{v}}^{\frac{1}{2}} l_{\mathrm{lv}} (g(\rho_{\mathrm{l}} - \rho_{\mathrm{v}})\sigma)^{\frac{1}{4}} \tag{3.9}$$

Based on experiments characterising critical heat flux for objects with varying shape, it is suggested the effect can be accurately modelled by applying geometry-dependent corrective factors to Equation 3.9 [72]. For large flat surfaces as considered in this chapter, the following correction is applied to calculate the critical heat flux q_{chf}.

$$q_{\mathrm{chf}} = 1.14 q_{\mathrm{zub}} \tag{3.10}$$

Previous studies [21] have reported an increase in critical heat flux with fluid saturation temperature. However, both the liquid surface tension and latent heat tend to zero as the saturation temperature approaches the critical point.

Equation 3.10 thus predicts an eventual decrease in CHF, reaching zero at the critical temperature. This is not observed for any fluid within the range of saturation temperatures considered in this work as shown in Fig. 3.3. The critical heat flux increases consistently with temperature and is highest for Novec 7000 due to the high latent heat.

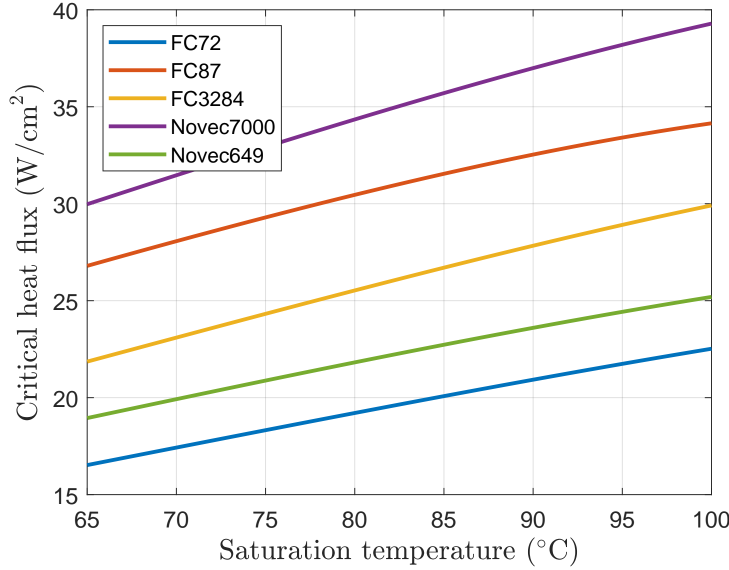

Figure 3.3: Critical heat flux as a function of fluid saturation temperature.

3.3 Experimental Verification

Novec 7000 and FC87 were identified as the most promising dielectric fluids. Despite the lower heat transfer coefficients, Novec 7000 was selected for further investigation. In addition to the larger critical heat flux, it also exhibits lower vapour pressures and a higher critical temperature, both of which are desirable in a practical system. An experimental approach was developed to characterise heat transfer from the surface of semiconductor switches immersed in Novec 7000. The switch is represented by a facsimile machined in metal. Using this approach, the heat flow can be set using simple resistive heating elements and a thermocouple inserted close below the facsimile surface can provide approximate measurements of the corresponding switch surface temperature T_c. As illustrated in Fig. 3.4, each facsimile has the

same planar area exposed to fluid as the switch. All surrounding material which facilitates heat flow is insulated from the fluid.

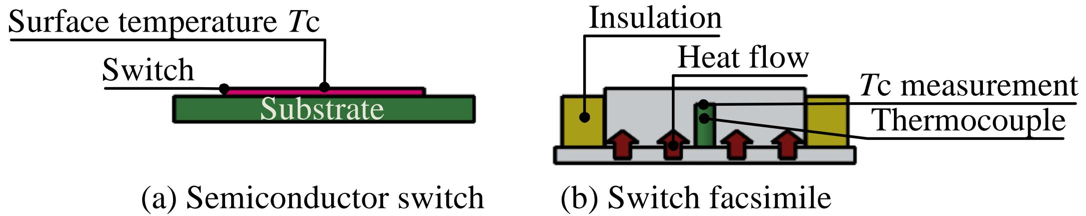

Figure 3.4: Diagram showing correspondence between a planar semiconductor switch and its facsimile.

3.3.1 Test Apparatus

The experimental apparatus consists of an open-ended cylindrical borosilicate chamber which encloses the fluid by sealing between a heater block and heat exchanger via an arrangement of nitrile O-rings shown in Fig. 3.5. The chamber wall thickness was chosen as 3.5 mm. Calculations indicate this is sufficient to withstand absolute pressures of 2000 kPa; the vapour pressure of Novec 7000 at 100 °C is significantly lower at 700 kPa.

The heater block is machined in aluminium 6082 with six 12.6 mm x 5.6 mm protrusions, each designed as a facsimile for one 150 A, 650 V GS-065-150-1-D2 bare die switch from GaN systems [73] in three-phase inverter configuration. Four cartridge heaters insert into the underside of the block to set the power dissipation through the switch facsimiles. K-type thermocouples insert to a depth of 1 mm beneath each switch facsimile to provide measurements of the surface temperature. A polyetheretherketone (PEEK) part fits tightly around the facsimiles to inhibit heat transfer from the heater block bulk into the fluid. It also provides a groove to house an O-ring seal around the borosilicate chamber. The heater block sides and bottom are insulated with PEEK to minimise heat loss to ambient air.

The heat exchanger is a custom circular aluminium 6082 part designed to fit the borosilicate chamber dimensions. The condenser side features a 45 mm surface exposed to the vapour, enhanced with pin fins; design of the fin arrangement is

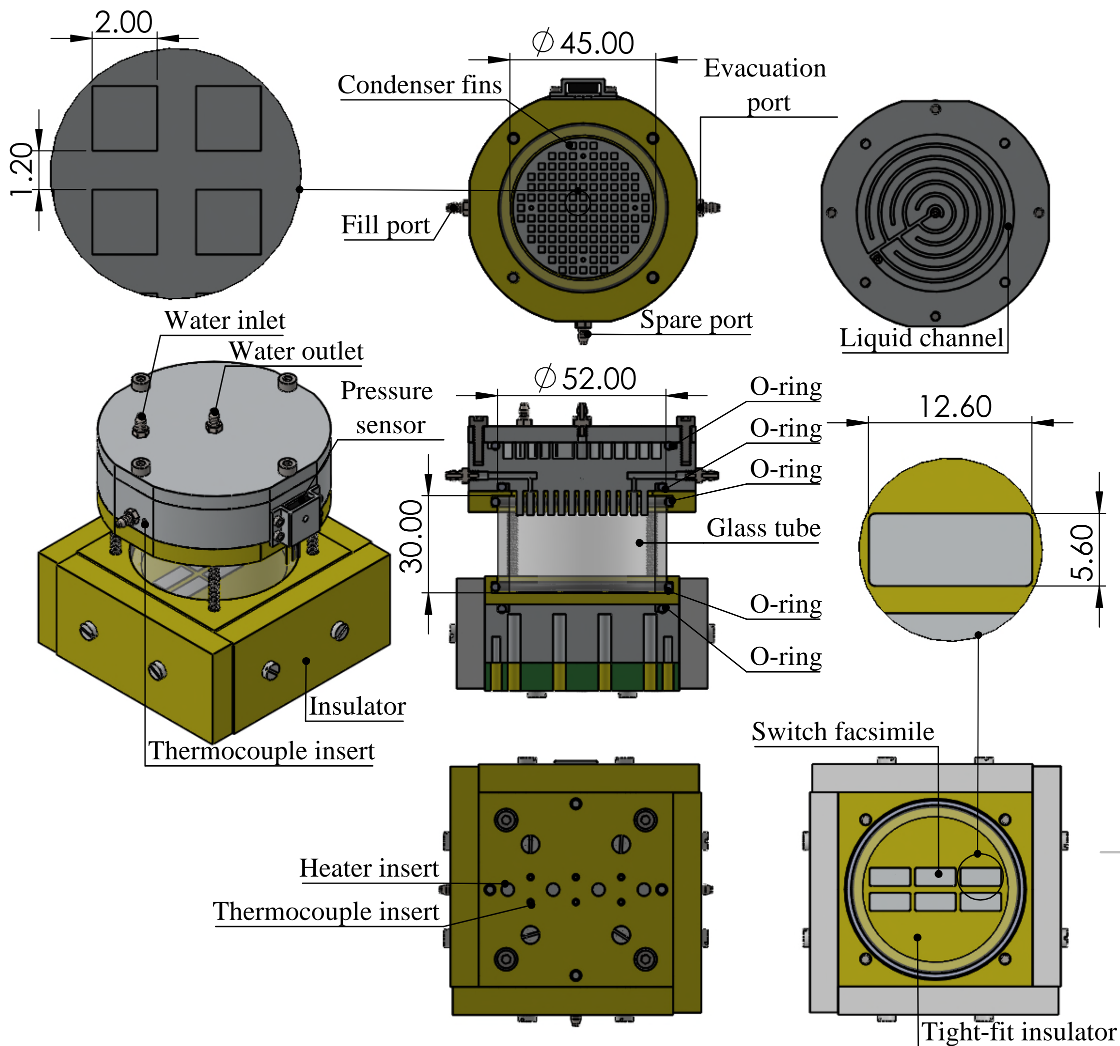

Figure 3.5: Section views of experimental apparatus. All dimensions are in millimetres.

discussed in more detail in Chapter 5. A Polyscience AP15R-40-A11B refrigerated circulator pumps water through the flow side channels at temperature set point of 65 °C. Two thermocouples embedded in the heat exchanger measure the temperature close to the condenser fin base. A polytetrafluoroethylene (PTFE) part supports a second O-ring seal around the borosilicate chamber top.

A Bourns BPS130 absolute pressure sensor is mounted on a port in the heat exchanger and sealed with a nitrile O-ring. This provides measurements of the saturation pressure which can be used to estimate the bulk temperature of the fluid, provided the system is saturated and free of air. A simple evacuation and filling procedure is followed to purge air from the apparatus: The chamber is

completely filled with fluid, after which the fill port is closed off with a clip. Heat is applied and liquid boiled off to atmosphere through the evacuation port until the desired fill height is reached. The evacuation port is then closed, leaving a completely sealed system saturated with working fluid. Pressure was continuously monitored over the course of several days following the fill procedure. As the system cooled, the measured pressure approached the room-temperature vapour pressure of Novec 7000. There was negligible further increase in pressure, indicating minimal leakage of air into the system.

3.3.2 Data Collection

Experiments were performed by incrementally increasing the heat flux through the switch facsimiles by stepping the voltage applied to the cartridge heaters by a EA-PS2084-05B power supply. After each increment, the system is allowed to reach steady state. This condition is identified by averaging 50 sequential temperature measurements for each thermocouple. Once the difference between two subsequent averages for all thermocouples falls below 0.1 °C, steady state is determined and ten further sequential measurements of each quantity are recorded and averaged. The steady state temperature measurement for each of the six switch facsimiles is used to calculate the average facsimile temperature T_c.

The heat exchanger features 6 mm thickness of aluminium between the condenser side and the liquid cooled side to support measurement ports and fittings. Two thermocouples are embedded in this layer and the measurements are averaged to calculate the condenser fin base temperature T_b. This layer is also intended to spread heat laterally and provide a near-isothermal condition at the thermocouple height regardless of any temperature rise of the water as it flows from inlet to outlet. The saturation temperature of the fluid T_s is determined from the measured pressure by inverting Equation 3.11 which is provided in the data sheet [17].

$$P_\mathrm{s} = \exp\left(\frac{-3548.6}{T_\mathrm{s} + 273.15} + 22.978\right) \tag{3.11}$$

The power at each step is calculated by multiplying the voltage and current from the power supply for each cartridge heater. A correction is made to account

for power dissipated in the cartridge heater leads. The power is also compensated to account for heat losses from the insulated surfaces of the heater block to ambient air. A test was conducted with the heater block detached from the chamber/heat exchanger and the switch facsimiles covered by insulating wool. All power applied by the cartridge heaters in this test was lost to ambient air through the PEEK insulation. A linear relationship plotted in Fig. 3.6 is derived between the heat loss and the average facsimile temperature increase above the ambient air temperature T_a. Assuming the temperature does not vary appreciably across the heater block, this relationship can be used in all tests to calculate the heat loss through the insulation.

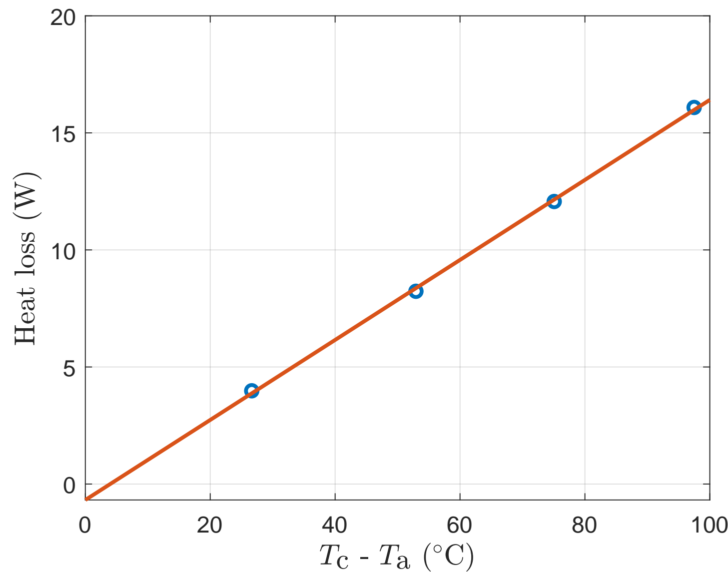

Figure 3.6: Heat loss to ambient air through heater block insulation as a function of the facsimile temperature increase above ambient.

Sources of uncertainty associated with the experimental equipment are summarised in Table 3.3. Standard error propagation techniques are used to evaluate percentage uncertainties for all derived values and these are displayed as error bars on subsequent figures. More detail concerning the error propagation method is provided in Appendix A. The maximum percentage error for the heat transfer coefficient is 23.1 %. This occurs at the smallest value of the temperature difference $T_c - T_s$ due to the relatively large uncertainty associated with the thermocouple.

Table 3.3: Summary of sources of experimental uncertainty.

Quantity	**Measurement approach**	**Uncertainty**
Switch facsimile temperatures	Thermocouple	±1.5 °C
Cartridge heater voltage	Desk power supply	±0.2 %
Cartridge heater current	Desk power supply	±0.3 %
Saturation pressure	Absolute pressure sensor	±1 % full scale
Switch facsimile length	Machining tolerance	±0.2 mm
Switch facsimile width	Machining tolerance	±0.2 mm
Average switch facsimile temperature T_c	Calculation	± (1.2 %-2.0 %)
Saturation temperature T_s	Equation 3.11	± (0.5 %-1.2 %)
$T_c - T_s$	Calculation	± (4.8 %-23.1 %)
Power	Calculation	± (2.0 %-3.1 %)
Heat flux	Calculation	± (4.7 %-5.5 %)
Heat transfer coefficient	Calculation	± (5.1 % - 23.1 %)

As both power and the temperature difference increase, the heat transfer coefficient becomes less sensitive to thermocouple uncertainty and the percentage error drops as low as 5.1 %.

3.3.3 Experimental Results

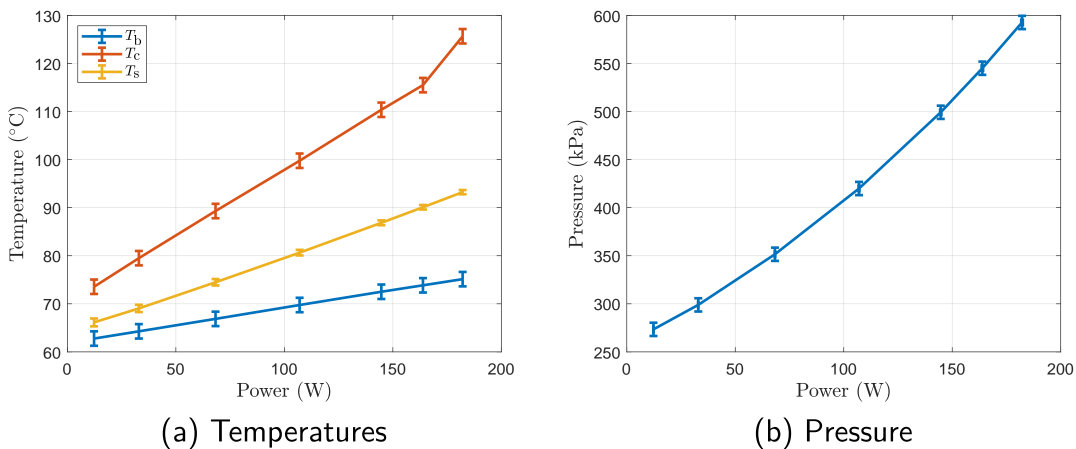

Figure 3.7: (a) Measured temperatures T_c, T_s and T_b and (b) saturation pressure P_s at different power dissipations.

Fig. 3.7 shows the average facsimile temperatures T_c, fluid saturation temperature T_s and condenser base temperature T_b, as well as saturation pressure P_s as a function of the compensated total power. The apparatus was tested up to 182 W at which point the experiment was halted due to observation of critical heat flux. The maximum observed fluid saturation temperature is 93 °C; this corresponds to a maximum saturation pressure of 593 kPa.

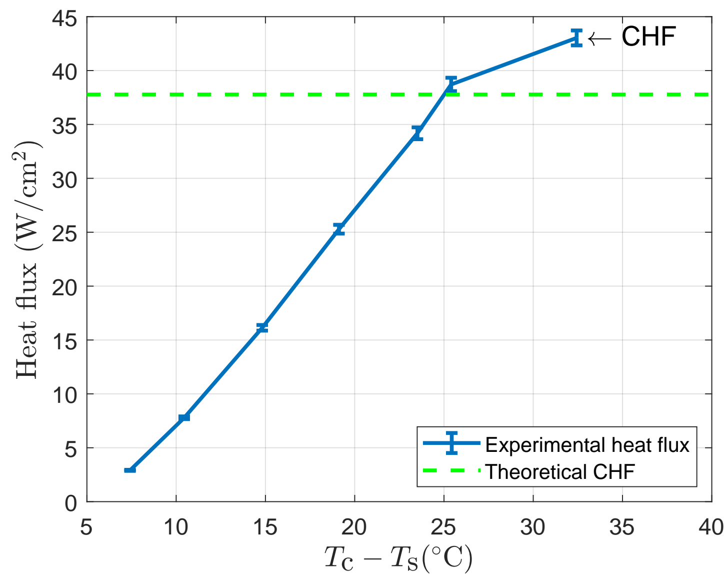

Figure 3.8: Heat flux dependence on difference between average facsimile temperature T_c and fluid saturation temperature T_s.

Fig. 3.8 demonstrates the variation of heat flux with temperature difference between the facsimile surface and the fluid. Critical heat flux was observed at 43 W/cm^2 by a sudden increase in the average switch facsimile temperature and a corresponding decrease in the saturation pressure. For comparison, the value calculated by Equation 3.10 is 37.7 W/cm^2. To validate the predicted trend of increasing critical heat flux with fluid saturation temperature, two further experiments were conducted with the flow side water temperature at 35 °C and 50 °C. In these tests, CHF was observed at saturation temperature of 66 °C and 81 °C respectively; the three experimental CHF values are shown in Fig. 3.9. The model under-predicts the measurements by only 6 % to 13 %. The discrepancy can be explained in part by under-prediction of the vapour density using the ideal gas

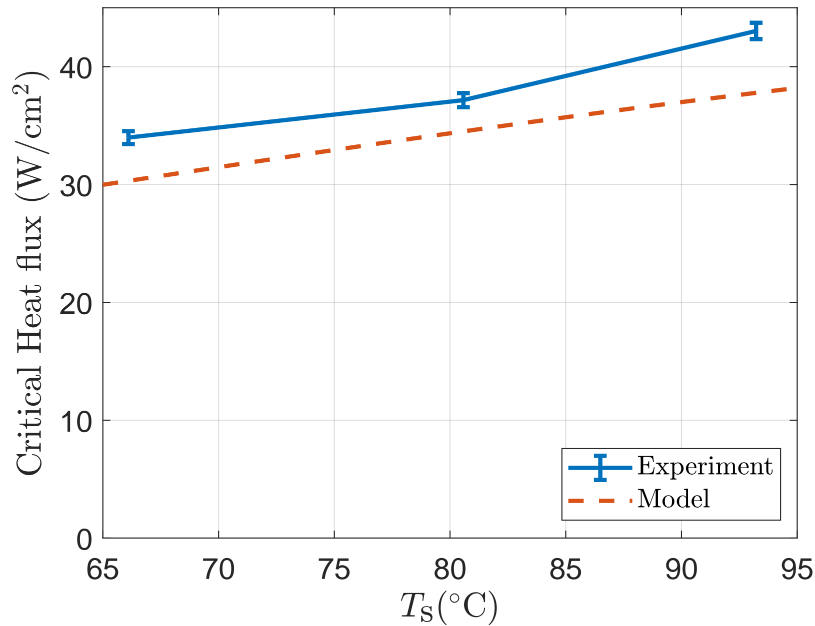

Figure 3.9: Experimental and theoretical critical heat fluxes at different fluid saturation temperature.

model.

The heat transfer coefficient defined by Equation 2.1 is derived from experimental data for 65 °C flow side water and plotted in Fig. 3.10 as a function of the facsimile temperature rise above the fluid saturation temperature. The highest value is 1.5 W/(cm^2 K), notably higher than results reported with Novec 7000 boiling at atmosphere, due to the elevated saturation temperature and pressure. Corresponding theoretical values are also calculated using the four boiling correlations detailed in Section 3.2. The Mostinski and Stephen-Abdelsalam models significantly under-predict the heat transfer coefficient across the majority of data points. Cooper's correlation was evaluated with surface roughness of 1 µm (recommended for unknown surfaces). Improved agreement is observed for temperature rises up to 15 °C. However, beyond this point as the heat flux approaches its critical value, the model drastically departs from the experimental data. In fact, all three correlations predict rapid growth of the heat transfer coefficient with increasing temperature rise. From the data, it is observed this trend does not persist up until the critical heat flux. Instead the increase of heat transfer coefficient diminishes and even becomes

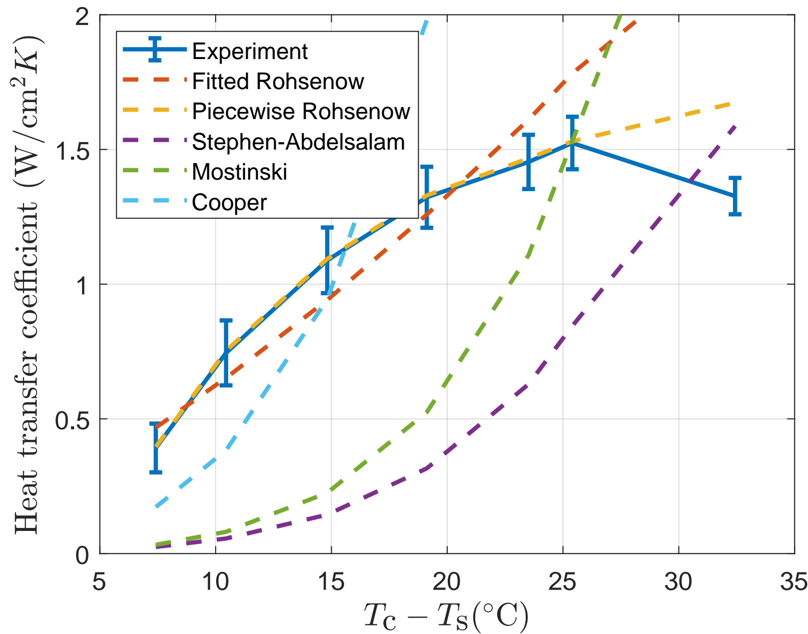

Figure 3.10: Experimental and theoretical heat transfer coefficients.

negative just before critical heat flux. Similar behaviour has been demonstrated in literature for experiments with Novec 7100 and Novec 649 [25]. It is attributed to bubble coalescence at higher heat fluxes leading to formation of larger bubbles and eventually vapour jets as critical heat flux is approached [33].

Also shown in Fig. 3.10 are predictions derived using a least-squares fit for the Rohsenow correlation, which yielded parameters $C_{sf} = 0.0042$ and $n = 0.5351$. The fitted correlation agrees with experiment to a mean percentage error of 13 %. Several works in the literature have proposed that a single power law correlation is insufficient to accurately reproduce the entire pool boiling curve up to the critical heat flux [22] [74]. It is advocated instead to subdivide the curve into segments, each modelled by a separate power law. The Rohsenow correlation was used with parameter C_{sf} and exponent n chosen to fit each segment of the data. Table 3.4 presents the values obtained and the temperature ranges over which they are valid. The exponent n for temperature rises below 10.4 °C is 0.3695, close to the value of 0.33 recommended by Rohsenow [67].

Table 3.4: Parameters used to evaluate the Rohsenow correlation for different portions of the pool boiling curve.

Quantity	$C_{\mathbf{sf}}$	n
$T_c - T_s \leq 10.4$	0.0042	0.3695
$10.4 < T_c - T_s \leq 14.8$	0.0039	0.5262
$14.8 < T_c - T_s \leq 19.1$	0.0034	0.6432
$19.1 < T_c - T_s$	0.0027	0.7798

3.4 Conclusions

Based on the work presented in this chapter, several conclusions have been drawn surrounding the boiling heat transfer on flat smooth surfaces representative of switches in immersion cooled inverters.

- The boiling heat transfer coefficient and critical heat flux increase with saturation temperature due to the increase in vapour density and decrease in bubble diameter. This is demonstrated by applying temperature dependence of thermophysical properties to existing models and validated through experiment.

- In a practical two-phase immersion cooled inverter for electric vehicle applications, it is reasonable to expect to dissipate up to $43\,\mathrm{W/cm^2}$ from planar semiconductor switches. This result agrees to within 13 % with models of critical heat flux based on hydrodynamic instability mechanisms.

- The highest heat transfer coefficient observed is $1.5\,\mathrm{W/(cm^2\,K)}$. Experimental measurements deviate from the trends predicted by nucleate pool boiling models at higher heat fluxes.

4

Boiling Heat Transfer for Finned Heat Spreaders

In the previous chapter, experiments with Novec 7000 boiling on a flat planar surface indicate a maximum heat transfer coefficient of $1.5\,\mathrm{W/(cm^2\,K)}$ and a critical heat flux of $43\,\mathrm{W/cm^2}$. In prior literature, both heat spreaders and surface enhancement techniques have been employed to maximise the allowable power dissipation per unit area of semiconductor switch. Effective heat transfer coefficients up to $25\,\mathrm{W/(cm^2\,K)}$ and critical heat fluxes up to $1110\,\mathrm{W/cm^2}$ have been demonstrated [42]. However, such high performance necessitates use of heat spreaders with planar area several times larger than the semiconductor switch. This approach may not be suitable for PCB-based converters where it is desired to minimise distance between all of the semiconductor switches and their ancillary components.

This chapter investigates the achievable improvements in boiling heat transfer using heat spreaders which comply with practical geometrical constraints for PCB-based converters. The proposed heat spreader has the same planar area as a GS-065-150-1-D2 semiconductor switch from GaN systems and uses normally protruding fins to increase the heat transfer area. A theoretical model for square pin fins immersed in boiling fluid is developed, incorporating non-linear dependence of the heat transfer coefficient on temperature. While analytical solutions to this

problem exist in special cases, a numerical solution procedure is adopted and explained in this chapter. Effective heat transfer coefficients and critical heat fluxes are predicted for several designs of finned heat spreader immersed in Novec 7000. These predictions are validated experimentally for the best heat spreader design. Finally, grit blasting is applied to characterise potential further improvements offered by simple surface enhancements.

4.1 Boiling Fin Model

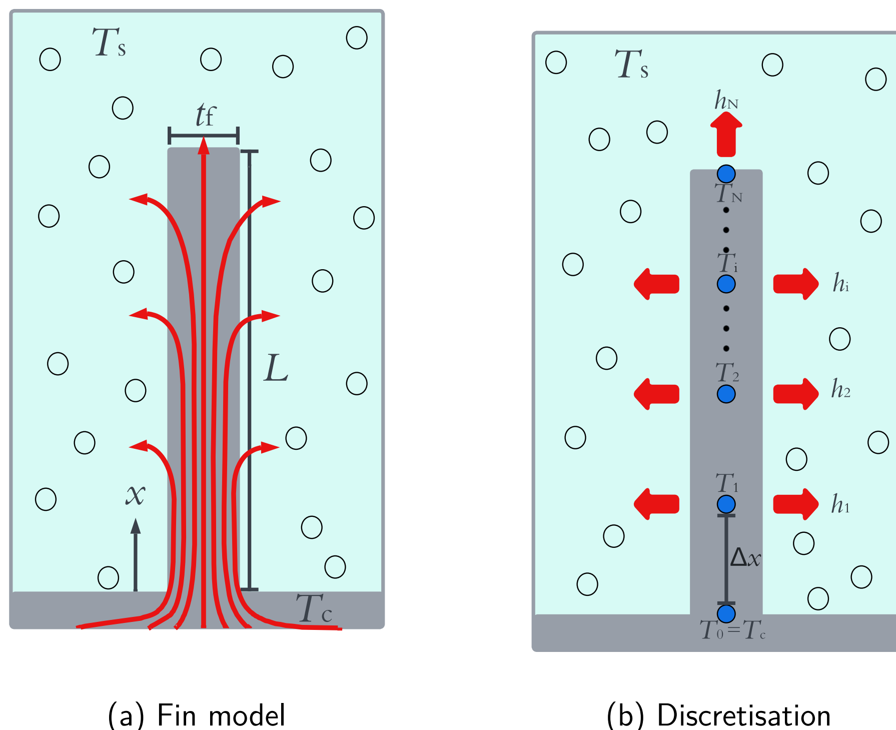

(a) Fin model (b) Discretisation

Figure 4.1: Diagrams depicting model of an immersed fin and discretisation into segments for numerical solving.

Fig. 4.1a depicts a square pin fin of width t_f and length L immersed in a pool of fluid at saturation temperature T_s. T denotes the temperature at a distance x along the fin length. Boiling of liquid along the fin sides is modelled as a temperature dependent heat transfer coefficient h. The fin material has a thermal conductivity k_f. The Biot number indicates the relative importance of thermal conduction within

a solid body compared to heat transfer from its surface. For the fin depicted in Fig. 4.1a, the Biot number is defined by Equation 4.1 [75].

$$Bi = \frac{h t_\mathrm{f}}{2 k_\mathrm{f}} \tag{4.1}$$

For Biot numbers significantly less than 1, it can be assumed the fin temperature is constant across its cross section and only varies with distance along its length. If the maximum heat transfer coefficient value is 1.5 W/(cm^2 K) and the fin is made from aluminium with thermal conductivity 170 W/(m K), the Biot number for a 5.6 mm width fin (i.e. the width of one GS-065-150-1-D2 switch) is 0.26. The one-dimensional heat equation for the depicted fin can be then expressed as follows [14].

$$\frac{\mathrm{d}^2 T}{\mathrm{d}x^2} = \frac{4h}{k_\mathrm{f} t_\mathrm{f}}(T - T_\mathrm{s}) \tag{4.2}$$

A constant temperature T_c is imposed at the fin base ($x = 0$). The fin tip $x = L$ is exposed to the same heat transfer coefficient as the sides, evaluated at the tip temperature. This yields the following boundary condition.

$$k_\mathrm{f} \left.\frac{\mathrm{d}T}{\mathrm{d}x}\right|_{x=L} = h|_{x=L}(T|_{x=L} - T_\mathrm{s}) \tag{4.3}$$

The total heat Q_f transferred through the fin is calculated using Equation 4.4 derived by applying Fourier's law at the fin base.

$$Q_\mathrm{f} = -k_\mathrm{f} t_\mathrm{f}^2 \left.\frac{\mathrm{d}T}{\mathrm{d}x}\right|_{x=0} \tag{4.4}$$

4.1.1 Numerical Solution Procedure

The fin heat transfer problem is solved numerically by dividing the fin into an integer number of segments N with equal length Δx, which defines N unknown temperatures $T_1, T_2, ...T_i...T_N$ and corresponding heat transfer coefficients $h_1, h_2, ...h_i...h_N$ as shown in Fig.4.1b. Equation 4.2 is discretised using the central difference approximation for the second derivative. This yields $N-1$ equations with the form of Equation 4.5 in terms of the N unknown temperatures and the base temperature T_c.

$$\frac{T_{i+1} - 2T_i + T_{i-1}}{\Delta x^2} = \frac{4h_i}{k_\mathrm{f} t_\mathrm{f}}(T_i - T_\mathrm{s}) \tag{4.5}$$

Equation 4.6 is obtained from the tip boundary condition by applying the backwards Euler approximation for the derivative, completing the system of N equations in N unknowns.

$$k_{\mathrm{f}}\frac{T_{N-1}-T_N}{\Delta x}=h_N(T_N-T_{\mathrm{s}}) \tag{4.6}$$

These equations can be combined to form a single non-linear equation relating tip temperature T_N to base temperature T_{c} which is solved numerically for T_N to a specified error tolerance. The total heat transfer through the fin is calculated by applying the forwards Euler approximation to Equation 4.4.

$$Q_{\mathrm{f}}=k_{\mathrm{f}}t_{\mathrm{f}}^2\frac{T_{\mathrm{c}}-T_1}{\Delta x} \tag{4.7}$$

4.1.2 Comparison with Analytical Solutions

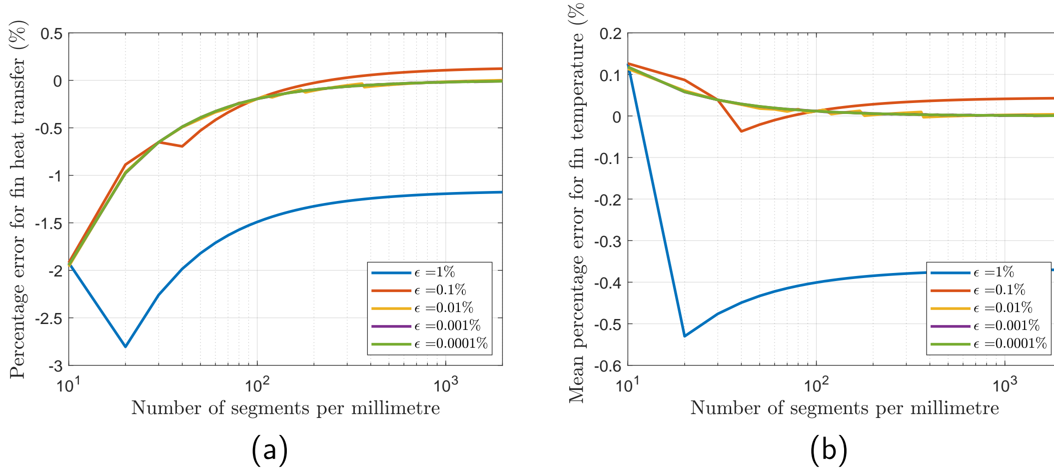

Figure 4.2: Percentage error for fin heat and mean percentage error for fin temperature with varying error tolerance ϵ and number of segments N.

To verify accuracy of the numerical solution procedure, it is compared against the analytical solution for a fin subject to a constant heat transfer coefficient. The number of segments N per mm of fin length and the error tolerance ϵ are varied and a mean percentage error for the temperature is computed, shown in Fig. 4.2b. The fin heat percentage error is also shown in Fig. 4.2a. For both quantities, when N is large, the error converges to a constant value irrespective of

N which is determined only by the error tolerance. This final error value is observed to decrease considerably with decreasing error tolerance until $\epsilon = 0.01\%$; only negligible improvements were observed at smaller values. One thousand segments per millimetre was selected; with these parameters the heat transfer percentage error is 0.016 % and mean percentage error for temperature is 0.0024 %.

It is necessary also to consider the accuracy of the numerical method for cases where the heat transfer coefficient depends on fin temperature. One example for which an analytical solution exists is a constant heat flux q. The fin heat equation can then be expressed as follows.

$$\frac{\mathrm{d}^2 T}{\mathrm{d}x^2} = \frac{4q}{k_\mathrm{f} t_\mathrm{f}} \tag{4.8}$$

Solving for the temperature subject to a convective boundary condition at the fin sides and tip yields Equation. 4.9. A derivation is presented in Appendix B.

$$T = \frac{2q}{k_\mathrm{f} t_\mathrm{f}} x^2 - \left(\frac{q}{k_\mathrm{f}} + \frac{4qL}{k_\mathrm{f} t_\mathrm{f}} \right) x + T_\mathrm{c} \tag{4.9}$$

The fin heat transfer evaluated via Equation 4.4 can be expressed as below.

$$Q_\mathrm{f} = q t_\mathrm{f}^2 + 4qLt_\mathrm{f} \tag{4.10}$$

One thousand fins of length 1 mm to 10 mm and widths 0.5 mm to 5 mm with heat flux between 1 W/cm^2 and 10 W/cm^2 were evaluated using both the numerical method and the analytical solution. Fig. 4.3b shows the ratio of fin heats computed numerically and analytically. The largest percentage deviation is 0.1 %. The mean ratio of temperature along the fin is also displayed in Fig. 4.3a with a maximum percentage error of 0.05 %. The numerical approach is thus deemed sufficiently accurate to inform design procedures for practical heat spreaders.

4.2 Heat Spreader Design

In this work, heat spreaders are designed for the target application of a PCB-based converter with compact electrical layout using GS-065-150-1-D2 switches from GaN systems. As shown in Fig. 2.7, the heat spreader would attach to an immersed

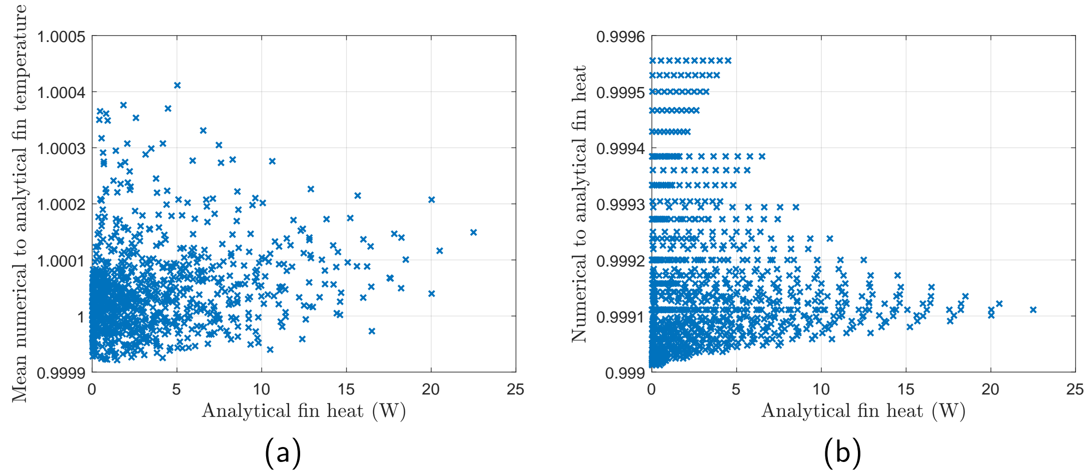

Figure 4.3: (a) Mean ratio of numerically computed fin temperature to analytical solution and (b) Ratio of numerically computed fin heat to analytical solution for 1000 different fins.

semiconductor switch and comprises a baseplate with normally protruding fins. It is desirable to integrate ancillary components like ceramic capacitors and control circuitry in close proximity to the switch. This imposes several practical constraints on the heat spreader geometry and fin arrangement.

- The heat spreader should not extend laterally outwards beyond the planar area of the semiconductor switch surface as this necessitates spacing out of switches and surrounding components. All fin arrangements considered fit within the 12.6 mm by 5.6 mm footprint of the GS-065-150-1-D2 switch.

- The maximum useful fin length is set to 4 mm. A survey of ceramic capacitors in 2220 package indicates the largest height available is 5.4 mm. A spreader with baseplate of thickness 1 mm with 4 mm fins can be bonded to the 0.27 mm GS-065-150-1-D2 die with no penalty on the converter height and volume.

- Tool size limitations associated with the milling process used to prepare finned surfaces restrict the spacing between fins to be greater than 1.2 mm. In previous research, it is recommended the fin spacing should be greater than the bubble diameter to prevent coalescence of bubbles within the gaps [22]. To ensure this condition is met, the bubble diameter is estimated for Novec 7000

using Equation 3.6 for fluid saturation temperatures from 65 °C to 100 °C and plotted in Fig. 4.4. The minimum fin spacing is over twice the maximum bubble diameter which is sufficient to prevent vapour crowding.

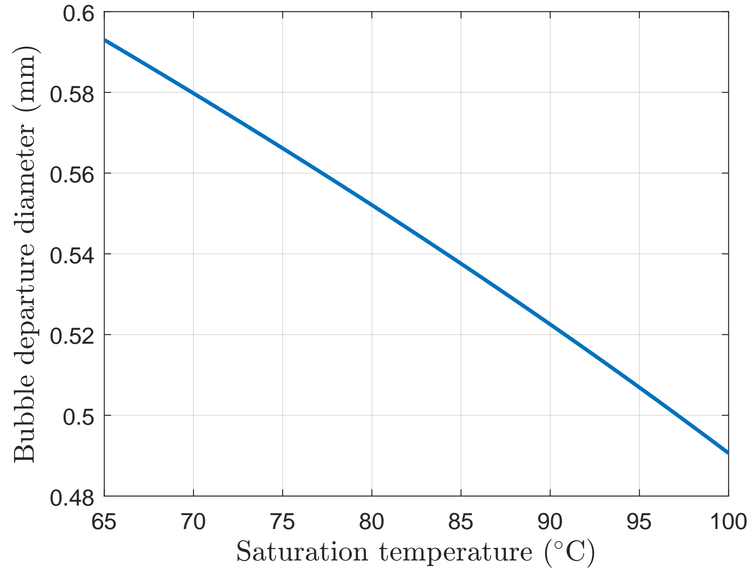

Figure 4.4: Bubble departure diameter for Novec 7000 as a function of saturation temperature.

For fins of length 4 mm with widths 0.5 mm to 5.6 mm satisfying the above conditions, an area enhancement value is calculated and plotted in Fig. 4.5. This represents the ratio of heat spreader area A_c to the switch area A_sw. For a heat spreader with N_f fins, it can be expressed as below.

$$\text{Area enhancement} = \frac{A_\mathrm{sw} + 4N_\mathrm{f}t_\mathrm{f}L}{A_\mathrm{sw}} \tag{4.11}$$

The area enhancement is observed to increase linearly with fin width in segments. At the end of each segment, the number of rows or columns must decrease to accommodate a wider fin and this is accompanied by a substantial reduction in area. Three candidate fin arrangements are identified. The first has 18 fins with width 1 mm, which yielded the highest area enhancement. The 2 mm fin offers slightly lower surface area than 1 mm though the increase in fin width will improve conduction heat transfer through the cross section. Finally, two fins of 5.6 mm width are considered.

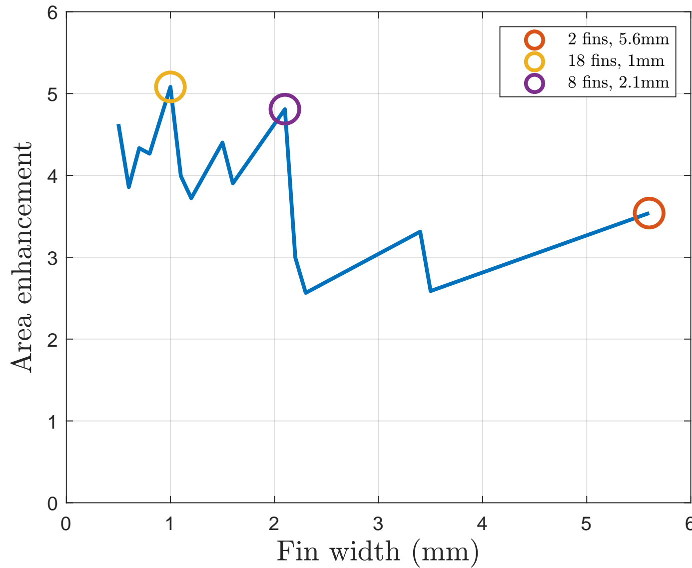

Figure 4.5: Area enhancement for heat spreaders with varying fin width.

4.2.1 Modelling Finned Heat Spreaders

For the semiconductor switch with attached heat spreader depicted in Fig. 2.7, the total power dissipated by the switch can be calculated by summing the following three contributions .

1. Heat transferred to fluid via the surface at the fin base. This is modelled using the piecewise fitted Rohsenow correlation for boiling Novec 7000 on horizontal surfaces detailed in Chapter 3, evaluated at temperature T_c.

2. Heat transferred through the baseplate sides. Assuming temperature variation within the baseplate is negligible, this can also be evaluated using the piecewise fitted Rohsenow correlation at temperature T_c.

3. Heat transferred through the fins. This is calculated via the numerical solution procedure using the piecewise fitted Rohsenow correlation to model the temperature dependent heat transfer coefficient. This assumes the vertical orientation of the fin sides does not impact boiling behaviour.

The semiconductor switch surface temperature T_{sw} is estimated from the fin base temperature T_{c} and baseplate thickness t_{sp} using Fourier's law via Equation 4.12.

$$T_{\mathrm{sw}} = T_{\mathrm{c}} + \frac{t_{\mathrm{sp}}}{k_{\mathrm{f}} A_{\mathrm{sw}}} Q_{\mathrm{c}} \tag{4.12}$$

The switch-level heat transfer coefficient can then be evaluated by Equation 2.4. It is plotted in Fig. 4.6 for the three selected fin arrangements with lengths from 0 mm to 4 mm. Fluid saturation temperature T_{s} is 100 °C and the fin base temperature T_{c} is 125 °C. The heat spreader with eight 2 mm wide and 4 mm long fins exhibits the highest switch-level heat transfer coefficient of 3.5 W K/cm. Furthermore, it is clear that further increase in fin length would yield negligible improvement in switch-level heat transfer coefficient at the expense of increased system volume. This is because of resistance to thermal conduction through the fin length .

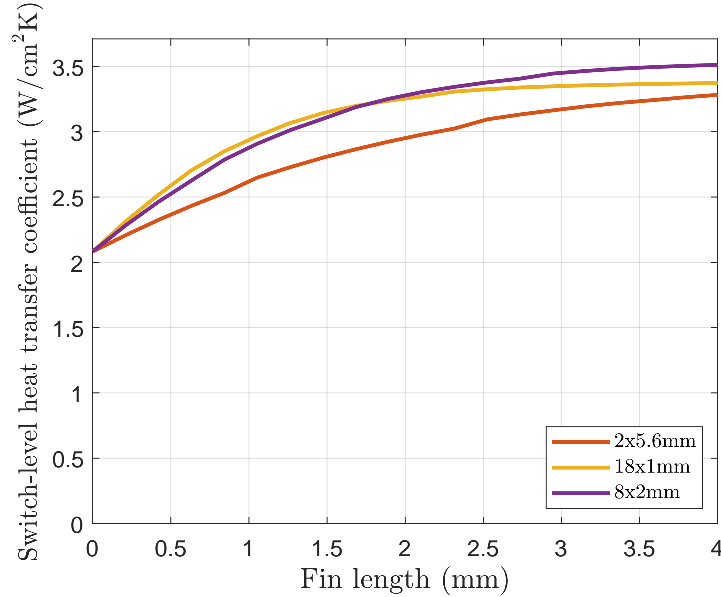

Figure 4.6: Switch-level heat transfer coefficients for three candidate heat spreader arrangements with fins of varying length.

In previous work, it is observed that once critical heat flux occurs at the fin base, portions of the fins remain free of vapour [40]. Consequently, the increase in temperature associated with critical heat flux is moderate compared with for flat surfaces and it may be possible to sustain higher switch level power dissipations. Nevertheless, in this work, the highest useful switch power is computed as that

which incipits critical heat flux on the baseplate surface. This is shown in Fig. 4.7 for three fin arrangements with varying lengths. Once again, the 2 mm wide fin yields best performance with switch-level critical heat flux of 114 W/cm^2 at a fin length of 4 mm. This is 2.7 times greater than the critical heat flux measured for a flat surface. Based on these results, the 2 mm fin spreader was selected for experimental characterisation in Novec 7000 fluid.

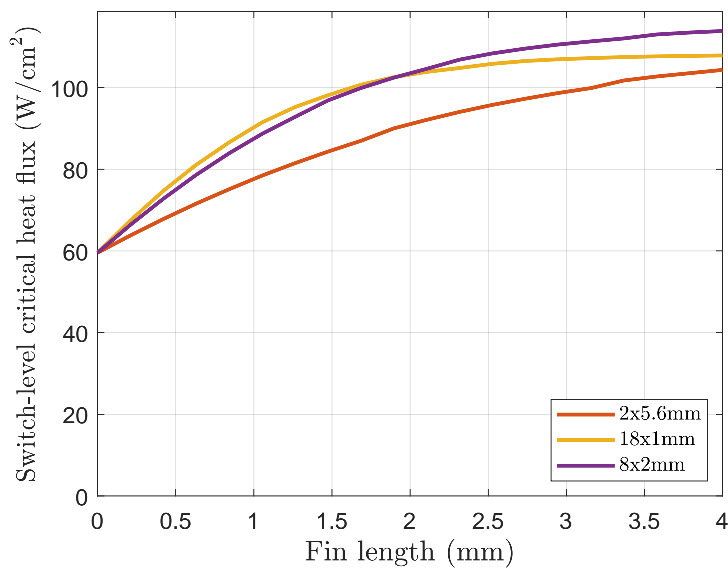

Figure 4.7: Switch-level critical heat fluxes for three candidate heat spreader arrangements with fins of varying length.

4.3 Experimental Verification

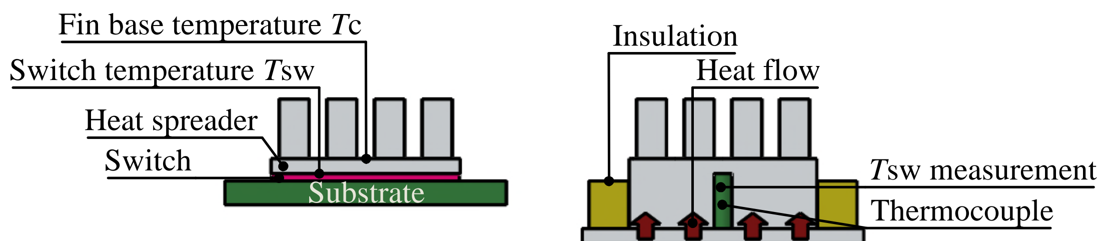

Figure 4.8: Diagram showing correspondence between a semiconductor switch with heat spreader and its facsimile.

The experimental approach used to validate the predicted performance of

Table 4.1: Experimental uncertainties on calculated quantities for smooth and grit blasted heat spreader facsimiles.

Quantity	**Smooth facsimile**	**Grit blasted facsimile**
Average switch facsimile temperature T_{sw}	± (1.4 %-2.1 %)	± (1.4 %-2.2 %)
Saturation temperature T_s	± (0.5 %-1.2 %)	± (0.4 %-1.3 %)
$T_{sw} - T_s$	± (9.1 %-37.8 %)	± (12.1 %-59.1 %)
Total power dissipation	± (0.2 %-0.3 %)	± (0.2 %-0.3 %)
Effective heat flux	± 1.6 %	± 1.6 %
Effective heat transfer coefficient	± (9.3 %-37.8 %)	± (12.2 % - 59.2 %)

finned heat spreaders is based on the facsimile concept. Fig. 4.8 illustrates the correspondence between a semiconductor switch with heat spreader attached and its facsimile machined in metal. The thermocouple insert is offset from the facsimile surface such that it provides measurements of the switch temperature T_{sw}.

The experimental apparatus used was the same as that detailed in Chapter 3. A modified heater block was prepared with additional 1 mm thickness of aluminium added to each facsimile and protruding fins machined into the top. Thermocouple inserts terminate 1 mm below the facsimile surface. In a further step, the exposed surfaces of all facsimiles were grit blasted in an effort to favourably modify the surface geometry; data was collected for both smooth and grit blasted facsimiles.

Heat loss to ambient air through the PEEK insulators was separately characterised for the modified heater block though the linear relationship between facsimile temperature and heat loss was very close to that obtained in Chapter3. Table 4.1 summarises the experimental uncertainty associated with calculated quantities for experiments with smooth and sand-blasted facsimiles. It should be noted the high experimental uncertainties occur for low values of effective heat transfer coefficient since $T_{sw} - T_s$ is small and highly sensitive to the thermocouple absolute uncertainty of 1.5 °C.

Due to safety limits on the system pressure, the apparatus was not tested beyond a total power dissipation of 186 W. This was insufficient to reach critical heat flux. The highest measured temperature at the maximal power dissipation was 110 °C

for the smooth facsimile and 107 °C for grit blasted.

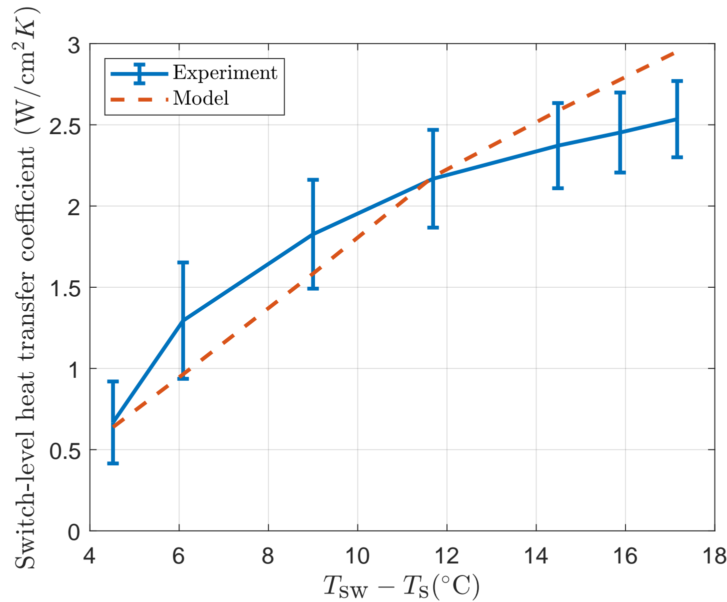

Figure 4.9: Experimental and theoretical switch-level heat transfer coefficients for the smooth heat spreader facsimile.

Fig.4.9 plots the experimentally derived switch-level heat transfer coefficient and corresponding theoretical predictions calculated at the measured saturation temperature and switch facsimile temperature. The model reasonably agrees with the data, with a mean absolute percentage difference of 12 %. Fig. 4.10 shows switch-level heat transfer coefficients for the smooth and grit-blasted heat spreader facsimiles compared with results for the planar bare switch facsimile from Chapter 3. It is clear the proposed finned heat spreader improves performance by a factor of 1.7; this increased further to a factor of 2.3 by applying grit blasting.

In an effort to characterise critical heat flux for the smooth heat spreader facsimile, an experiment was conducted with PEEK caps covering five of the six facsimiles. Power was supplied via two of the four cartridge heaters which were closest to the exposed facsimile. The switch-level heat flux calculated by normalising the total power dissipation to the area of a single switch facsimile is shown in Fig. 4.11.

The maximum heat flux tested was 126 W/cm^2 with no apparent indication of critical heat flux. For comparison, the value predicted by the model is 101 W/cm^2. The discrepancy between experiment and theory could be due to heat transfer

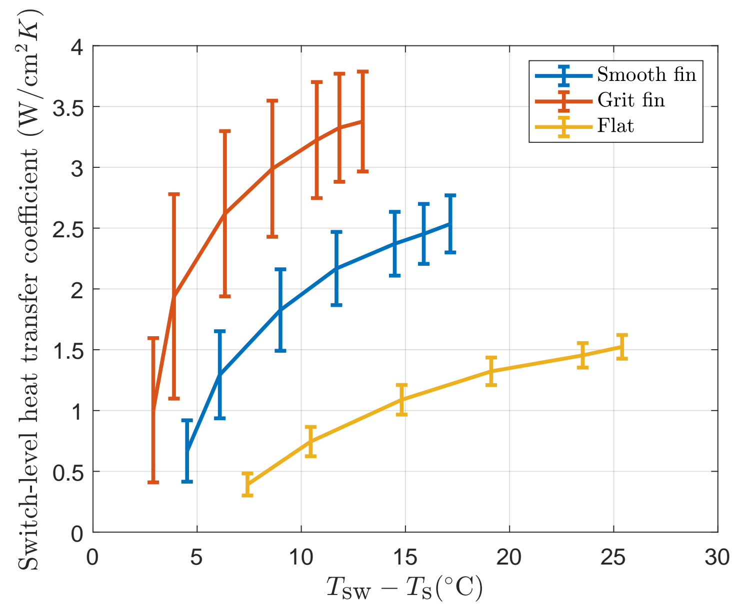

Figure 4.10: Experimental switch-level heat transfer coefficients for the smooth and grit blasted heat spreader facsimiles as well as the planar facsimile from Chapter 3.

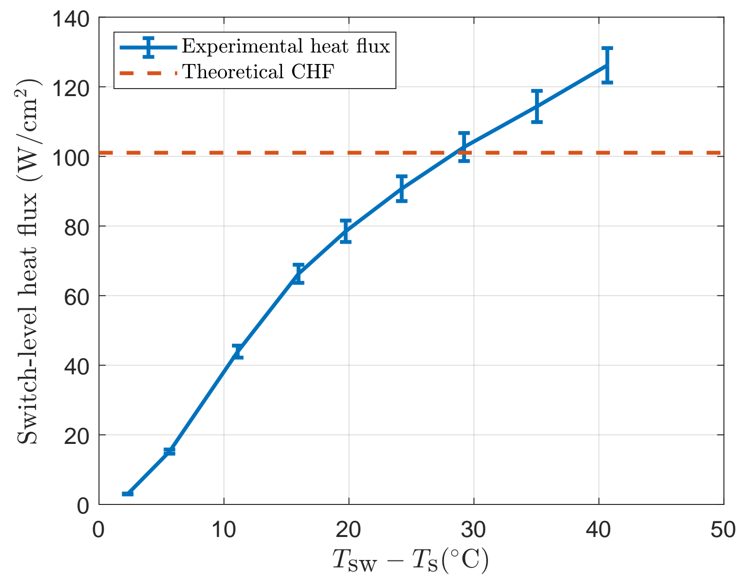

Figure 4.11: Measured switch-level heat fluxes for a single smooth heat spreader facsimile compared with theoretical prediction.

from the covered up switch facsimiles which could not be completely eliminated. Nevertheless, both theory and experiment indicate that heat fluxes in excess of 100 W/cm^2 can be sustained by the proposed heat spreader.

4.4 Conclusions

This chapter provides several key insights into boiling heat transfer on pin fins arrays which can be used to instruct design of heat spreaders for two-phase immersion cooled systems.

- By considering practical geometrical constraints, heat spreaders can be designed for electrically compact PCB-based converters to increase the power dissipation per unit switch area with negligible impact on system volume. This is demonstrated by design of a heat spreader for the GS-065-150-1-D2 switch. Experiments indicate that a grit-blasted heat spreader yields switch-level heat transfer coefficient of $3.4\,\mathrm{W/(cm^2\,K)}$, over two times greater than that for a planar surface.

- Theoretical predictions and experimental results indicate the proposed heat spreader can sustain switch-level heat fluxes in excess of $100\,\mathrm{W/cm^2}$. This is 2.4 times greater than the value observed for a planar surface.

- The switch-level heat transfer coefficient for a finned heat spreader can reasonably be predicted using experimentally derived boiling correlations to model the temperature dependent heat transfer coefficients on the fin sides and tip. Due to the non-linear dependence of heat transfer coefficient on temperature, numerical methods can be applied to solve problems and these have been verified by comparing with simple cases for which analytical solutions exist.

5
Power Density of Two-Phase Immersion Cooled Converters

Previous studies on two-phase immersion cooling for electronics have largely focused on systems where semiconductor switches are submerged in a fluid pool coupled to a separate commercial heat exchanger which condenses the fluid. These systems demonstrate CSPI values of 17 W/(L K) when the heat exchanger flow side is air-cooled [42] and 45 W/(L K) using water cooling [53].

The two-phase immersion concept considered in this work is intended for converters on PCB substrates and is depicted in Fig. 1.3 The dielectric fluid is enclosed by two chambers which seal to the top and bottom sides of the PCB with heat exchanger integrated into the top chamber. This chapter aims to demonstrate a practical design of the concept which can achieve high CSPI, paving the way towards high power density converters on PCB substrates. The target application is an electric vehicle motor drive inverter with six GS-065-150-1-D2 switches immersed in Novec 7000 fluid. As per the Automotive Centre UK recommendations, the heat exchanger flow side is cooled with 65 °C water.

A preliminary contribution is development of a theoretical model and numerical solution approach for condensation heat transfer on downward-facing fins. The model can be employed to design the condenser side for heat exchangers and is

verified against experimental data collected with the apparatus of Chapter 3. Based on the experimental performance of the heat exchanger, a practical two-phase immersion system is designed for the inverter and characterised in terms of the CSPI and HEPI metrics defined previously.

During operation, it is important to ensure the system contains only pure vapour with minimal quantities of non-condensible gases. In the final part of the chapter, preliminary experiments are conducted to explore the impact of leakage and outgassing on performance.

5.1 Condensation on Finned Surfaces

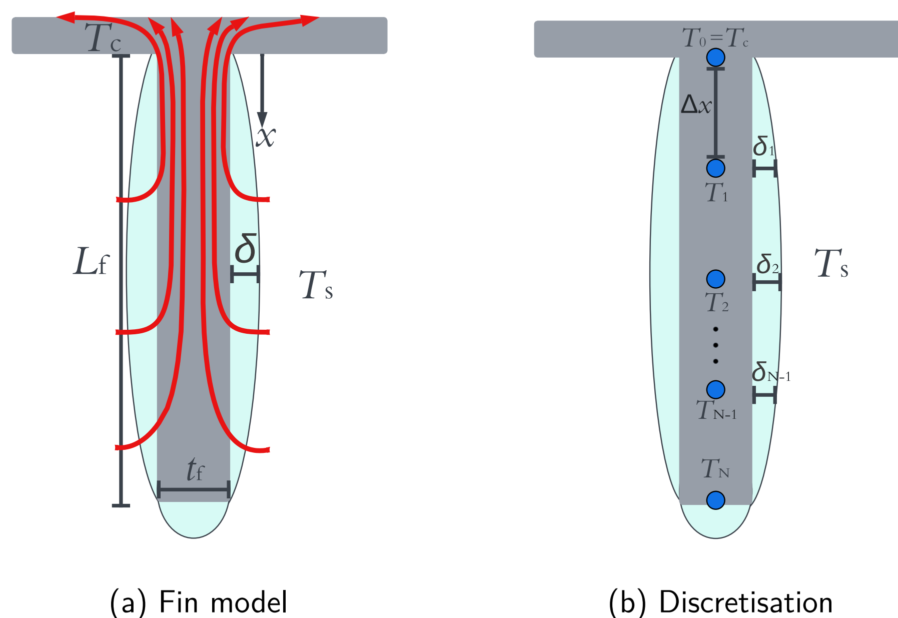

Figure 5.1: Diagrams depicting model of gravity-driven condensation on a fin and discretisation into segments for numerical solving.

Fig. 5.1 depicts the mechanism of heat transfer for a square pin fin of thickness t_f, length L and material thermal conductivity k_f in contact with a vapour at saturation temperature T_s. In most engineering applications, the condensate fully wets the surface, forming a film of varying thickness δ along the fin sides. Assuming heat is transferred predominantly by conduction through the condensate with thermal

conductivity k_l the heat equation for the fin temperature T can be expressed as follows. It is subject to a constant temperature boundary condition T_b at the fin base.

$$\frac{\mathrm{d}^2T}{\mathrm{d}x^2} = \frac{4k_\mathrm{l}}{k_\mathrm{f}t_\mathrm{f}\delta}(T - T_\mathrm{s}) \tag{5.1}$$

Under the influence of gravity and surface tension, condensate drains down the fin sides and gathers at the tip, with droplets periodically detaching and returning to the fluid pool. Since the condensate layer is comparatively thick at the fin tip for significant portions of the time, negligible heat transfer through this surface is assumed. The boundary condition at the tip is expressed by Equation 5.2

$$k_\mathrm{f}\left.\frac{\mathrm{d}T}{\mathrm{d}x}\right|_{x=L} = 0 \tag{5.2}$$

The condensate film shape is governed by the balance of gravitational and surface forces acting on the film. Assuming gravity is the dominant force, the film thickness can be modelled by Equation 5.3 derived in Nusselt's theory of condensation on vertical walls [14].

$$\delta^3\frac{\mathrm{d}\delta}{\mathrm{d}x} = \frac{\mu_\mathrm{l}k_\mathrm{l}(T_\mathrm{s} - T)}{l_\mathrm{lv}\rho_\mathrm{l}(\rho_\mathrm{l} - \rho_\mathrm{v})g} \tag{5.3}$$

To verify this assumption, the Bond number can be used to characterise the relative importance of gravity and surface tension. It is defined in Equation 5.4 [14].

$$\mathrm{Bo} = \frac{(\rho_\mathrm{l} - \rho_\mathrm{v})gL^2}{\sigma_\mathrm{l}} \tag{5.4}$$

Fig. 5.2 plots the fin length corresponding to different Bond numbers for Novec 7000 at temperatures from 65 °C to 100 °C. For fins longer than 1 mm, the Bond number is greater than one for all temperatures, meaning gravitational forces dominate over significant portions of the length.

5.1.1 Numerical Solution Procedure

The equations for heat transfer through a fin subject to surface condensation are solved using a numerical approach similar to that discussed in Chapter 4, modified to incorporate solution of Equation 5.3 for the film thickness. Figure. 5.1b

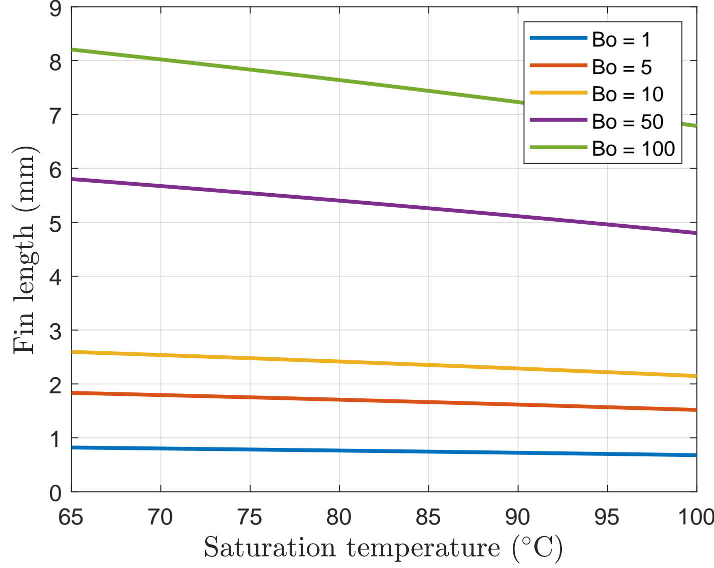

Figure 5.2: Lengths of fin corresponding to different Bond numbers for varying fluid saturation temperature.

demonstrates discretisation of the fin into N equal segments of length Δx, defining N temperatures $T_1, T_2, ...T_i...T_N$ and N film thicknesses $\delta_1, \delta_2, ...\delta_i, ...\delta_N$. Applying the central difference approximation for second derivatives yields the discretised heat equation below.

$$\frac{T_{i+1} - T_i + T_{i-1}}{\Delta x^2} = \frac{4k_\mathrm{l}}{k_\mathrm{f} t_\mathrm{f} \delta_i}(T_i - T_\mathrm{s}) \tag{5.5}$$

Film thickness is evaluated by approximating the first derivative as a forward difference, leading to Equation 5.6.

$$\delta_{i+1} = \delta_i + \frac{\mu_\mathrm{l} k_\mathrm{l} (T_\mathrm{s} - T_i)\Delta x}{l_\mathrm{lv}\rho_\mathrm{l}(\rho_\mathrm{l} - \rho_\mathrm{v}) g {\delta_i}^3} \tag{5.6}$$

Since film thickness δ_0 at the fin base iz zero, this expression yields infinite film thickness δ_1 after the first segment. Consequently, a backward difference approximation is used for this case only, resulting in the following relation. All remaining film thicknesses are evaluated via Equation 5.6.

$$\delta_1 = \left(\frac{\mu_\mathrm{l} k_\mathrm{l} (T_\mathrm{s} - T_1)\Delta x}{l_\mathrm{lv}\rho_\mathrm{l}(\rho_\mathrm{l} - \rho_\mathrm{v}) g}\right)^{\frac{1}{4}} \tag{5.7}$$

The insulated tip boundary condition can be approximated using a forward difference, yielding Equation 5.8.

$$k_{\mathrm{f}} \frac{T_{N-1} - T_N}{\Delta x} = 0 \tag{5.8}$$

This approach yields a set of $2N$ non-linear equations in terms of N film temperatures and N film thicknesses which can be combined to yield one equation in terms of a single temperature. This can be solved numerically to some error tolerance.

To validate the numerical approach for calculating the fin thickness, it is compared against the analytical solution which can be derived from Equation 5.3 when the fin is isothermal at temperature T_{b}.

$$\delta = \left(\frac{4\mu_{\mathrm{l}} k_{\mathrm{l}} (T_{\mathrm{s}} - T_{\mathrm{b}}) x}{l_{\mathrm{lv}} \rho_{\mathrm{l}} (\rho_{\mathrm{l}} - \rho_{\mathrm{v}}) g} \right)^{\frac{1}{4}} \tag{5.9}$$

Fig. 5.3 shows the mean percentage error in film thickness with varying number of segments for a fin of length 10 mm and temperature 65 °C in contact with Novec 7000 vapour at 100 °C. For 1000 segments per mm, the mean percentage error is only 0.07 %.

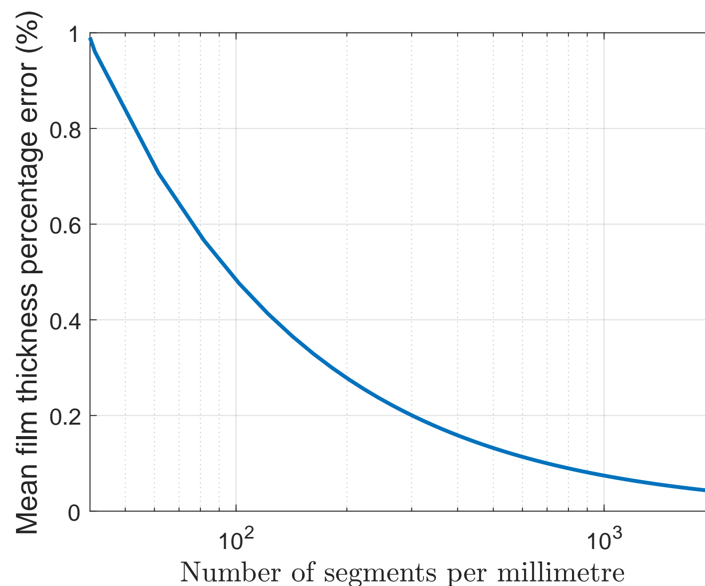

Figure 5.3: Mean percentage error in film thickness for different numbers of segments.

5.1.2 Heat Exchanger Design

The experimental apparatus detailed in Chapter 3 features a borosilicate glass chamber with internal diameter 45 mm; this size was selected to accommodate six GS-065-150-1-D2 semiconductor switches. The heat exchanger condenser side thus also features a 45 mm diameter surface exposed to saturated vapour which is enhanced with square pin fins to increase the contact area. In Chapter 4 for pin fins immersed in boiling Novec 7000, it was observed that 2 mm thick fins offered a good compromise between surface area and conduction through the cross section. Furthermore, inter-fin spacing was set as 1.2 mm, the smallest value accommodated by the CNC machining process. 117 such fins were incorporated into the condenser side.

Fig. 5.4 shows the predicted total heat transfer across the heat exchanger for fin lengths up to 10 mm. Longer fins were not considered due to restrictions on cutting depth. The vapour saturation temperature is 100 °C and the fin base is at 65 °C. A fin length of 7.5 mm was selected for the heat exchanger. Only minor improvement was observed with further increase in fin length, at the expense of greater heat exchanger volume. The predicted heat transfer was 300 W. Also shown is the predicted heat transfer of 57 W for condensation on a planar surface without fins. This was calculated using the model proposed in [76] by Gerstmann and Griffith where surface tension is the primary mechanism for condensate drainage and determines the film shape. That the presence of fins increases the heat transfer by a factor of five indicates the importance of features to maximise surface area.

5.2 Experimental Results

The proposed heat exchanger condenser side model is verified against data collected with Novec 7000 dielectric fluid in Chapter 3. Specifically, the thermocouples embedded in the heat exchanger provide measurements of temperature at the fin base T_{b}. These are plotted for the flat, smooth finned and grit-blasted finned switch facsimile tests in Fig. 5.5a. The fluid saturation temperature is obtained

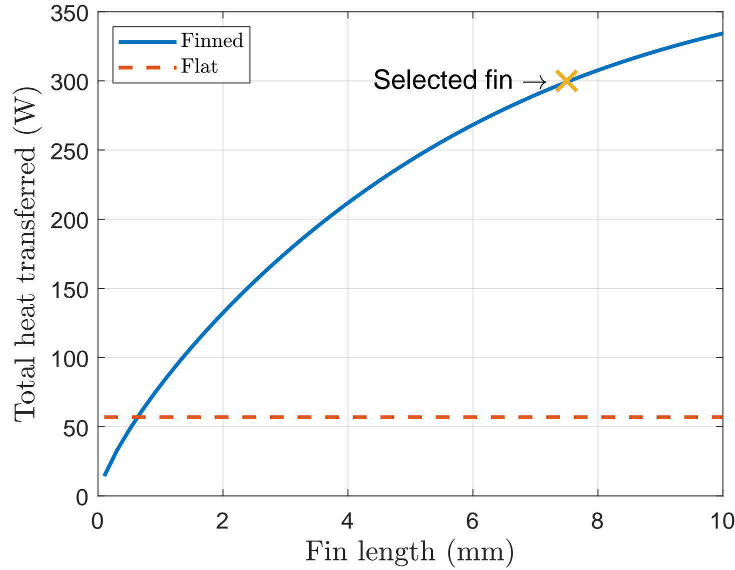

Figure 5.4: Total heat transfer across heat exchanger for a flat surface and enhanced with fins of varying length.

from the pressure measurement via Equation 3.3 and shown for all three switch facsimiles in Fig. 5.5b. Temperature measurements agree closely for the three tests, demonstrating repeatability of the heat exchanger performance.

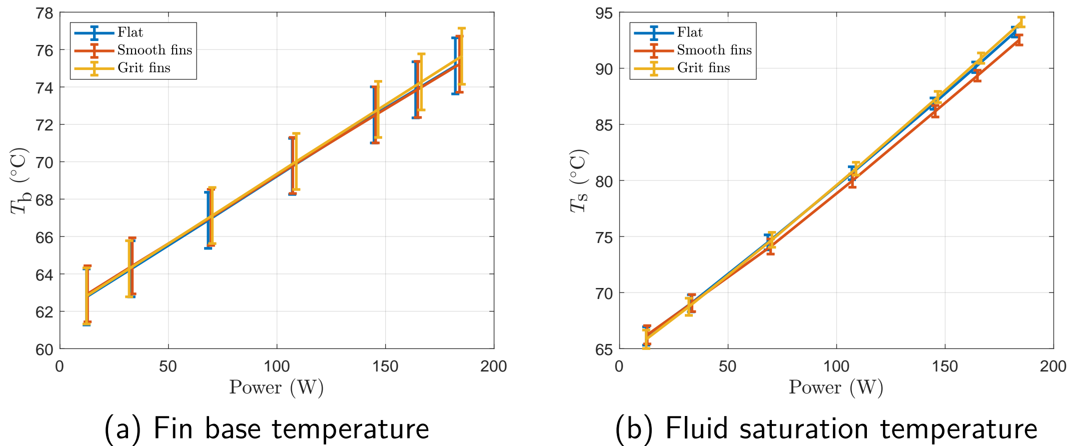

(a) Fin base temperature (b) Fluid saturation temperature

Figure 5.5: Fin base temperature and fluid saturation temperature for experiments conducted with three different switch facsimile types.

Fig. 5.6 shows the difference between the fluid saturation temperature T_s and the fin base temperature T_b as a function of the total power dissipation. For comparison, values computed using the film condensation model are also shown. The theory

under-predicts temperature rise at low power dissipations but accurately reproduces the experimental results for high power.

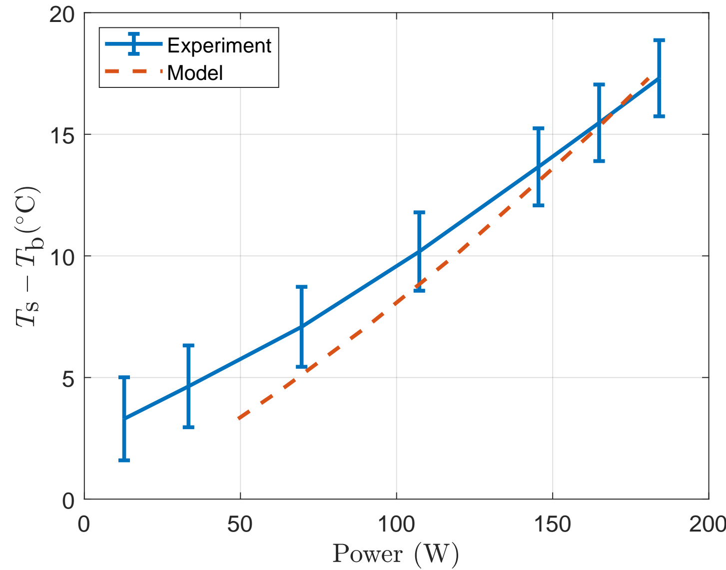

Figure 5.6: Temperature difference between fluid and fin base as a function of temperature. Experimental results and model predictions are shown for comparison.

Fig.5.7 shows the measured switch facsimile temperature, fluid saturation temperature and fin base temperature for the flat and grit blasted finned facsimiles at their respective maximum power dissipations. The heat exchanger flow side inlet temperature is maintained at 65 °C by the circulating water bath. For the flat facsimile, the total power dissipation is 182 W and the measured facsimile temperature is 126 °C, yielding a thermal resistance of 0.34 K/W to the flow side inlet. Almost half of the thermal resistance is due to boiling on the facsimile surface. For the grit-blasted finned facsimile, the total power dissipation is 186 W and the measured facsimile temperature is 107 °C with a thermal resistance of 0.23 K/W. The heat exchanger condenser side is now the most significant contributor to thermal resistance, accounting for 44 %.

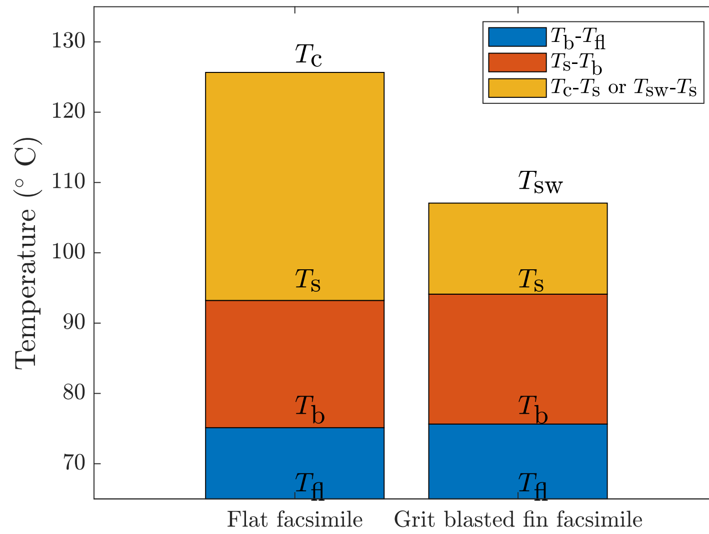

Figure 5.7: Temperatures measured at the fin base, the fluid and the switch facsimile for flat and grit-blasted fin facsimiles.

5.3 Motor Drive Inverter

5.3.1 Two-Phase Immersion Cooling Performance

A two-phase immersion cooling system for motor drive inverter is shown in Fig. 5.8. The converter circuit consists of six GS-065-150-1-D2 switches on a PCB substrate. 14 decoupling capacitors of value 0.2 µF are incorporated to mitigate effects of parasitic inductance in the power loop. Total decoupling capacitance is over 100 times greater than the semiconductor switch output capacitance [73], in line with recommendations from the literature [7]. Gate driver circuitry would be laid out on the bottom side of the circuit board in close proximity to the switches in order to minimise gate loop inductance. It is assumed a grit-blasted heat spreader with 8 fins of thickness 2 mm is attached to each switch.

The heat exchanger is a rectangular aluminium part designed to give comparable thermal performance to the circular heat exchanger employed in experiments. Consequently, the condenser side consists of 120 7.5 mm long fins and the flow side features an arrangement of channels with the same surface area as in experiments. The heat exchanger volume is 0.04 L. From Fig. 5.7, the total thermal resistance

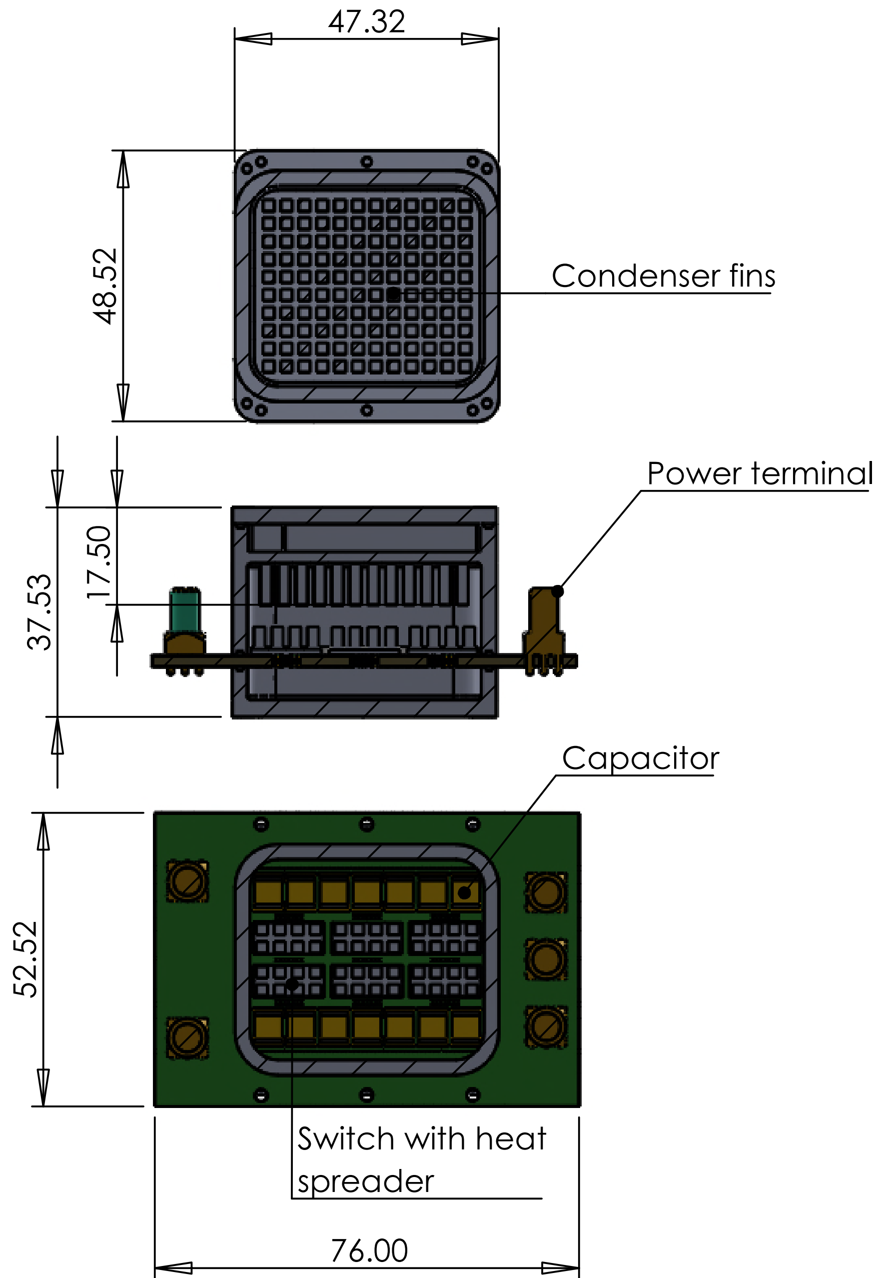

Figure 5.8: Diagram of the proposed motor drive inverter on PCB substrate enclosed in a two-phase immersion cooling chamber.

associated with the heat exchanger (i.e. from the dielectric fluid to the flow side inlet) is 0.15 K/W. The heat exchanger performance index can be calculated via Equation 2.6 as 167 W/(L K).This is significantly better than the 40 W/(L K) demonstrated by commercial fin/tube radiators [50] and approaches the performance of parallel plate water heat exchangers (300 W/(L K) [53]) with the additional

advantage of integrating the fluid chamber and heat exchanger as a single part.

To seal the dielectric fluid, it is proposed to use elastomer O-rings. These would sit in glands formed between a groove in the chamber wall and an exposed copper trace on the circuit board. Consequently, a portion of the PCB extends outward beyond the chamber wall. Terminals used to pass power into and out of the converter are located externally to the chamber; connections between the circuit and terminals would be made by copper traces in internal layers such that the sealing trace can be unbroken. The boxed volume enclosing the circuit board and fluid chamber is 0.15 L. The thermal resistance from switch surface to flow side inlet is equal to the experimentally measured value of 0.23 K/W for grit blasted fins. A CSPI value of 30 W/(L K) is thus achieved. This substantially improves on the 5 W/(L K) previously demonstrated for a similar integrated chamber and heat exchanger design [57]. Furthermore, it exceeds the best performance of systems with separate air-cooled radiators (17 W/(L K) [42]) and approaches that offered by parallel plate liquid heat exchangers (45 W/(L K) [53]). while also facilitating close integration of switches, decoupling capacitors and gate drivers.

5.3.2 Leak Testing

In practical two-phase immersion cooling systems, it is desirable to purge both chamber and fluid of non-condensible gases (NCGs) prior to operation. This is because they can stratify close to the condenser surface, drastically degrading its performance [15]. Furthermore, elevated pressures due to presence of NCGs can elevate the switch surface temperature required for boiling incipience [77]. When purged of NCGs, the chamber is saturated with dielectric fluid vapour and the internal pressure is usually sub-atmospheric at room temperature (i.e. when the converter is not in operation). In this case, there are several mechanisms by which gases can enter the chamber.

- Leakage through the O-rings which seal the fluid chambers to the PCB.
- Outgassing of contaminants from the PCB and elastomer seals under sub-atmospheric pressure.

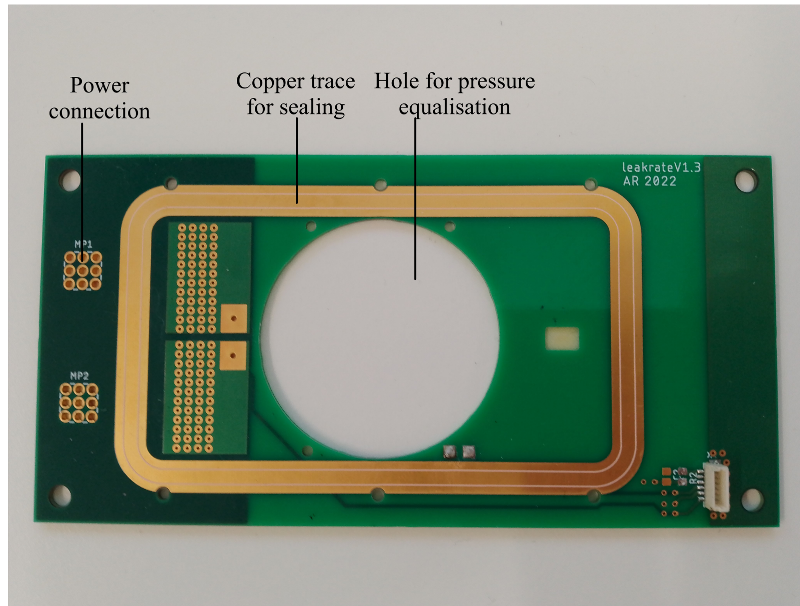

(a) Leak test PCB

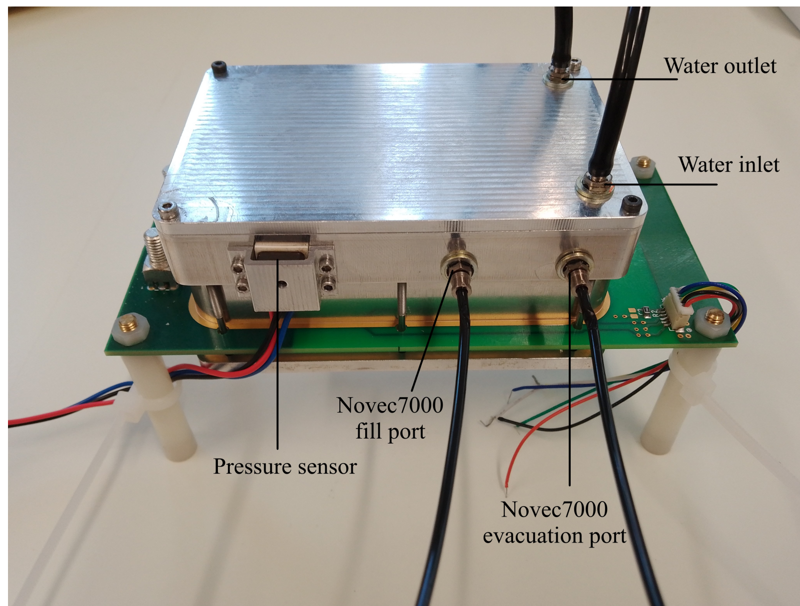

(b) Leak test apparatus

Figure 5.9: Photographs of printed circuit board and full test apparatus used to investigate leakage of non-condensible gases.

- Leakage through sealing elements like bonded seals which connect fittings/ports to the chamber.
- Release of gases dissolved in the working fluid under sub-atmospheric pressure.

An experimental apparatus was developed, shown in Fig. 5.9, to investigate the

impact of non-condensible gas on performance during repeated power cycles. A printed circuit board was fabricated with unmasked electroless nickel immersion gold (ENIG) finish copper traces on the top and bottom layers. Two aluminium chambers are fastened to either side of the PCB using six M2 bolts. Grooves are machined into the aluminium chamber wall surfaces which contact the exposed trace on the circuit board, forming a gland which fits a 1 mm thick nitrile O-ring. Novec 7000 dielectric fluid is delivered to the chamber through a fill port attached via a bonded seal. The fill port is then closed with a clip and a small quantity of fluid is boiled off to atmosphere through the evacuation port which is subsequently also closed. The chamber is then sealed and full of saturated vapour.

A coil of bare copper wire is soldered to the circuit board; its power dissipation was set by controlling the current flow via an Adaptive Power Systems DDP25-200 power supply. Thermal cycles were applied by dissipating 300 W for between two and three hours, then allowing the system to cool down to room temperature. Two cycles were applied within 24 hours of each other. The system was then left at room temperature and sub-atmospheric pressure for two weeks, after which two further cycles were conducted within 24 hours. Pressure was recorded throughout the thermal cycling test by a Bourns BPS130 absolute pressure sensor; the measurements are shown in Fig 5.10. After the first two thermal cycles, pressure reached a steady state value of 70.2 kPa. After the final cycle, the steady state pressure value was 63.4 kPa; the reduction was attributed to variation in ambient conditions such as temperature in the laboratory. It is clear the rate of air leakage and contaminant outgassing during the two week period is sufficiently small that it can not be distinguished from other contributing factors. This indicates that, on short time scales at least, the proposed two-phase immersion cooling system is unaffected by non-condensible gases. Longer term testing is required to draw conclusions about performance over the lifetime of a power converter.

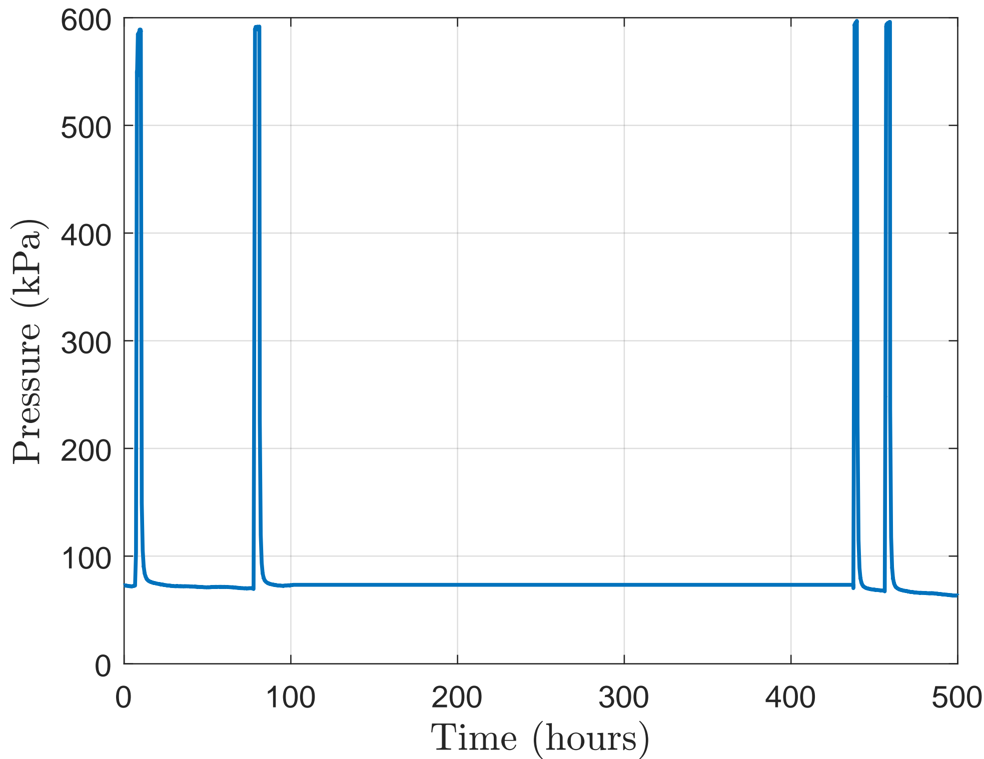

Figure 5.10: Pressure measurements taken over a period of two weeks with four thermal cycles applied.

5.4 Conclusions

In this chapter, a practical two-phase immersion cooling system was proposed for an electric vehicle motor drive on PCB substrate. The following key observations were made concerning the performance of such systems.

- Condensation heat transfer on downward facing fins is accurately predicted at high power using theoretical models based on conduction through the liquid film. For heat exchangers with a finned condenser side and water channels on the flow side as shown in Fig. 1.3, heat exchanger performance index of 167 W/(L K) was demonstrated.

- When considering the whole converter, the cooling system performance index achieved is 30 W/(L K). This is competitive with the best previous efforts detailed in literature while offering the unique advantage of cooling the entire converter rather than just semiconductor switches.

- Preliminary experiments with a two-phase immersion apparatus using O-rings and bonded seals indicates that air leakage and contaminant outgassing have negligible impact on performance over one month timescales.

6
Power Density of Two-Phase Immersion Cooled Magnetic Components

Another important class of components for power electronic systems is magnetics. These consist of one or more coils of electrical conductor wound on a magnetic core. Conventional cooling approaches rely on natural or forced flows of air around the coils and core. High power transformers may be immersed in tanks of mineral oil such that heat is transferred by single phase liquid convection. The aim of this chapter is to explore the potential for increased volumetric power density of magnetic components by applying two-phase immersion cooling with Novec 7000 dielectric fluid. It is anticipated improved surface heat transfer can facilitate operation of a given magnetic component at higher currents, voltages and powers. Table 6.1 summarises the heat transfer coefficients which can be achieved by air and oil cooling based on previous literature. For comparison, the highest recorded heat transfer coefficient for boiling Novec 7000 from Chapter 3 is $1.5\,\mathrm{W/(cm^2\,K)}$.

Magnetic components suffer two main loss mechanisms associated with the wire coils and magnetic core respectively. Wire losses are generated by Joule heating associated with resistance to current flow. The first contribution of this chapter is a theoretical model and subsequent experimental validation of the current at which a two-phase immersion cooled wire will fail due to Joule heating. For pure copper

Table 6.1: Heat transfer coefficients for different magnetic component cooling techniques. These are selected based on values proposed in the respective reference.

Cooling approach	**Heat transfer coefficient** ($W/(cm^2\,K)$)	**Reference**
Natural convection in air	0.0005	[78]
Forced air cooling	0.005	[79]
Mineral oil with aluminium oxide nanoparticles	0.05	[80]
Boiling heat transfer with Novec 7000	1.5	Chapter. 3

wire, this limit arises from the incipience of critical heat flux on the wire surface. Experiments are also conducted with Litz wire, which consists of many individually insulated copper strands. An alternative failure mechanism is identified whereby the insulation material melts, fusing strands together and effectively short circuiting them. This limits the current carrying capacity for Litz wire relative to bare copper wires of comparable diameter. Expected improvements compared with air and oil cooling are quantified for both types of wire.

In magnetic cores excited by periodic alternating voltages, power losses are dependent on the maximum magnetic flux density which in turn depends on the magnitude and frequency of the voltage excitation. By applying two-phase immersion cooling, power losses for a toroidal ferrite magnetic core are characterised at frequencies up to 1.6 MHz and flux densities approaching saturation of the core. This is a wider range of operating conditions than is typically provided by core material data-sheets and is facilitated by improved heat transfer from the core surface. A thermal model of the chosen core is proposed and used to evaluate the maximum flux density as a function of frequency for two-phase immersion, oil and air cooling. In a final step, the experimental results and models developed are employed to design transformers in air, oil and Novec 7000 in order to compare their volumes.

6.1 Coil Current Limits

When alternating current with frequency f flows in a conductor, the current density is highest near the surface and decreases towards the centre. Skin depth δ_e, expressed in Equation 6.1, provides a measure of how far current penetrates into a conductor with electrical resistivity ρ_e and magnetic permeability μ_m [81].

$$\delta_e = \sqrt{\frac{\rho_e}{\pi f \mu_m}} \tag{6.1}$$

If the diameter of a wire coil is less than twice the skin depth, the skin effect can be neglected; the coil resistance and losses are approximately the same as for a direct current [81]. Fig. 6.1 plots the largest frequency for which this condition is satisfied for copper wire at 65 °C. The maximum frequency for a 1 mm diameter wire is 20 kHz. This was selected as a practical lower bound on the switching frequency so larger diameter wires were not considered.

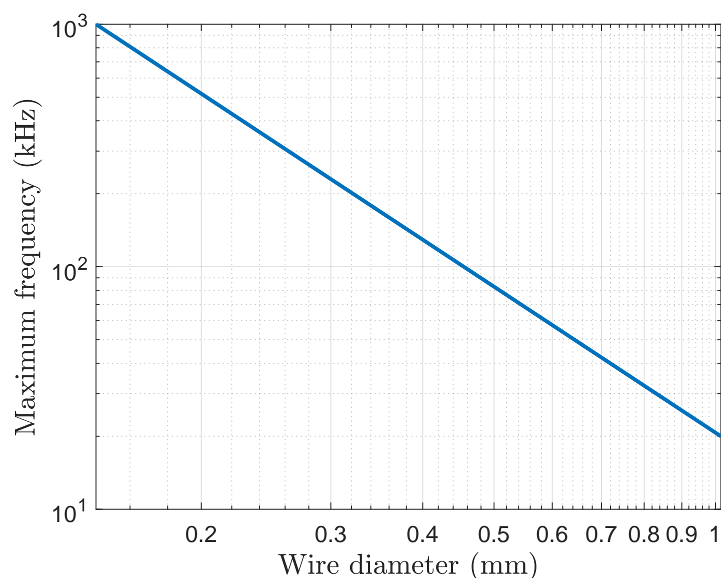

Figure 6.1: Maximum frequency for copper wire coils of varying diameter based on skin effect.

6.1.1 Bare Copper Windings

A wire coil can be modelled as a thermally conductive cylinder with diameter d_{w} and material thermal conductivity k_{w}. The coil rejects heat from its surface to a surrounding medium at temperature T_{s}, at a rate characterised by the heat transfer coefficient h. The Biot number for the wire is defined in Equation 6.2 [14]. If the material is copper with thermal conductivity 390 W/(m K) and the surface heat transfer coefficient is 1.5 W/(cm^2 K)the worst case Biot number is 0.04 for a 1 mm diameter wire. This value indicates the temperature can be considered uniform across the cross section and is everywhere equal to the surface temperature T_{c}.

$$Bi = \frac{hd_{\mathrm{w}}}{k_{\mathrm{w}}} \tag{6.2}$$

When current I passes through a coil, it will heat up to the temperature at which the Joule heating power losses are equal to the heat transferred from surface to surroundings. This condition can be expressed per unit length of wire by Equation 6.3.

$$\frac{4\rho_{\mathrm{e}}}{\pi d_{\mathrm{w}}^2} I^2 = h\pi d_{\mathrm{w}}(T_{\mathrm{c}} - T_{\mathrm{s}}) \tag{6.3}$$

Copper exhibits an increase in electrical resistivity with temperature as indicated by the positive value of the temperature coefficient α in Equation 6.4 [82].

$$\frac{\mathrm{d}\rho_{\mathrm{e}}}{\mathrm{d}T} = \alpha\rho_{\mathrm{e}} \tag{6.4}$$

For sufficiently high currents, thermal runaway can occur whereby the temperature increases rapidly until the wire melts. This is illustrated in Fig. 6.2 which plots the per-length power loss and surface heat transfer (the right and left hand sides of Equation 6.3) as functions of wire temperature for three different currents. For the smallest current of 15 A there are two intersections, defining two potential thermal equilibria which are labelled according to their stability. The highest theoretical current, 26 A, is that for which only one (unstable) equilibrium occurs. For yet higher currents, the lines do not intersect; the surface heat transfer is everywhere smaller than the power loss and the wire temperature will increase until it melts.

This mechanism imposes a limit on the current carrying capacity of coils. These limits are plotted in Fig. 6.4 for the heat transfer coefficients detailed in Table 6.1 and surrounding temperature of 65 °C.

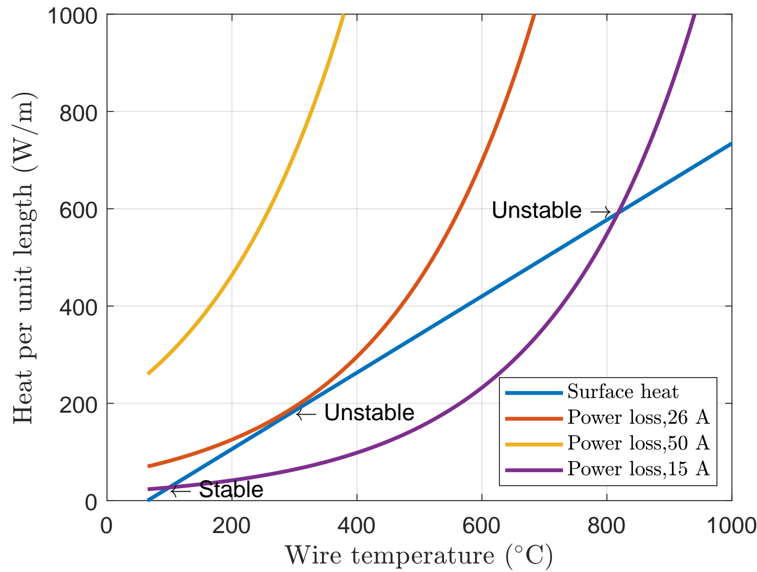

Figure 6.2: Per length values of power loss and surface heat transfer as a function of wire temperature at different currents.

For two-phase immersion cooled coils, it is important to also consider the critical heat flux. For small horizontally oriented cylinders, a model has been proposed in literature based on a modification to the Zuber instability theory; it is expressed by Equation 6.5 [72]. This model predicts a decrease in critical heat flux with wire diameter as shown in Fig. 6.3.

$$q_{\mathrm{chf}} = 0.94 \left(\frac{d_{\mathrm{w}}}{2\sqrt{\frac{\sigma_{\mathrm{l}}}{g(\rho_{\mathrm{l}}-\rho_{\mathrm{v}})}}} \right)^{-\frac{1}{4}} q_{\mathrm{zub}} \tag{6.5}$$

Equating the power losses and surface heat transfer at critical heat flux yields Equation 6.6 for the maximum coil current. For simplicity, the electrical resistivity is evaluated at the temperature T_{s} of the surrounding fluid plus 35 °C. Fig. 6.4 demonstrates the critical heat flux current limit for wire coils immersed in Novec 7000 fluid with saturation temperature of 65 °C. It is apparent these currents are lower than the thermal runaway limits evaluated with a heat transfer coefficient

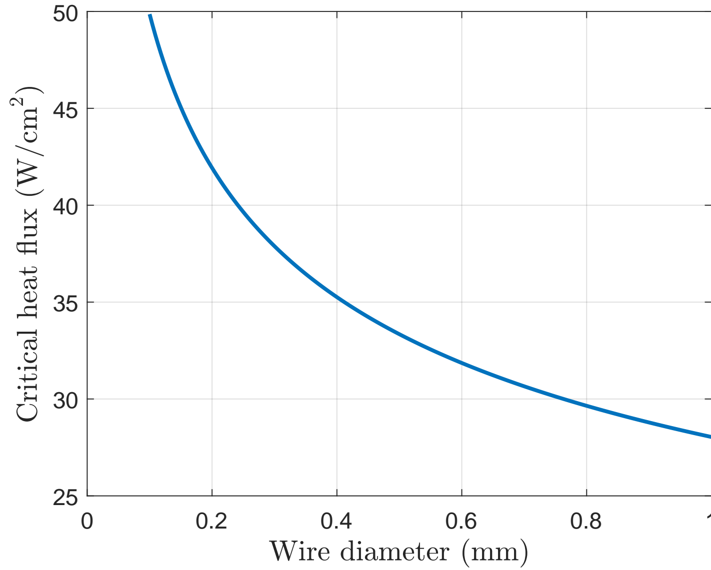

Figure 6.3: Critical heat flux for a small horizontal wire as a function of its diameter according to the Zuber model of Equation 6.5.

of 1.5 W/(cm^2 K) so critical heat flux is the mechanism by which the wire will fail. Nevertheless, the failure currents are up to three times greater than for oil and almost eight times larger than with forced air.

$$I = \sqrt{\frac{\pi^2 d_{\mathrm{w}}^3 q_{\mathrm{chf}}}{4\rho_{\mathrm{e}}}} \tag{6.6}$$

To validate the predicted critical heat flux current limits for two-phase immersion cooled coils, a modified version of the experimental apparatus from Chapter 3 was built, depicted in Fig. 6.5. The borosilicate chamber, heat exchanger and O-ring sealing arrangement remain unchanged; the insulated aluminium heater block is replaced with a solid PEEK block. To pass electrical current through the component under test, two M4 threaded brass studs are inserted into the block. A bonded seal is secured to either side of the PEEK by a nut to prevent leakage of fluid. A power supply is connected to the exposed portion of the stud external to the chamber. The apparatus can be applied to any two-terminal component, including wire segments or inductors wound on a magnetic core, by connecting each end to the corresponding stud internal to the chamber. Prior to each test, the apparatus

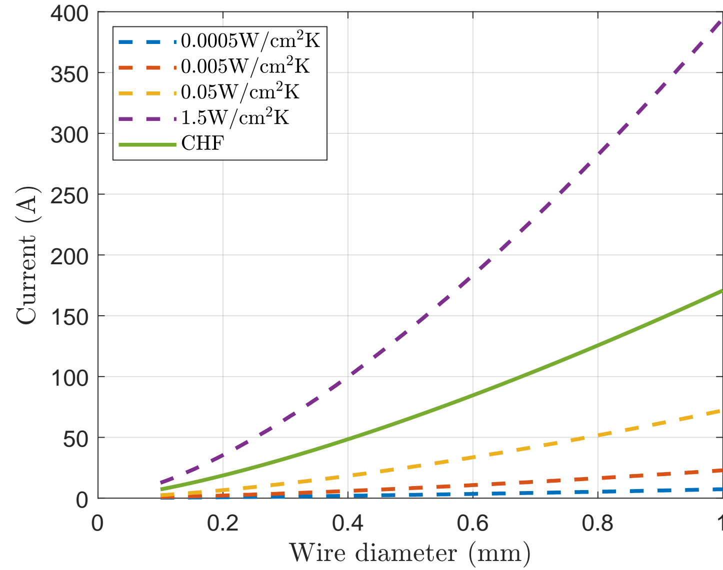

Figure 6.4: Current limits based on thermal runaway and critical heat flux as a function of wire diameter.

is filled with Novec 7000 and evacuated of air as outlined in Chapter 3.

20 cm lengths of coiled bare copper wire with varying diameters were tested by applying a direct current increased incrementally until critical heat flux was observed. The current flow is set by an Adaptive Power Systems DDP25-200 power supply connected to the apparatus via power leads. Separate sense leads are attached to the external brass stud immediately after the sealing nut and fed back to the supply, providing wire voltage measurements which do not include the resistive voltage drop due to current flow in the power leads. Measured voltages facilitate estimation of the power dissipation and critical heat flux. Importantly, they are also used to identify the incipience of critical heat flux, which is accompanied by a sudden increase in wire resistance and voltage. By setting appropriate protection limits on the power supply, the test could be terminated automatically after critical heat flux without causing the wire to burn out.

Table 6.2 summarises theoretical and experimental critical heat fluxes and currents for wires of diameter 0.315 mm, 0.4 mm and 0.5 mm. The theoretical values are evaluated at the fluid saturation temperature calculated from the corresponding pressure measurement. In the absence of accurate wire temperature measurements,

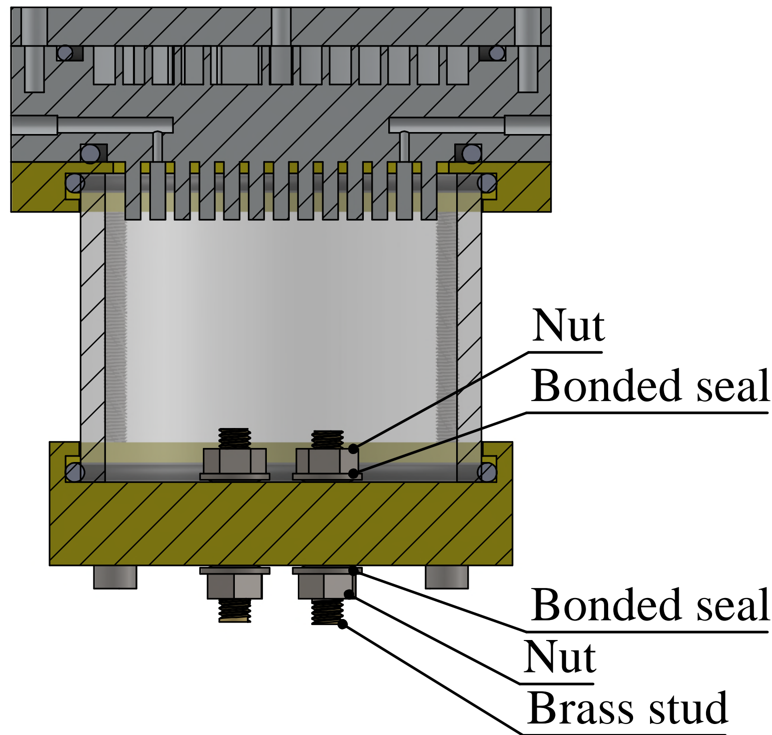

Figure 6.5: Experimental apparatus used for testing of magnetic components.

it is assumed to be 35 °C hotter than the fluid saturation temperature when evaluating the electrical resistivity for Equation 6.6. This value was chosen based on experimental observations from Chapter 3. The experimentally measured currents are smaller than the predictions by between 2 % and 4 %. This is due to the overestimation of critical heat flux by the model. A possible explanation for this discrepancy relates to orientation of the cylindrical surface when coiled. It is reported in previous literature that critical heat flux on planar surfaces decreases as the orientation varies from zero to 90°, so certain portions of the wire may be more susceptible to critical heat flux than a horizontal cylinder [83].

6.1.2 Litz Wire Windings

For high frequency magnetic components, Litz wire is employed in order to mitigate the skin effect. It is made up of many individually insulated wire strands, each smaller than the skin depth, bundled and twisted together. A Litz wire will exhibit lower current carrying capacity than a pure copper wire of the same diameter

Table 6.2: Calculated and experimentally determined values of critical heat flux and failure current for different wire diameters.

Diameter (mm)	0.315	0.4	0.5
Theoretical CHF (W/cm^2)	40.9	39.2	37.6
Experimental CHF (W/cm^2)	37.5	37.0	36.4
Theoretical current (A)	35.8	49.9	68.0
Experimental current (A)	35	48	65

for several reasons. Firstly, the copper fill factor is reduced which increases the resistance per unit length. Furthermore, the insulation material can introduce significant thermal resistance to heat flow through the cross section. According to prior literature, if Litz wire is considered a homogenous porous material, its effective thermal conductivity is only 1 W/(m K) to 2 W/(m K) compared with 390 W/(m K) for pure copper [84].

At 1 MHz, Litz wire manufacturers recommend use of 46 American Wire Gauge (AWG) strands with diameter 0.04 mm. A Litz wire with 300 46 AWG strands was selected for experimental characterisation to determine the current carrying capacity with two-phase immersion cooling. It is a type 2 Litz wire, meaning the strands are divided up and twisted together to form bundles. The wire diameter was measured with a calliper as 0.96 mm. The insulation material has a melting temperature of 155 °C. In a preliminary test, it is observed the coil stiffens after passing a sufficiently high direct current. Inspection of the cross section indicates the insulation has melted and fused adjacent strands together. Fig. 6.6c depicts a fully fused section of wire after testing at 90 A. This can cause short circuits between strands and an accompanying large increase in AC electrical resistance due to skin effect. Consequently, the highest practical current is that just insufficient to melt the insulation.

Further testing was conducted by finding two currents which bracket the maximum current, one which causes strands to fuse and one which does not.

By testing the midpoint between these currents, the search space can be halved with each test. This is a time consuming process which requires disassembly of the experimental apparatus after each test to check the wire. Thus, the maximum current reported may not be exact but is deemed sufficiently close to the actual value.

Fig. 6.6a shows the wire after testing with 62 A. All of the strands could be separated from each other and there was no indication the insulation had melted. At 73 A, as shown by Fig. 6.6b strands within the same bundle were observed to have fused though the bundles could be separated from each other. This was selected as the current which is just sufficient to cause failure.

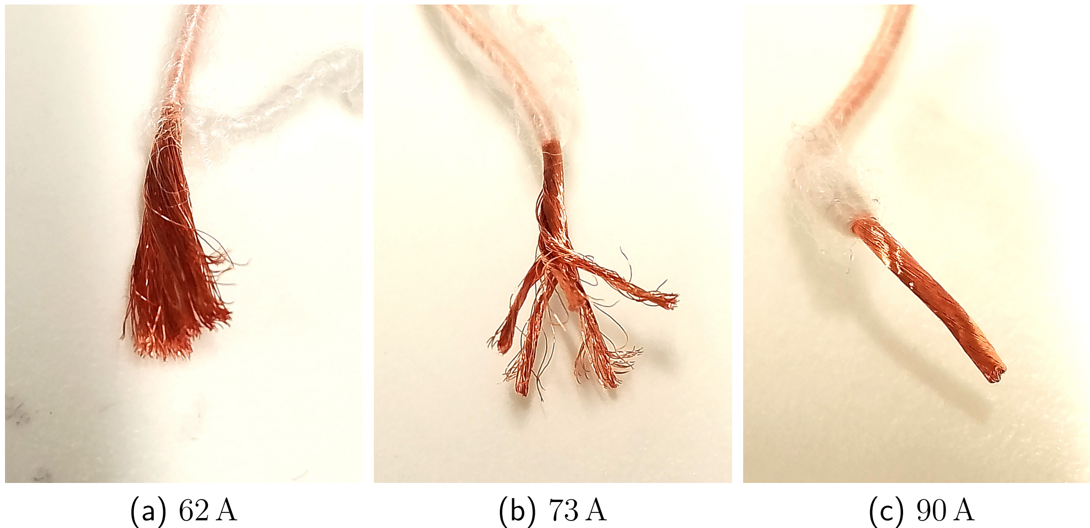

(a) 62 A (b) 73 A (c) 90 A

Figure 6.6: Pictures showing different degrees of strand fusing for 300/46 Litz wire tested at three different current values.

Theoretical predictions for oil and air cooled coils are calculated to compare with the experimental result. Assuming the chosen Litz wire is homogenous with thermal conductivity of 2 W/(m K) the Biot number with oil cooling is 0.24. This is deemed sufficiently low to assume uniform temperature throughout the cross section and the model is analogous to that for bare copper discussed previously. For a Litz wire with N_{st} strands each with diameter d_{st}, Equation 6.3 can be modified to yield the expression for current below. The failure values are found by evaluating

Table 6.3: Failure currents for 300/46 Litz wire cooled by air, oil and Novec 7000.

	Forced air	**Oil**	**Novec 7000**
Current (A)	12.5	39.6	73.0
Derived from	Equation 6.7	Equation 6.7	Experiment

Equation 6.7 with a wire temperature of 155 °C and are summarised in Table 6.3.

$$I = \sqrt{\frac{N_{\mathrm{st}}\pi^2 d_{\mathrm{w}} d_{\mathrm{st}}^2 h(T_{\mathrm{c}} - T_{\mathrm{s}})}{4\rho_{\mathrm{e}}}} \tag{6.7}$$

Two-phase immersion cooled Litz wire can sustain currents which are almost double those for oil and 6 times greater than forced air. It is noteworthy that Equation 6.7 predicts a failure current of 216 A for a heat transfer coefficient of 1.5 W/(cm^2 K) representing boiling in Novec 7000. The fact that only 73 A was achieved indicates conduction through the cross section becomes significant.

6.2 Magnetic Cores

When a periodic voltage waveform is applied to a coil wound on a magnetic core, a periodic flux is induced in the core with peak value proportional to the voltage magnitude. It is beneficial to operate magnetic components at high peak flux densities as this facilitates reduction of the core size for the same voltage. However, magnetic saturation places a limit on the maximum flux density; this is a property of the core material and is independent of its geometry. A second limit arises due to the dependence of magnetic core power losses on the peak flux density. For sufficiently high flux densities, sections of the core may heat up beyond the Curie temperature of the material. Once this occurs, magnetic permeability drops rapidly to zero and the component no longer functions as designed. This limit depends both on the material and core geometry. Table6.4 summarises dimensions and material properties for the 5977001401 toroidal ferrite core from Fair-rite which was selected for characterisation of flux density limits.

Table 6.4: Material properties and dimensions of the Fair-rite 5977001401 magnetic core.

Property	**Value** [85]
Core outer diameter (mm)	25.40
Core inner diameter (mm)	15.50
Core height (mm)	8.15
Saturation flux density at 100 °C (T)	0.4
Curie temperature (°C)	215
Thermal conductivity (W/(m K))	0.45

6.2.1 Curie Temperature Thermal Model

Although the chosen core has a rectangular cross section, it is modelled as a cylinder with thermal conductivity k_{cr} and diameter d_{cr} chosen to conserve the perimeter-to-cross section ratio for simplicity. The Biot number, evaluated via Equation. 6.2 with heat transfer coefficient of 1.5 W/(cm^2 K) is 150. This indicates conduction through the core can not be neglected and temperature T varies throughout the cross section with radial distance r from the core centre. The heat equation can be expressed in terms of the volumetric power dissipation Q''' which is assumed to be generated uniformly throughout the core [14].

$$\frac{1}{r}\frac{\mathrm{d}}{\mathrm{d}r}\left(rk_{\mathrm{cr}}\frac{\mathrm{d}T}{\mathrm{d}r}\right) = -Q''' \tag{6.8}$$

Equation 6.8 can be solved analytically subject to a boundary condition which sets a heat transfer coefficient h on the core surface. By equating the highest temperature, found at the core centre $r = 0$, to the Curie temperature T_{cr}, the following expression is obtained. It can be used to calculate the maximum volumetric power loss. A full derivation of the solution is presented in Appendix B.

$$T_{\mathrm{cr}} = T_{\mathrm{s}} + \frac{Q''' d_{\mathrm{cr}}^2}{16k_{\mathrm{cr}}} + \frac{Q''' d_{\mathrm{cr}}}{4h} \tag{6.9}$$

If instead the boundary condition is a constant critical heat flux q_{chf}, the following relation exists between the volumetric power loss and the heat flux.

$$Q''' = \frac{4q_{\mathrm{chf}}}{d_{\mathrm{cr}}} \tag{6.10}$$

Fig. 6.7a shows the Curie temperature limit on volumetric power loss for the chosen core with surface heat transfer coefficients up to 1.5 W/(cm^2 K). The surrounding medium is taken to be at 65 °C. It is observed the volumetric power loss tends towards a maximum value which is independent of further increase in heat transfer coefficient. This can be explained by considering Fig. 6.7b, which plots the temperature increase from fluid to core surface and from core surface to centre at the Curie temperature power dissipation limit. As the heat transfer coefficient increases, the total temperature rise at the core centre becomes dominated by the component from surface to centre which depends only on the material thermal conductivity and the core geometry.

Also shown is the volumetric power loss corresponding to critical heat flux in Novec 7000 evaluated using the Zuber model of Equation 3.10. It is clear that the Curie temperature will always be reached at the centre well before the power loss is sufficient to incipit critical heat flux on the surface.

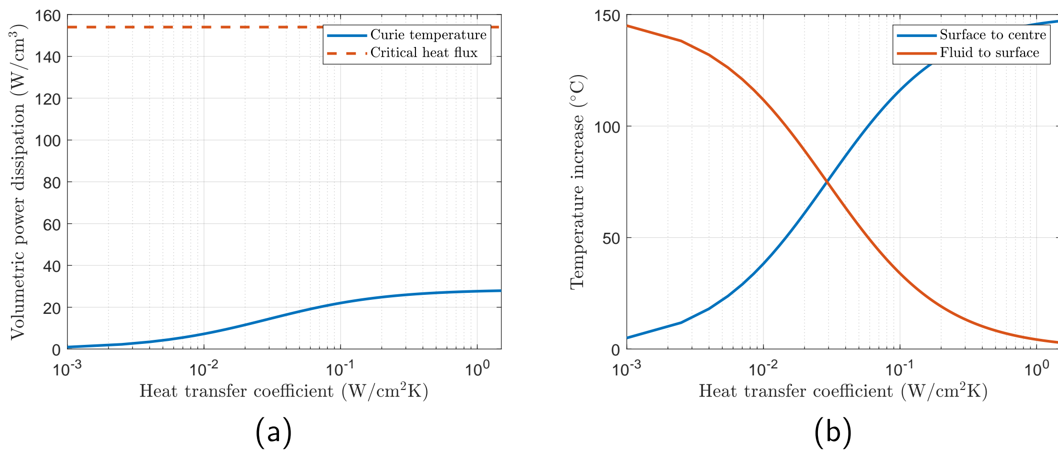

Figure 6.7: (a) Power dissipation limits imposed on the chosen magnetic core by Curie temperature and critical heat flux. (b)Temperature difference from fluid to core surface and from core surface to centre at the Curie temperature limit.

6.2.2 Magnetic Core Experiments

The Steinmetz equation is commonly used to evaluate the losses in a magnetic core excited by a sinusoidal flux. It is an empirical relationship which expresses the

per volume power loss in terms of the peak flux density ΔB and the excitation frequency f. It incorporates empirical parameters c, a and b which are derived from experimental data [86].

$$Q''' = cf^a \Delta B^b \tag{6.11}$$

In order to relate the Curie temperature power loss limit to the flux density via Equation 6.11, it is necessary to derive values for the Steinmetz parameters. While the core manufacturer provides some loss data, it is limited to frequencies below 400 kHz and flux densities below 0.2 T. By making use of improved two-phase immersion cooling, the selected core is tested up until magnetic saturation or Curie temperature limit for frequencies up to 1.6 MHz. An inductor comprised of three Litz wire turns with 300 strands of 46 AWG was wound on the selected core and enclosed within the test chamber of Figure. 6.5. DC voltage is set by an EA-PSI 8720-15 power supply and converted into a square wave with magnitude V by a full bridge converter controlled via a field programmable gate array (FPGA) platform previously developed within the Power Electronics Group. Frequency f of the square wave voltage is varied by changing the converter switching frequency via the FPGA. The square wave voltage excitation produces a triangular flux waveform whose peak depends on the number of winding turns N_{w} and the core cross-sectional area A_{cr}.

$$\Delta B = \frac{V}{4fN_{\mathrm{w}}A_{\mathrm{cr}}} \tag{6.12}$$

By varying the power supply voltage in increments up to the converter rated value of 150 V, the flux density is set via Equation 6.12. For each combination of frequency and flux density, the total power dissipation is calculated from the DC voltage and current provided by the power supply, which were measured with Keithley DMM6500 multimeters. Implicit in this approach is the assumption that all input power is dissipated in the core i.e. the power loss in the Litz wire, converter and connecting cables are negligible. This assumption is justified by the fact that current magnitudes, and thus Joule heating losses, are small.

The current waveform is continuously monitored via a current clamp connected

to an oscilloscope. Under normal operation of the inductor, current waveforms are observed to be triangular. As the flux density increases, deformation to the current waveform shape occurs, indicating the inductor no longer works as expected either due to core saturation or parts of the core reaching the Curie temperature. When this is observed for a particular frequency, the test is ended and higher voltages are not applied. It should also be noted that at 1.6 MHz, current deformation was not observed; rather, the test was halted due to overheating of the semiconductor switches in the converter.

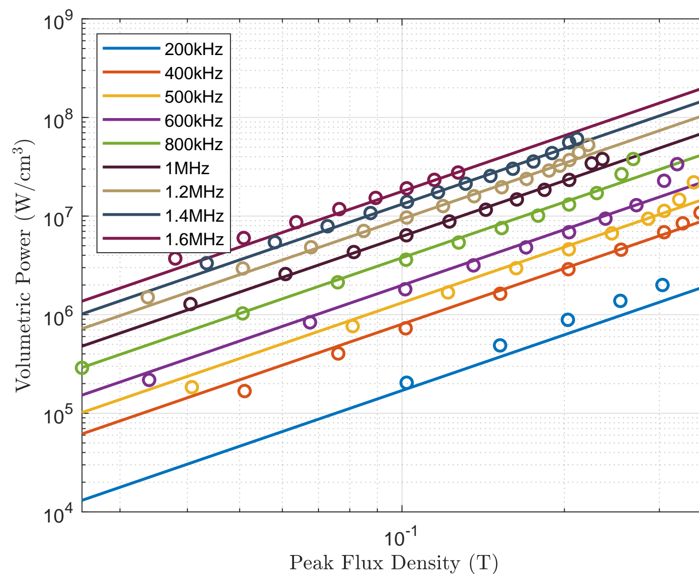

Figure 6.8: Measured volumetric power dissipations for different flux densities and excitation frequencies (shown as dots). Steinmetz equation fits are also shown as straight lines.

Fig. 6.8 shows the measured volumetric power loss as a function of flux density and frequency. The Steinmetz parameters were computed as $a = 2.2360$, $b = 1.8766$ and $c = 1.7962 \times 10^{-5}$ by multivariable regression. Power dissipations computed via the fitted Steinmetz equation are also displayed.

By combining the thermal model with the fitted Steinmetz equation, it is possible to estimate the maximum flux density as a function of frequency. This is shown in Fig. 6.9 for frequencies up to 2 MHz for each of the cooling methods from Table 6.1. For low frequencies, core saturation rather than Curie temperature imposes a limit

on flux density, accounting for the flat portion of each line. At higher frequencies, Curie temperature is reached before saturation and a decrease in flux density with increasing frequency is observed. The model predicts a two-phase immersion cooled winding can operate at flux densities 1.3 times greater than in oil and 2.8 times greater than in air.

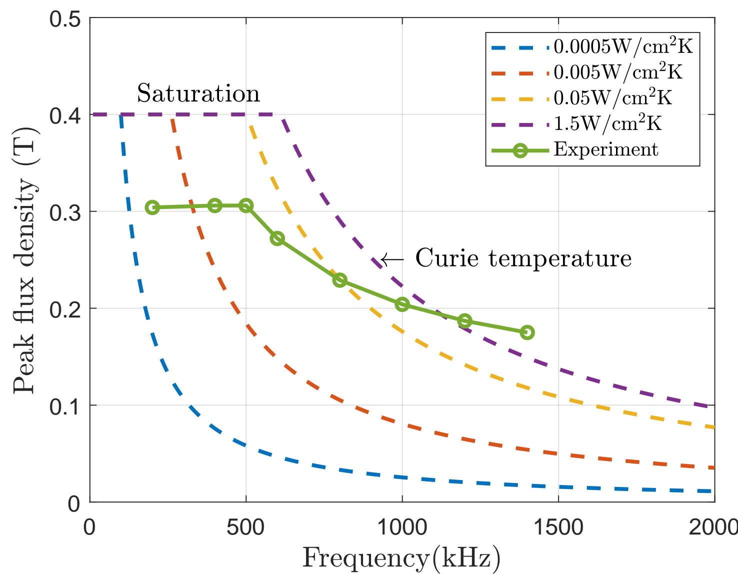

Figure 6.9: Predicted peak flux density as a function of frequency for different heat transfer coefficients at the core surface. Experimentally measured values for the core immersed in Novec 7000 are also displayed.

The figure also includes the experimentally measured flux densities beyond which current deformation was observed. These values follow a similar trend as the theoretical predictions. For frequencies up to 500 kHz, saturation occurs at a flux density of 0.3 T. This is smaller than the data sheet value provided at 100 °C and likely reflects a reduction in saturation flux density with core temperature. For 600 kHz and up, the maximum flux density decreases with frequency, indicating the Curie temperature is the limiting factor.

6.3 Transformer Power Density

In order to quantify the improvements in power density facilitated by two-phase immersion cooling, a sizing approach is developed to estimate the volume of a

transformer cooled via forced air, oil and boiling Novec 7000. The target application is an isolated DC-DC converter in an electrical vehicle. The voltage excitation magnitude is set to 800 V as this is an increasingly common choice for battery pack voltage. The excitation frequency is 1 MHz. The load current is selected as 73 A. The transformer consists of primary and secondary Litz wire coils each with twelve turns; it has unity turns ratio. The magnetic core is toroidal with circular cross section and made from Fair-rite material 77.

For the two-phase immersion cooled transformer, 300/46 Litz wire can conduct the full load current. For oil and air, AWG Litz wires with 300, 330, 420, 550, 660 and 1000 strands of 46 AWG were considered. For each, the number of wires which must be connected in parallel to conduct the load current is determined. The toroidal core inner diameter is sized to accommodate both coils with 0.6 mm spacing between adjacent turns to prevent vapour coalescence. Finally, the core cross section diameter must be selected to avoid saturation or Curie temperature limits.

6.3.1 Core Sizing

To determine core cross section diameter, it is useful to consider how it effects the magnetic flux. Increasing the diameter will decrease the flux density for the same voltage excitation via Equation 6.12. However, it will also reduce the volumetric power loss (and hence peak flux density) at which the Curie temperature is reached at the centre. By combining Equations 6.12,6.9 and 6.11, the following expression can be derived.

$$\frac{d_{\mathrm{cr}}^{2b}}{\frac{d_{\mathrm{cr}}^{2}}{16k_{\mathrm{cr}}}+\frac{d_{\mathrm{cr}}}{4h}}=\left(\frac{V}{N_{\mathrm{w}}\pi}\right)^{b}\frac{cf^{a-b}}{T_{\mathrm{cr}}-T_{\mathrm{s}}} \tag{6.13}$$

It can be shown the left hand side of Equation 6.13 is a monotonically increasing function of core diameter and the smallest allowable core diameter is that for which the Curie temperature is just reached at the centre. This is found by solving Equation 6.13 iteratively using Newton's method for the corresponding heat transfer coefficient from Table 6.1. More detail concerning the solution procedure is presented in Appendix C.

Table 6.5: Design parameters and calculated volume for transformers cooled in air, oil and boiling Novec 7000.

	Air	**Oil**	**Novec 7000**
Number of Litz strands	1000	660	300
Number of parallel wires	2	1	1
Diameter of Litz wire (mm)	2.29	1.65	0.96
Core inner diameter (mm)	45.2	18.0	12.4
Core cross section (mm)	26.6	18.1	16.4
Transformer volume (cm^3)	221.8	47.1	28.6

Table 6.5 summarises chosen parameters for the three transformers. For each, the volume is estimated by a cylindrical envelope which encloses the core and windings. The results indicate that two-phase immersion cooling can reduce the transformer volume by a factor of 1.6 compared with oil and 8 compared with air. The three transformers are depicted graphically in Fig. 6.10.

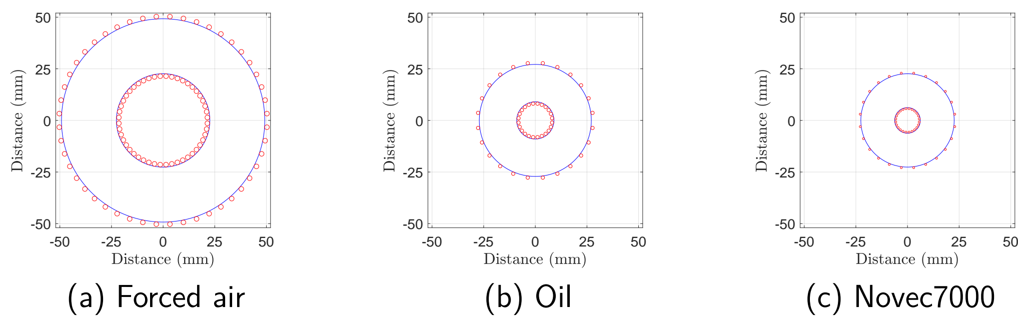

Figure 6.10: Plots showing dimensions of transformers cooled in air, oil and Novec 7000.

6.4 Conclusions

The experiments detailed in this chapter provide important insights into the performance of magnetic components cooled by two-phase immersion.

- For bare copper wires immersed in Novec 7000, the current capacity is limited by the occurrence of critical heat flux on the surface. These currents are predicted to be three times greater than oil and eight times greater than air. For enamelled Litz wire, failure occurs by melting of the insulation and subsequent fusing of strands. This mechanism was found to substantially reduce the maximum current compared with bare copper wire of the same diameter.

- Immersion of a ferrite core in Novec 7000 enabled loss characterisation up to the saturation flux density and for frequencies in excess of 1 MHz, which is typically not possible when testing cores in air. Thermal modelling indicates the temperature difference across the core cross section is significant and the volumetric power dissipation is limited by occurrence of the Curie temperature at the core centre.

- Improved surface heat transfer offered by two-phase immersion cooling facilitates reduction of transformer volume by a up to 8 times compared with air.

7
Discussion and Future Work

Throughout this thesis, theoretical analysis of boiling and condensation phenomena, along with experiments, were applied to provide answers for the research questions posed in Chapter 1. Based on the results, several important conclusions can be drawn concerning application of two-phase immersion cooling to enable power dense converters on PCB substrates. These conclusions are discussed in this chapter and avenues for future research within the topic of two-phase immersion cooling are also proposed.

7.1 Conclusions

1. **Identifying the limits of boiling heat transfer performance for planar horizontal switches in closed systems**. Experimental results support the hypothesis that boiling heat transfer in dielectric fluids improves with elevated saturation temperatures and pressures occurring in closed systems. For a practical electric vehicle motor drive with water-glycol temperature of 65 °C, critical heat flux of 43 W/cm^2 and a heat transfer coefficient of 1.5 W K/cm^2 can be expected with Novec 7000 dielectric fluid, compared with 20 W/cm^2 and 0.85 W K/cm^2 at atmospheric pressure [24].

   It is observed that the Zuber model based on hydrodynamic stability theory

predicts the experimental critical heat flux to within 13 %. Boiling correlations proposed by Stephan, Mostinski and Cooper failed to match experimental results up to the critical heat flux. The Rohsenow correlation with fitted parameters C_{sf} and n reasonably agrees with experiment to a mean absolute percentage error of 12 %.

2. **Exploring improvements in boiling heat transfer for semiconductor switches with finned heat spreaders on PCB substrates**. A one-dimensional model for heat flow through pin fins subject to a temperature-dependent heat transfer coefficient was proposed. Through numerical solution, the model can be applied to predict performance of heat spreader designs subject to constraints imposed by the PCB substrate. By modelling the heat transfer coefficient with a piecewise Rohsenow correlation fitted to experimental data , switch-level heat transfer coefficient predictions can be obtained which match experimental values with a mean absolute percentage error of 12 %.

   Experiments with Novec 7000 indicate finned heat spreaders can improve the switch-level heat transfer coefficient from $1.5\,\mathrm{W\,K/cm^2}$ to $2.5\,\mathrm{W\,K/cm^2}$. This was increased further to $3.4\,\mathrm{W\,K/cm^2}$ by grit blasting the fin surfaces to favourably influence micro-geometry. This performance was achieved with simple machining and surface treatment techniques using a heat spreader geometry that neither compromises converter electrical layout nor requires an increase in total volume.

3. **Design and evaluation of a complete sealed two-phase immersion cooling system targeting high thermal power density**. A heat exchanger design for two-phase immersion cooling was presented. It features downward facing pin fins on the condenser side, water-glycol coolant channels on the flow side and a separating material layer in between. This allows the condenser side fins and the flow side channels to be configured independently of each other. The flow side channels can be sized using conventional design paradigms

to achieve high convective heat transfer with acceptable pressure drop. A theoretical model for film condensation on downward facing fins was presented and solved numerically. This allows for simulation aided design of the condenser side geometry. Experimental results indicate the heat exchanger can achieve HEPI of 167 W/(L K). It approaches the performance of commercial liquid cooled heat exchangers with the additional advantage of integration into the fluid chamber and can be constructed using simple CNC manufacturing techniques.

Based on the proposed heat exchanger, an electric vehicle motor drive inverter on PCB substrate was designed and evaluated in terms of thermal power density metrics. The converter achieves CSPI of 30 W/(L K) which is competitive with the best previous efforts in literature, while incorporating decoupling capacitors and gate drivers in close proximity to semiconductor switches. This performance indicates the potential of two-phase immersion cooling to enable power dense PCB-based converters with low inductance electrical layouts.

A sealing concept to enclose dielectric fluid between a chamber and the PCB substrate was proposed based on elastomer seals. Experiments were conducted over the course of a month to investigate the impact of non-condensible gases leaking into the system and contaminant outgassing. Results indicate performance of was unaffected after several thermal cycles. However, longer term tests are required to draw conclusions over the lifetime of a converter.

4. **Characterisation of the reduction in size of two-phase immersion cooled power magnetic components**. Experiments with bare copper wires immersed in Novec 7000 dielectric fluid indicate their current capacity is limited by the occurrence of critical heat flux at the surface. Maximal currents measured for different diameters of wire agree closely with predictions derived using Zuber's theory of critical heat flux. The values are three times greater than theoretical estimates for oil-cooled wires and almost eight times greater than with air-cooling. For Litz wires, sufficiently high currents cause the

insulation to melt which fuses strands together and increases AC resistance. This current was identified experimentally for a 300/46 Litz wire as 73 A, almost double the theoretical value for oil and six times greater than air.

Analysis of heat transfer through a magnetic core cross section demonstrates the volumetric power dissipation is restricted due to the core centre reaching the material Curie temperature. A limiting value on power dissipation occurs when conduction through the core alone causes this to occur. Immersing ferrite cores in Novec 7000 fluid significantly improves heat transfer from the surface and allows the core to operate close to the conduction limit. This enables characterisation of loss mechanisms in magnetic materials at higher flux densities than are typically provided in material data-sheets. Furthermore, it facilitates reduction in core size for the same voltage excitation and frequency. The combined effect of two-phase cooling both core and coils is to reduce the volume of air-cooled transformers and inductors by a factor of almost 8.

7.2 Future Work

Exploration of alternative heat transfer fluids for two-phase immersion cooling: Experiments conducted in Chapters 3 and 4 demonstrate that boiling heat transfer performance for dielectric fluids can be improved substantially by combining high fluid saturation temperature operation, finned heat spreaders and surface micro-geometry enhancement. In order to achieve yet higher switch-level heat transfer coefficients and critical heat fluxes, it is important to consider fluids with more favourable physical properties. This would additionally improve heat transfer associated with the heat exchanger condenser side. Further research would therefore seek to address issues which currently obstruct use of alternative fluids, including chemical compatibility for solvents like methanol and electrical conduction for water.

Preliminary investigations in the literature using ethanol demonstrate adequate chemical compatibility with semiconductor dies in short tests [32]. Furthermore, tests were conducted during the course of this DPhil involving immersion of a printed

circuit board in ethanol. These experiments were not discussed in the main body of the thesis. However, there were no clear indications of chemical damage to the PCB, semiconductor switches, passive components or silicone seals over the course of one week. With more time, long term testing would be conducted using various alcohols with a wider range of electronic components including transformer/inductor assemblies.

If alcohols prove to be feasible candidate fluids for electronics cooling, several further avenues of investigation follow. One example is the use of binary aqueous mixtures. In [87], small quantities of methanol or 2-propanol are mixed with water, yielding improvements in critical heat flux by factor of 1.6 and 2 respectively compared with pure water. This is explained by the reduction in surface tension of the mixture relative to pure water, reducing bubble size while retaining favourable bulk thermal properties. Future work in this area would consider the performance of mixtures with fluids other than water as the base liquid in order to address electrical conduction issues.

Novel heat exchangers to achieve greater power density: In Chapter 5, it is observed that when finned heat spreaders and surface enhancement techniques are used to enhance boiling heat transfer from the semiconductor switch surface, the heat exchanger condenser side accounts for the majority of thermal resistance from the flow side inlet to the switch. This is due to the separation between dielectric fluid and water glycol and the effect of conduction through the condenser side pin fins. In order to improve the achievable CSPI of two-phase immersion cooled systems, it is necessary to consider novel heat exchanger designs which reduce separation between the two fluids with minimal compromise on the surface area available for condensation and liquid convection. Preferably, these would also be machinable using conventional CNC milling techniques. A possible example is depicted in Fig. 7.1. It consists of alternating parallel channels separated by a folded layer of material. The dielectric fluid condenses in the downward facing channels and returns to the pool under gravity. Water-glycol flows through the upward facing channels

and the two are coupled thermally via a thin separating wall. The condensing

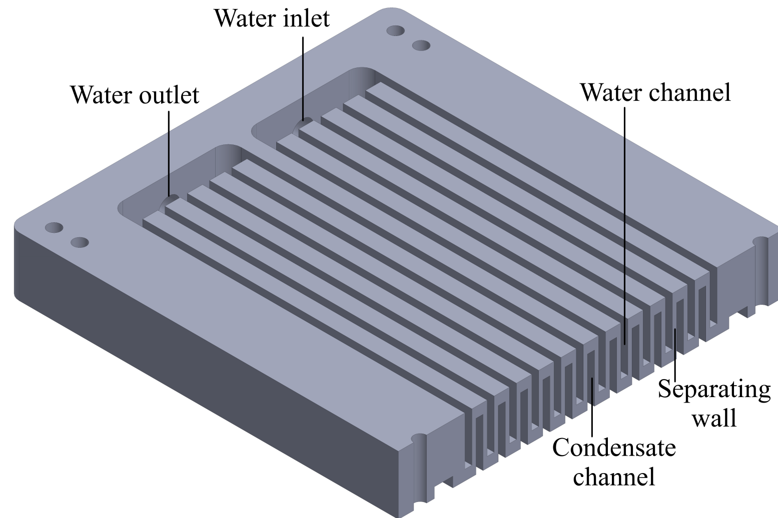

Figure 7.1: Diagram showing section view of alternative heat exchanger structure which minimises separation between dielectric fluid and water-glycol coolant.

surface geometry is now closely related to the flow side channel arrangement. Future research would focus on optimising such structures to achieve the best compromise between condensation and convective heat transfer while maintaining acceptable pressure drop across the flow side.

More drastic departures from the heat exchanger concept of this thesis could also be considered. In [88], it is proposed to condense dielectric fluid vapour by direct contact with water. Due to the high density of Novec 7000 fluid, it will stratify at the bottom of a mixture with water. Bubbles forming in the dielectric fluid layer rise and accumulate at the interface between the two liquids. When a sufficiently large bubble forms, it penetrates the interface, condenses in direct contact with surrounding water and returns to the Novec 7000 layer. This approach yields high condensation heat transfer coefficients and a large heat exchange area. Research would focus on addressing concerns surrounding the electrical isolation capability, particularly in non-static applications like electric vehicles, where mixing of the dielectric fluid and water may occur.

Practical implementation of two-phase immersion cooling in electric

vehicle applications: In Chapter 5, experiments were conducted which demonstrate a negligible impact of air leakage over the course of one month for fluid chambers sealed to PCB substrates via elastomer O-rings. Given more time, longer term thermal cycling tests would be conducted. The results could be extrapolated over the lifetime of a power converter to determine the feasibility of a sealed-for-life approach. Furthermore, development of techniques for in-situ detection and purging of non-condensible gases would be investigated. Such techniques work by periodically venting NCGs stratified on top of the vapour space, which is inevitably accompanied by loss of dielectric fluid [42]. In electric vehicle applications where volume is severely constrained, a feasible degassing approach must minimise the associated loss rate to reduce the excess fluid volume required to ensure components remain submerged over the converter lifetime.

Another challenge in electric vehicle applications which warrants further investigation relates to the impact of vehicle motion on two-phase immersion cooling performance. This work would consider methods to ensure all electronic components can remain submerged under changes in orientation. This could include incorporation of porous structures to induce capillary driven return of liquid from the condenser, as is commonly employed in heat pipes [14]. Alternative chamber designs could also be considered which allow for effective heat exchange from all surfaces rather than just one single surface which is located vertically above the electronic components. This could facilitate gravity-driven return of condensate in multiple different orientations.

Realisation of power dense, transformer isolated DC-DC converters: Further research would build on findings concerning magnetic components in Chapter 6 to demonstrate power dense DC-DC converters with transformers for galvanic isolation. This is useful in applications like on-board chargers for electric vehicles where volume minimisation is a key objective. An important component of this work relates to novel design procedures for two-phase immersion cooled transformers. Preliminary investigations in the literature tested chemical compatibility between dielectric fluids and materials used in conventional transformer assemblies. Ferrite

core, polyurethane enamelled wires, epoxy adhesives and polymer spacers/coil formers all demonstrated no observable damage or signs of chemical attack [58]. Future work may consider novel transformer designs which take full advantage of improved cooling. This can be achieved by spacing out the coils and magnetic core, allowing the dielectric fluid to fill the gaps and maximise heat transfer from their surfaces.

Another avenue of investigation may consider the electrical performance of circuits immersed in dielectric fluid. Operation of resonant converter topologies is sensitive to the inductances and capacitances associated with the isolating transformer. In [58], it is observed that immersion yields negligible impact on magnetic properties of the core and hence on inductances. However, the dielectric constant of the fluid, which floods the gaps in between adjacent coil turns, impacts the inter-turn capacitance. A simulation analysis performed in [89] indicates this can lead to voltage overshoots, oscillations and greater energy loss during switching transients. This provides an imperative for increasing the inter-turn spacing. There is a clear trade-off between parasitic capacitance and volume which depends on the turn spacing and could be investigated in further work.

Appendices

A
Uncertainty Evaluation

In Chapters 3 and 4, uncertainties are reported for heat fluxes and heat transfer coefficients which were calculated from measured temperatures, pressures, voltages and currents. This appendix details the procedure used to propagate uncertainties in the measurements to obtain uncertainties for derived values.

A quantity Y is calculated from independently measured quantities $X_\mathrm{a}, X_\mathrm{b}, ...X_\mathrm{z}$ via the functional relationship Φ.

$$Y = \Phi(X_\mathrm{a}, X_\mathrm{b}, ...X_\mathrm{z}) \tag{A.1}$$

Measurements $x_\mathrm{a}, x_\mathrm{b}, ...x_\mathrm{z}$ of these quantities are taken with uncertainty $\Delta x_a, \Delta x_b, ...\Delta x_\mathrm{z}$. In general, the uncertainty Δy in the corresponding calculated quantity can be estimated using Equation A.2 [90].

$$\Delta y = \sqrt{\left(\left.\frac{\partial \Phi}{\partial X_\mathrm{a}}\right|_{X_\mathrm{a}=x_\mathrm{a}} \Delta x_\mathrm{a}\right)^2 + \left(\left.\frac{\partial \Phi}{\partial X_\mathrm{b}}\right|_{X_\mathrm{b}=x_\mathrm{b}} \Delta x_\mathrm{b}\right)^2 + ... \left(\left.\frac{\partial \Phi}{\partial X_\mathrm{z}}\right|_{X_\mathrm{z}=x_\mathrm{z}} \Delta x_\mathrm{z}\right)^2} \tag{A.2}$$

Most of the calculated uncertainties in Table. 3.3 can be derived by combining standard rules for sums, products and quotients which follow from Equation. A.2. The only exception is the saturation temperature, which is related to the pressure by Equation. A.3.

$$P_\mathrm{s} = \exp\left(\frac{-3548.6}{T_\mathrm{s} + 273.15} + 22.978\right) \tag{A.3}$$

To calculate its uncertainty, it is necessary to evaluate derivative $\frac{\mathrm{d}T_\mathrm{s}}{\mathrm{d}P_\mathrm{s}}$ via the following expression

$$\frac{\mathrm{d}T_\mathrm{s}}{\mathrm{d}P_\mathrm{s}} = \frac{3548.6}{P_\mathrm{s}(22.978 - \log(P_\mathrm{s}))^2} \tag{A.4}$$

B

Analytical Solutions of the One-Dimensional Heat Equation

B.1 Pin Fin with Uniform Surface Heat Flux

In Chapter 4, analytical solution for a pin fin subject to a uniform heat flux on all surfaces was discussed. The heat equation for this problem is expressed below.

$$\frac{\mathrm{d}^2T}{\mathrm{d}x^2} = \frac{4q}{k_\mathrm{f}t_\mathrm{f}} \tag{B.1}$$

By integrating both sides of the equation twice, the following relationship is derived where A and B are constants of integration.

$$T = \frac{2q}{k_\mathrm{f}t_\mathrm{f}}x^2 + Ax + B \tag{B.2}$$

A constant heat flux boundary condition is applied at the fin tip:

$$-k_\mathrm{f}\frac{\mathrm{d}T}{\mathrm{d}x}\bigg|_{x=L} = -k_\mathrm{f}\left(\frac{4qL}{k_\mathrm{f}t_\mathrm{f}} + A\right) = q \tag{B.3}$$

Applying the boundary condition and rearranging yields the following expression for the constant A.

$$A = -\left(\frac{q}{k_\mathrm{f}} + \frac{4qL}{k_\mathrm{f}t_\mathrm{f}}\right) \tag{B.4}$$

The fin temperature at the fin base, $T|_{x=0}$ is constant at T_c. This yields the following equation for constant B.

$$B = T_\mathrm{c} \tag{B.5}$$

The heat transfer through the fin can be evaluated via Equation B.6.

$$Q_\mathrm{f} = -k_\mathrm{f} t_\mathrm{f}^2 \left.\frac{\mathrm{d}T}{\mathrm{d}x}\right|_{x=0} = -k_\mathrm{f} t_\mathrm{f}^2 A = q t_\mathrm{f}^2 + 4qLt_\mathrm{f} \tag{B.6}$$

B.2 Cylindrical Magnetic Core with Uniform Power Dissipation

In Chapter 6, the heat equation for cylindrical magnetic core cross sections with volumetric power dissipation was discussed. A more detailed derivation of the solution is presented here. The heat equation is expressed in polar coordinates below.

$$\frac{1}{r}\frac{\mathrm{d}}{\mathrm{d}r}\left(k_\mathrm{cr} r \frac{\mathrm{d}T}{\mathrm{d}r}\right) = -Q''' \tag{B.7}$$

Rearranging and integrating twice leads to the following expression in terms of integration constants A and B.

$$T = B - \frac{Q''' r^2}{4k_\mathrm{cr}} + \frac{A\log(r)}{k_\mathrm{cr}} \tag{B.8}$$

In order for the temperature to remain bounded at the core centre, constant A must be equal to zero. If the core is subject to a heat transfer coefficient at its surface $r = \frac{d_\mathrm{cr}}{2}$, the boundary condition can be expressed as follows.

$$-k_\mathrm{cr}\left.\frac{\mathrm{d}T}{\mathrm{d}r}\right|_{r=\frac{d_\mathrm{cr}}{2}} = \frac{Q''' d_\mathrm{cr}}{4} = h(T|_{r=\frac{d_\mathrm{c}r}{2}} - T_\mathrm{s}) = B - \frac{Q''' d_\mathrm{cr}^2}{16k_\mathrm{cr}} - T_\mathrm{s} \tag{B.9}$$

This yields the following expression for constant B.

$$B = T_\mathrm{s} + \frac{Q''' d_\mathrm{cr}^2}{16k_\mathrm{cr}} + \frac{Q''' d_\mathrm{cr}}{4} \tag{B.10}$$

By equating the highest temperature, found at the core centre $r = 0$, to the Curie temperature T_cr, the following expression is obtained.

$$T_\mathrm{cr} = T_\mathrm{s} + \frac{Q''' d_\mathrm{cr}^2}{16k_\mathrm{cr}} + \frac{Q''' d_\mathrm{cr}}{4h} \tag{B.11}$$

If the heat flux at the core surface reaches critical heat flux, the boundary condition can be expressed as follows.

$$-k_{\mathrm{cr}} \frac{\mathrm{d}T}{\mathrm{d}r}\bigg|_{r=\frac{d_{\mathrm{cr}}}{2}} = \frac{Q''' d_{\mathrm{cr}}}{4} = q_{\mathrm{chf}} \tag{B.12}$$

C
Transformer Core Sizing

In Chapter 6 the following expression was derived relating the diameter of a magnetic core d_{cr} to its electrical and thermal parameters. The left hand side of the equality is denoted as a function ϕ of core diameter.

$$\phi(d_{\text{cr}}) = \frac{d_{\text{cr}}^{2b}}{\frac{d_{\text{cr}}^2}{16k_{\text{cr}}} + \frac{d_{\text{cr}}}{4h}} = \left(\frac{V}{N_{\text{w}}\pi}\right)^b \frac{cf^{a-b}}{T_{\text{cr}} - T_{\text{s}}} \tag{C.1}$$

The derivative $\phi'(d_{\text{dc}})$ can be evaluated using the quotient rule, yielding Equation C.2.

$$\phi'(d_{\text{cr}}) = \frac{(2b-2)\frac{d_{\text{cr}}^{2b+1}}{16k_{\text{cr}}} + (2b-1)\frac{d_{\text{cr}}^{2b}}{4h}}{\left(\frac{d_{\text{cr}}^2}{16k_{\text{cr}}} + \frac{d_{\text{cr}}}{4h}\right)^2} \tag{C.2}$$

Since $2b > 2$, the derivative is always positive and $\phi(d_{\text{cr}})$ is a monotonically increasing function of core diameter. This is illustrated in Fig. C.1 which plots the left and right hand sides of Equation C.1 for different values of core diameter and Curie temperature. For a given temperature, there exists a single solution for the core diameter. Furthermore, it is clear the smallest core diameter occurs for the largest temperature at the core centre i.e. when it reaches the Curie temperature of the material.

The core diameter is calculated numerically by Newton's method using the

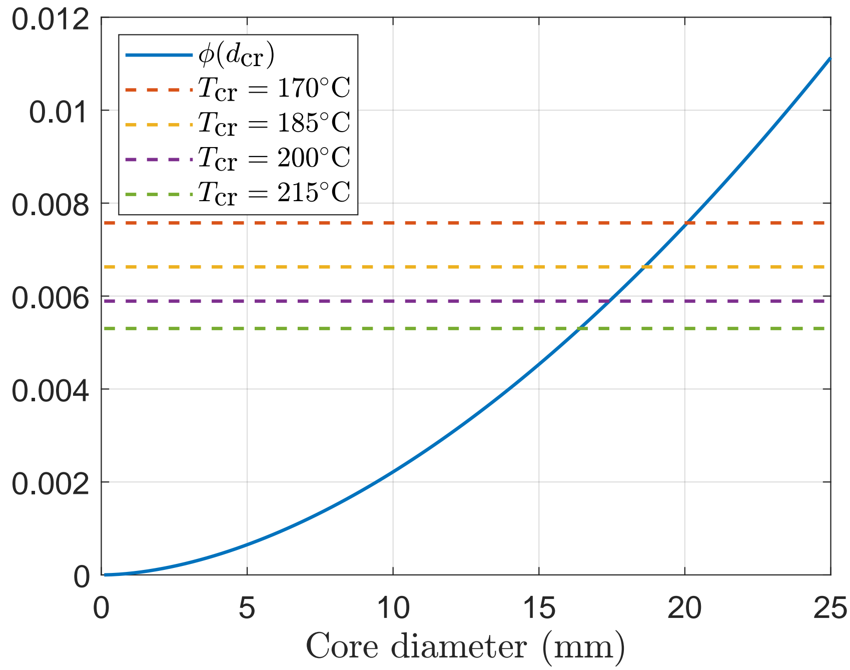

Figure C.1: $\phi(d_{\mathrm{cr}})$ plotted as a function of core diameter. Also shown is the right hand side of Equation C.2) for various values of Curie temperature.

following relation to iteratively update an estimate to the solution.

$$d_{\mathrm{cr}} = d_{\mathrm{cr}} - \frac{\phi(d_{\mathrm{cr}}) - \left(\frac{V}{N_{\mathrm{w}}\pi}\right)^{b} \frac{cf^{a-b}}{T_{\mathrm{cr}} - T_{\mathrm{s}}}}{\phi'(d_{\mathrm{cr}})} \tag{C.3}$$

References

[1] Samantha Jones-Jackson et al. "Overview of Current Thermal Management of Automotive Power Electronics for Traction Purposes and Future Directions". In: *IEEE Transactions on Transportation Electrification* 8.2 (2022), pp. 2412–2428.

[2] Hanyan Gao and Pan Liu. "High-Temperature Encapsulation Materials for Power Modules: Technology and Future Development Trends". In: *IEEE Transactions on Components, Packaging and Manufacturing Technology* 12.11 (2022), pp. 1867–1881.

[3] C. Gillot et al. "Double-sided cooling for high power IGBT modules using flip chip technology". In: *IEEE Transactions on Components and Packaging Technologies* 24.4 (2001), pp. 698–704.

[4] Fabio Carastro et al. "DCM™1000X – Automotive Power Module Technology Platform Optimized for SiC Traction Inverters". In: *2021 IEEE Applied Power Electronics Conference and Exposition (APEC)*. 2021, pp. 2364–2368.

[5] *Power Electronics Roadmap 2020 Narrative Report*. Advanced Propulsion Centre UK. Feb. 2021. URL: `apcuk.co.uk/power-electronics-roadmap/`.

[6] Yu Ren et al. "Analysis of a low-inductance packaging layout for Full-SiC power module embedding split damping". In: *2016 IEEE Applied Power Electronics Conference and Exposition (APEC)*. 2016, pp. 2102–2107.

[7] Xingyue Tian et al. "PCB-on-DBC GaN Power Module Design with High-Density Integration and Double-Sided Cooling". In: *IEEE Transactions on Power Electronics* (2023), pp. 1–10.

[8] Lei Kou and Juncheng Lu. "Applying GaN HEMTs in Conventional Housing-Type Power Modules". In: *2020 IEEE Energy Conversion Congress and Exposition (ECCE)*. 2020, pp. 4006–4011.

[9] Han Jiang et al. "Further Enhancement of Thermal Conductivity through Optimal Uses of h-BN Fillers in Polymer-Based Thermal Interface Material for Power Electronics". In: *2019 IEEE 69th Electronic Components and Technology Conference (ECTC)*. 2019, pp. 1569–1574.

[10] *TG-A1780 Ultra Soft Thermal Pad*. T-Global Technology. July 2023.

[11] K. Hiraishi et al. "Development and practical operation of perfluorocarbon immersed 275 kV transformers with compressed SF/sub 6/ gas insulation". In: *IEEE Transactions on Power Delivery* 10.2 (1995), pp. 880–888.

[12] Shiro Nukiyama. "The maximum and minimum values of the heat Q transmitted from metal to boiling water under atmospheric pressure". In: *International Journal of Heat and Mass Transfer* 9.12 (1966), pp. 1419–1433. URL: `https://www.sciencedirect.com/science/article/pii/0017931066901384`.

[13] Stanley J. Reed and Issam Mudawar. “Enhancement of boiling heat transfer using highly wetting liquids with pressed-on fins at low contact forces”. In: *International Journal of Heat and Mass Transfer* 40.10 (1997), pp. 2379–2392. URL: https://www.sciencedirect.com/science/article/pii/S0017931096002864.

[14] A Bejan and A.D. Kraus. *A Heat Transfer Handbook*. New Jersey: John Wiley and Sons, 2003.

[15] Phillip E. Tuma. “Design considerations relating to non-thermal aspects of passive 2-phase immersion cooling”. In: *2011 27th Annual IEEE Semiconductor Thermal Measurement and Management Symposium*. 2011, pp. 1–9.

[16] *3M Fluorinert Electronic Liquid FC-72*. 3M. Sept. 2019.

[17] *3M Novec7000 Engineered Fluid*. 3M. Sept. 2021.

[18] *Physical Properties of Pure Methanol*. Methanol Institute. June 2016.

[19] *Dielectric Constant of Common Solvents*. University of Washington.

[20] The Engineering ToolBox. *Water - Thermophysical Properties*. 2003. URL: https://www.engineeringtoolbox.com/water-thermal-properties-d_162.html.

[21] W. Bailey et al. “Pool boiling study on candidature of pentane, methanol and water for near room temperature cooling”. In: *Thermal and Thermomechanical Proceedings 10th Intersociety Conference on Phenomena in Electronics Systems, 2006. ITHERM 2006.* 2006, pp. 599–603.

[22] I. Mudawar and T. M. Anderson. “Optimization of Enhanced Surfaces for High Flux Chip Cooling by Pool Boiling”. In: *Journal of Electronic Packaging* 115.1 (Mar. 1993), pp. 89–100. eprint: https://asmedigitalcollection.asme.org/electronicpackaging/article-pdf/115/1/89/5629997/89_1.pdf. URL: https://doi.org/10.1115/1.2909306.

[23] M. El-Genk. “Nucleate boiling enhancements for immersion cooling of high power electronics”. In: *2010 3rd International Conference on Thermal Issues in Emerging Technologies Theory and Applications*. 2010, pp. 5–5.

[24] Mohamed S. El-Genk and Mahyar Pourghasemi. “Experimental investigation of saturation boiling of HFE-7000 dielectric liquid on rough copper surfaces”. In: *Thermal Science and Engineering Progress* 15 (2020), p. 100428. URL: https://www.sciencedirect.com/science/article/pii/S2451904919302343.

[25] Omidreza Ghaffari et al. “Pool Boiling Experiment of Dielectric Liquids and Numerical Study for Cooling a Microprocessor”. In: *2019 18th IEEE Intersociety Conference on Thermal and Thermomechanical Phenomena in Electronic Systems (ITherm)*. 2019, pp. 540–545.

[26] T. M. Anderson and I. Mudawar. “Microelectronic Cooling by Enhanced Pool Boiling of a Dielectric Fluorocarbon Liquid”. In: *Journal of Heat Transfer* 111.3 (Aug. 1989), pp. 752–759. eprint: https://asmedigitalcollection.asme.org/heattransfer/article-pdf/111/3/752/5551970/752_1.pdf. URL: https://doi.org/10.1115/1.3250747.

[27] Kazuhisa Yuki et al. "Immersion cooling of electronics utilizing lotus-type porous copper". In: *2016 International Conference on Electronics Packaging (ICEP)*. 2016, pp. 169–172.

[28] Pramod Warrier et al. "Novel heat transfer fluids for direct immersion phase change cooling of electronic systems". In: *International Journal of Heat and Mass Transfer* 55.13 (2012), pp. 3379–3385. URL: https://www.sciencedirect.com/science/article/pii/S0017931012001263.

[29] Aravind Sathyanarayana et al. "Pool Boiling of HFE 7200–C4H4F6O Mixture on Hybrid Micro-Nanostructured Surface". In: *Journal of Nanotechnology in Engineering and Medicine* 3.4 (Mar. 2013), p. 041004. eprint: https://asmedigitalcollection.asme.org/nanoengineeringmedical/article-pdf/3/4/041004/6280536/nano_3_4_041004.pdf. URL: https://doi.org/10.1115/1.4023245.

[30] Patrick Birbarah et al. "Water immersion cooling of high power density electronics". In: *International Journal of Heat and Mass Transfer* 147 (2020), p. 118918. URL: https://www.sciencedirect.com/science/article/pii/S0017931019336002.

[31] Ankit Kalani and Satish G. Kandlikar. "Enhanced Pool Boiling With Ethanol at Subatmospheric Pressures for Electronics Cooling". In: *Journal of Heat Transfer* 135.11 (Sept. 2013). 111002. eprint: https://asmedigitalcollection.asme.org/heattransfer/article-pdf/135/11/111002/6205434/ht_135_11_111002.pdf. URL: https://doi.org/10.1115/1.4024595.

[32] Nobuyuki Otsuka et al. "Low-Pressure Direct-Liquid-Cooling Technology for GaN Power Transistors". In: *Japanese Journal of Applied Physics* 50.4S (2011), 04DF07. URL: https://dx.doi.org/10.1143/JJAP.50.04DF07.

[33] Chiara Falsetti, Jason Chetwynd-Chatwin, and Edmond J. Walsh. "Pool boiling heat transfer of Novec 649 on sandblasted surfaces". In: 2024, p. 100615. URL: https://www.sciencedirect.com/science/article/pii/S2666202724000570.

[34] J.J. Wei and H. Honda. "Effects of fin geometry on boiling heat transfer from silicon chips with micro-pin-fins immersed in FC-72". In: *International Journal of Heat and Mass Transfer* 46.21 (2003), pp. 4059–4070. URL: https://www.sciencedirect.com/science/article/pii/S0017931003002266.

[35] Yaser Nabavi Larimi et al. "Multi-Scale Electroplated Porous Coating for Immersion Cooling of Electronics". In: *2022 21st IEEE Intersociety Conference on Thermal and Thermomechanical Phenomena in Electronic Systems (iTherm)*. 2022, pp. 1–7.

[36] Kazuhisa Yuki et al. "Immersion cooling of electronics utilizing lotus-type porous copper". In: *2016 International Conference on Electronics Packaging (ICEP)*. 2016, pp. 169–172.

[37] Joshua Gess et al. "Impact of surface enhancements upon boiling heat transfer in a liquid immersion cooled high performance small form factor server model". In: *Fourteenth Intersociety Conference on Thermal and Thermomechanical Phenomena in Electronic Systems (ITherm)*. 2014, pp. 435–443.

[38] Kazuhisa YUKI et al. “Thermal management of automotive SiC-based on-board inverter with 500 W/cm² in heat flux, and Two-phase immersion cooling by breathing phenomenon spontaneously induced by lotus porous copper jointed onto a grooved heat transfer surface”. In: *Journal of Thermal Science and Technology* 15.1 (2020), JTST0012–JTST0012.

[39] D. Tanaka et al. “Heat Transfer Enhancement in Two-phase Immersion Cooling with FC-72”. In: *2023 International Conference on Electronics Packaging (ICEP)*. 2023, pp. 179–180.

[40] P.E. Tuma. “Evaporator/boiler design for thermosyphons utilizing segregated hydrofluoroether working fluids”. In: *Twenty-Second Annual IEEE Semiconductor Thermal Measurement And Management Symposium*. 2006, pp. 69–77.

[41] Karl J. L. Geisler and Avram Bar-Cohen. “Optimization of Pool Boiling Heat Sinks Including the Effects of Confinement in the Interfin Spaces”. In: *Journal of Electronic Packaging* 130.4 (Nov. 2008), p. 041002. eprint: https://asmedigitalcollection.asme.org/electronicpackaging/article-pdf/130/4/041002/5803336/041002_1.pdf. URL: https://doi.org/10.1115/1.2993135.

[42] Cindy M. Barnes and Phillip E. Tuma. “Practical Considerations Relating to Immersion Cooling of Power Electronics in Traction Systems”. In: *IEEE Transactions on Power Electronics* 25.9 (2010), pp. 2478–2485.

[43] *Immersion Cooling of Power Electronics in Segregated Hydrofluoroether Liquids*. Vol. Heat Transfer: Volume 2. Heat Transfer Summer Conference. Aug. 2008, pp. 719–725. eprint: https://asmedigitalcollection.asme.org/HT/proceedings-pdf/HT2008/48487/719/2711578/719_1.pdf. URL: https://doi.org/10.1115/HT2008-56230.

[44] D.B. Tuckerman and R.F.W. Pease. “High-performance heat sinking for VLSI”. In: *IEEE Electron Device Letters* 2.5 (1981), pp. 126–129.

[45] Gongyue Tang et al. “Development of a Compact and Efficient Liquid Cooling System With Silicon Microcooler for High-Power Microelectronic Devices”. In: *IEEE Transactions on Components, Packaging and Manufacturing Technology* 6.5 (2016), pp. 729–739.

[46] Sevket U. Yuruker et al. “A Vertically Enhanced Manifold Microchannel System for Thermal Management of Power Electronics”. In: *IEEE Transactions on Components, Packaging and Manufacturing Technology* 11.10 (2021), pp. 1716–1723.

[47] Remco van Erp, Georgios Kampitsis, and Elison Matioli. “Efficient Microchannel Cooling of Multiple Power Devices With Compact Flow Distribution for High Power-Density Converters”. In: *IEEE Transactions on Power Electronics* 35 (2020), pp. 7235–7245. URL: https://api.semanticscholar.org/CorpusID:209428284.

[48] Gilberto Moreno et al. “Single-Phase Dielectric Fluid Thermal Management for Power-Dense Automotive Power Electronics”. In: *IEEE Transactions on Power Electronics* 37.10 (2022), pp. 12474–12485.

[49] Uwe Drofenik, Andrija Stupar, and Johann W. Kolar. “Analysis of Theoretical Limits of Forced-Air Cooling Using Advanced Composite Materials With High Thermal Conductivities”. In: *IEEE Transactions on Components, Packaging and Manufacturing Technology* 1.4 (2011), pp. 528–535.

[50] Phillip E. Tuma, Bamidele O. Fayemi, and Lawrence J. Stang. “Condenser Design for Thermosyphons Utilizing Segregated Hydrofluoroether Working Fluids”. In: *Twenty-Third Annual IEEE Semiconductor Thermal Measurement and Management Symposium*. 2007, pp. 162–167.

[51] Omidreza Ghaffari et al. “Study of the Impact of the Airflow and Filling Ratio on the Thermal Performances of a Two-Phase Immersion Cooling Prototype”. In: *2022 21st IEEE Intersociety Conference on Thermal and Thermomechanical Phenomena in Electronic Systems (iTherm)*. 2022, pp. 1–6.

[52] Chiara Falsetti et al. “Experimental Analysis of the Condenser Design in a Thermosiphon System for Cooling of Telecommunication Electronics”. In: *IEEE Transactions on Components, Packaging and Manufacturing Technology* 10.6 (2020), pp. 963–973.

[53] Francesco Agostini and Bruno Agostini. “Flexible two-phase thermosyphon for power electronic cooling”. In: *2011 IEEE 33rd International Telecommunications Energy Conference (INTELEC)*. 2011, pp. 1–6.

[54] Raffaele L. Amalfi et al. “Two-phase liquid cooling system for electronics, part 3: Ultra-compact liquid-cooled condenser”. In: *2017 16th IEEE Intersociety Conference on Thermal and Thermomechanical Phenomena in Electronic Systems (ITherm)*. 2017, pp. 687–695.

[55] C. Tantolin, M. Lallemand, and U. Eckes. “Experimental study of immersion cooling for power components”. In: *1994 International Conference on Control - Control ’94*. Vol. 1. 1994, 723–727 vol.1.

[56] W.G. Koellner et al. “Recent advances in mining haul trucks”. In: *IEEE Transactions on Industrial Electronics* 51.2 (2004), pp. 321–329.

[57] Joshua L. Gess, Sushil H. Bhavnani, and R. Wayne Johnson. “Experimental Investigation of a Direct Liquid Immersion Cooled Prototype for High Performance Electronic Systems”. In: *IEEE Transactions on Components, Packaging and Manufacturing Technology* 5.10 (2015), pp. 1451–1464.

[58] A. Yingke Wen et al. “Study of material compatibility and parasitic parameters of magnetic components in fully-immersion evaporative cooling system”. In: *2016 19th International Conference on Electrical Machines and Systems (ICEMS)*. 2016, pp. 1–6.

[59] Kangjie Huang and Bin Xiong. “Research on Insulation Characteristics of Distributed Winding with Cooling Chamber for Evaporative Cooling Transformer”. In: *2021 24th International Conference on Electrical Machines and Systems (ICEMS)*. 2021, pp. 489–494.

[60] Hualin Shi et al. “Application of Evaporative Cooling Technology in Transformer for Mine Tunnels”. In: *Processes* 9.5 (2021). URL: https://www.mdpi.com/2227-9717/9/5/875.

[61] Smreeti Dahariya and Amy R. Betz. “High pressure pool boiling: Mechanisms for heat transfer enhancement and comparison to existing models”. In: *International Journal of Heat and Mass Transfer* 141 (2019), pp. 696–706. URL: https://www.sciencedirect.com/science/article/pii/S0017931019301243.

[62] Hiroto SAKASHITA. “Bubble Growth Rates and Nucleation Site Densities in Saturated Pool Boiling of Water at High Pressures”. In: *Journal of Nuclear Science and Technology* 48.5 (2011), pp. 734–743. eprint: https://www.tandfonline.com/doi/pdf/10.1080/18811248.2011.9711756. URL: https://www.tandfonline.com/doi/abs/10.1080/18811248.2011.9711756.

[63] *3M Fluorinert Electronic Liquid FC-72*. 3M. Sept. 2019.

[64] *3M Fluorinert Electronic Liquid FC-87*. 3M. Sept. 2019.

[65] *3M Novec649 Engineered Fluid*. 3M. Sept. 2009.

[66] SANTI R. PALIT. “Thermodynamic Interpretation of the Eötvös Constant”. In: *Nature* 177.4521 (1956), pp. 1180–1180. URL: https://doi.org/10.1038/1771180a0.

[67] Warren Max Rohsenow. “A Method of Correlating Heat-Transfer Data for Surface Boiling of Liquids”. In: *Journal of Fluids Engineering* (1952). URL: https://api.semanticscholar.org/CorpusID:94343868.

[68] K. Stephan and M. Abdelsalam. “Heat-transfer correlations for natural convection boiling”. In: *International Journal of Heat and Mass Transfer* 23.1 (1980), pp. 73–87. URL: https://www.sciencedirect.com/science/article/pii/0017931080901404.

[69] Klaus Spindler. “Overview and discussion on pool boiling heat transfer data and correlations of ammonia”. In: *International Journal of Refrigeration* 33.7 (2010), pp. 1292–1306. URL: https://www.sciencedirect.com/science/article/pii/S0140700710001428.

[70] I.L. Pioro, W. Rohsenow, and S.S. Doerffer. “Nucleate pool-boiling heat transfer. II: assessment of prediction methods”. In: *International Journal of Heat and Mass Transfer* 47.23 (2004), pp. 5045–5057. URL: https://www.sciencedirect.com/science/article/pii/S0017931004002637.

[71] Novak Zuber. “Hydrodynamic Aspects Of Boiling Heat Transfer (Thesis)”. In: (). URL: https://www.osti.gov/biblio/4175511.

[72] John H. Lienhard and Vijay K. Dhir. “Hydrodynamic Prediction of Peak Pool-boiling Heat Fluxes from Finite Bodies”. In: *Journal of Heat Transfer-transactions of The Asme* 95 (1973), pp. 152–158. URL: https://api.semanticscholar.org/CorpusID:120647310.

[73] *GS66516T Top-side cooled 650 V E-mode GaN transistor*. GaN Systems. 2021.

[74] Ilya T’Jollyn et al. “Nucleate Pool Boiling Regimes Of Power Electronics Cooling”. In: *2022 28th International Workshop on Thermal Investigations of ICs and Systems (THERMINIC)*. 2022, pp. 1–5.

[75] F. Fantozzi, A. Franco, and E. M. Latrofa. “Analysis of the heat dissipation enhancement with finned surfaces in pool boiling of dielectric fluid”. In: *Heat and Mass Transfer* 36.6 (2000), pp. 487–495. URL: https://doi.org/10.1007/s002310000110.

[76] Joseph Gerstmann and Peter Griffith. “Laminar film condensation on the underside of horizontal and inclined surfaces”. In: *International Journal of Heat and Mass Transfer* 10 (1967), pp. 567–580.

[77] Matteo Fabbri, Shanjuan Jiang, and Vijay K. Dhir. “A Comparative Study of Cooling of High Power Density Electronics Using Sprays and Microjets ”. In: *Journal of Heat Transfer* 127.1 (Feb. 2005), pp. 38–48. eprint: https://asmedigitalcollection.asme.org/heattransfer/article-pdf/127/1/38/5791198/38_1.pdf. URL: https://doi.org/10.1115/1.1804205.

[78] Irma Villar et al. “Transient thermal model of a medium frequency power transformer”. In: *2008 34th Annual Conference of IEEE Industrial Electronics*. 2008, pp. 1033–1038.

[79] Selami Balci, Ibrahim Sefa, and Necmi Altin. “Thermal Behavior of a Medium-Frequency Ferrite-Core Power Transformer”. In: *Journal of Electronic Materials* 45.8 (2016), pp. 3978–3988. URL: https://doi.org/10.1007/s11664-016-4567-5.

[80] Diaa-Eldin A. Mansour and Ahmed M. Elsaeed. “Heat transfer properties of transformer oil-based nanofluids filled with Al2O3 nanoparticles”. In: *2014 IEEE International Conference on Power and Energy (PECon)*. 2014, pp. 123–127.

[81] R.W. Erickson and D Maksimovic. *Fundamentals of Power Electronics*. New York: Kluwer Academic/Plenum Publishers, 2001.

[82] The Engineering ToolBox. *Resistivity and Conductivity - Temperature Coefficients Common Materials*. 2003. URL: https://www.engineeringtoolbox.com/resistivity-conductivity-d_418.html.

[83] Alicia H. Howard and Issam Mudawar. “Orientation effects on pool boiling critical heat flux (CHF) and modeling of CHF for near-vertical surfaces”. In: *International Journal of Heat and Mass Transfer* 42.9 (1999), pp. 1665–1688. URL: https://www.sciencedirect.com/science/article/pii/S0017931098002336.

[84] Xiaomei Liu et al. “Effective Thermal Conductivity Calculation and Measurement of Litz Wire Based on the Porous Metal Materials Structure”. In: *IEEE Transactions on Industrial Electronics* 67.4 (2020), pp. 2667–2677.

[85] Fair-rite. *Toroids (5977001401*. 2023. URL: https://fair-rite.com/product/toroids-5977001401/.

[86] N. Mohan, T.M. Undeland, and W.P. Robbins. *Power Electronics: Converters, Applications and Design*. New York: John Wiley and Sons, 1989.

[87] W.R. McGillis et al. “Boiling binary mixtures at subatmospheric pressures”. In: *[1992 Proceedings] Intersociety Conference on Thermal Phenomena in Electronic Systems*. 1992, pp. 127–136.

[88] M.A. Gómez et al. "Thermal study of a passive cooling device operating through a bubble lifting CLTPT of NOVEC 7000 with a two-fluid condenser". In: *International Journal of Heat and Mass Transfer* 177 (2021), p. 121530. URL: https://www.sciencedirect.com/science/article/pii/S0017931021006335.

[89] A. Yingke Wen et al. "Simulation and performance analysis of fully-immersion evaporative cooling switching mode power supply". In: *2016 19th International Conference on Electrical Machines and Systems (ICEMS)*. 2016, pp. 1–5.

[90] A Silcox. *Basic Analysis of Data*. 2008. URL: https://my.che.utah.edu/~geoff/writing/statistics.pdf.